

AD-A119 074

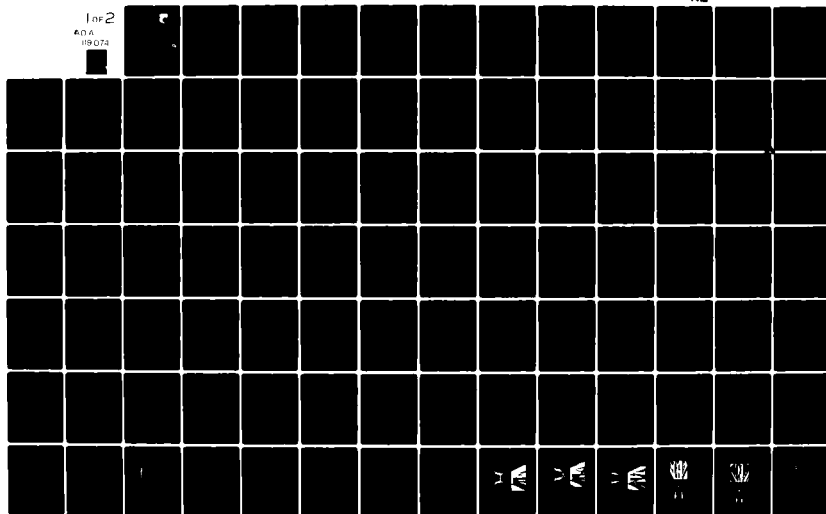
AIR FORCE WRIGHT AERONAUTICAL LABS WRIGHT-PATTERSON AFB OH F/G 20/4  
NAVIER-STOKES SOLUTIONS FOR AN AXISYMMETRIC NOZZLE IN A SUPERSO--ETC(U)  
MAR 82 G A HASEN  
AFWAL-TR-81-3161

UNCLASSIFIED

NL

1 of 2

ADA  
119 074



AD A119074



# NAVIER-STOKES SOLUTIONS FOR AN AXISYMMETRIC NOZZLE IN A SUPERSONIC EXTERNAL STREAM

Gerald A. Hasen, Captain, USAF  
Aerodynamics and Airframe Branch  
Aeromechanics Division

March 1982

Final Report for Period June 1978 - April 1981

Approved for public release; distribution unlimited.

DTIC  
SELECTED  
SEP 9 1982  
H

FLIGHT DYNAMICS LABORATORY  
AIR FORCE WRIGHT AERONAUTICAL LABORATORIES  
AIR FORCE SYSTEMS COMMAND  
WRIGHT-PATTERSON AIR FORCE BASE, OHIO 45433

DIR FILE COPY

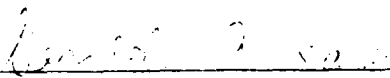
82 10 10 10 2

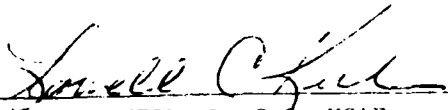
NOTICE

When Government drawings, specifications, or other data are used for any purpose other than in connection with a definitely related Government procurement operation, the United States Government thereby incurs no responsibility nor any obligation whatsoever; and the fact that the government may have formulated, furnished, or in any way supplied the said drawings, specifications, or other data, is not to be regarded by implication or otherwise as in any manner licensing the holder or any other person or corporation, or conveying any rights or permission to manufacture use, or sell any patented invention that may in any way be related thereto.


This report has been reviewed by the Office of Public Affairs (ASD/PA) and is releasable to the National Technical Information Service (NTIS). At NTIS, it will be available to the general public, including foreign nations.

This technical report has been reviewed and is approved for publication.

  
GERALD A. HASEN, Captain, USAF  
Project Engineer

  
LOWELL C. KEEL, Lt Col, USAF  
Chief, Aerodynamics and Airframe Branch

FOR THE COMMANDER

  
JOHN R. CHEVALIER, Colonel, USAF  
Chief, Aeromechanics Division

If your address has changed, if you wish to be removed from our mailing list, or if the addressee is no longer employed by your organization please notify AFWAL/FIMM, W-PAFB, OH 45433 to help us maintain a current mailing list.

Copies of this report should not be returned unless return is required by security considerations, contractual obligations, or notice on a specific document.

UNCLASSIFIED

SECURITY CLASSIFICATION OF THIS PAGE (When Data Entered)

REPORT DOCUMENTATION PAGE		READ INSTRUCTIONS BEFORE COMPLETING FORM
1. REPORT NUMBER AFWAL-TR-81-3161	2. GOVT ACCESSION NO. AD-A119074	3. RECIPIENT'S CATALOG NUMBER
4. TITLE (and Subtitle) NAVIER-STOKES SOLUTIONS FOR AN AXISYMMETRIC NOZZLE IN A SUPERSONIC EXTERNAL STREAM		5. TYPE OF REPORT & PERIOD COVERED Final Report June 1978 - April 1981
		6. PERFORMING ORG. REPORT NUMBER
7. AUTHOR(s) Gerald A. Hasen, Captain, USAF		8. CONTRACT OR GRANT NUMBER(s)
9. PERFORMING ORGANIZATION NAME AND ADDRESS Flight Dynamics Laboratory (AFWAL/FIMM) Air Force Wright Aeronautical Laboratories (AFSC) Wright-Patterson AFB, Ohio 45433		10. PROGRAM ELEMENT, PROJECT, TASK AREA & WORK UNIT NUMBERS Program Element 61102F, Project 2307, Task 2307N6, Work Unit 2307N603
11. CONTROLLING OFFICE NAME AND ADDRESS Flight Dynamics Laboratory (AFWAL/FIM) Air Force Wright Aeronautical Laboratories (AFSC) Wright-Patterson AFB, Ohio 45433		12. REPORT DATE March 1982
		13. NUMBER OF PAGES 139
14. MONITORING AGENCY NAME & ADDRESS (if different from Controlling Office)		15. SECURITY CLASS. (of this report)  Unclassified
		15a. DECLASSIFICATION DOWNGRADING SCHEDULE
16. DISTRIBUTION STATEMENT (of this Report)  Approved for public release; distribution unlimited.		
17. DISTRIBUTION STATEMENT (of the abstract entered in Block 20, if different from Report)		
18. SUPPLEMENTARY NOTES The material reported herein is based on the author's dissertation submitted in partial fulfillment of the requirements for the Doctor of Philosophy degree at the Air Force Institute of Technology, Wright-Patterson AFB, Ohio.		
19. KEY WORDS (Continue on reverse side if necessary and identify by block number) Computational Fluid Dynamics    Compressible Flow Numerical Solution                Turbulent Flow Navier-Stokes                      MacCormack's Explicit Method Axisymmetric Nozzle              Adaptive Grid Mach Disc		
20. ABSTRACT (Continue on reverse side if necessary and identify by block number) Numerical solutions of the Navier-Stokes equations are obtained for an axisymmetric nozzle in a supersonic external stream ( $M_\infty = 1.94$ , $M_j = 3.0$ , $Re_\infty = 2.2 \times 10^6$ ). Five jet pressure conditions ranging from a highly over-expanded case which exhibits a Mach disc shock formation to a slightly under-expanded case are examined and solved numerically. MacCormack's explicit method is applied as the numerical algorithm. An adaptive grid scheme is utilized in the nozzle wake to allow the fine mesh region of the computational grid to remain in areas containing relatively high flow gradients. Locally		

DD FORM 1473

EDITION OF 1 NOV 65 IS OBSOLETE

UNCLASSIFIED

SECURITY CLASSIFICATION OF THIS PAGE (When Data Entered)

dependent eddy viscosity modelling is applied in the form of a Cebeci-Smith two-layer model in the boundary layer regions on the nozzle walls, and a form of the Prandtl mixing length model in the nozzle wake. A two-dimensional wedge flat plate validation case was computed using these models with excellent results. The computational solutions of the axisymmetric nozzle accurately reproduced the experimentally observed viscous effects on the nozzle base pressure and shock wave locations that are caused by the thick nozzle base annulus. Correct transition was achieved numerically from regularly reflected shock waves at the line of symmetry in the jet core to a Mach disc reflection at the appropriate nozzle static pressure ratio.

# FOREWORD

This report is the result of research performed in the Computational Aerodynamics Group, Aerodynamics and Airframe Branch, Aeromechanics Division, Flight Dynamics Laboratory from June 1978 to April 1981. This report was prepared under Work Unit 2307N603, "Computational Fluid Dynamics". Dr. Wilbur L. Hankey is the Task Manager.

The author would like to express his thanks to Dr. Wilbur L. Hankey for his valuable advice and technical guidance in this work. Special thanks are also due to Dr. Joseph S. Shang of the Computational Aerodynamics Group for his guidance with the numerical algorithms portion of the research. Being associated with the members of the Computational Aerodynamics Group has been personally as well as technically rewarding. Appreciation is also expressed to the members of the AFIT faculty who served on my doctoral committee.

The material reported herein is based on the author's dissertation submitted in partial fulfillment of the requirements for the Doctor of Philosophy degree at the Air Force Institute of Technology, Wright-Patterson AFB, Ohio.

Accession For		<input checked="" type="checkbox"/>
DTIC	CR&I	<input type="checkbox"/>
DTIC	Tab	<input type="checkbox"/>
Unannounced		
Justification		
By		
Distribution/		
Availability Codes		
Dist	Avail	Special
A		

DTIC  
COPY  
RECEIVED

## TABLE OF CONTENTS

SECTION	PAGE
I INTRODUCTION	1
1. Background	1
2. Research Objectives	10
II MATHEMATICAL DESCRIPTION OF THE FLOW STRUCTURE	12
1. Governing Equations	12
2. Boundary and Initial Conditions	19
III NUMERICAL PROCEDURE	23
1. Coordinate System	23
2. Solution Algorithm	27
3. Convergence Criteria	35
IV BOUNDARY AND INITIAL CONDITION IMPLEMENTATION	39
1. The Upstream Boundary	39
2. The Upper Boundary	42
3. The Downstream Boundary	45
4. The Centerline	46
5. The Nozzle Walls	48
6. Initial Conditions	50
V TURBULENCE MODELING	52
1. Boundary Layer Model	52
2. Far Wake Model	54
3. Near Wake Model	59
VI NUMERICAL RESULTS	65
1. Experimental Data Base	65
2. Computational Details	66
3. Comparison with Experimental Data	73
VII CONCLUSIONS AND RECOMMENDATIONS	90
APPENDIX A NOZZLE WALL TEMPERATURE CALCULATION	93
APPENDIX B ADAPTIVE FINITE DIFFERENCE MESH	96
APPENDIX C TWO-DIMENSIONAL FLAT PLATE FAR WAKE SOLUTION	99
APPENDIX D TWO-DIMENSIONAL WEDGE-FLAT PLATE NEAR WAKE SOLUTION	103
APPENDIX E AXISYMMETRIC NOZZLE SOLUTION SIMULATING INTERNAL BOUNDARY LAYER SEPARATION	110
APPENDIX F INVESTIGATION OF NUMERICAL ERROR	114
REFERENCES	120

## LIST OF ILLUSTRATIONS

FIGURE		PAGE
1	Shock Structure for a Typical Overexpanded Axisymmetric Nozzle	4
2	Schematic of a Typical Mach Reflection	5
3	Hodograph Diagram Showing Shock Polar Intersections for Transition from Regular to Mach Reflection	7
4	Viscous Effects on the Mach Disc Structure	9
5	Schematic of the Axisymmetric Jet Model Used as a Basis for the Computational Solutions	11
6	Physical Domain for the Computational Solutions	19
7	Finite Difference Mesh in Physical Space	24
8	Exponentially Stretched Mesh Schematic	24
9	Adaptive Finite Difference Mesh, $P_j/P_\infty = 0.150$	26
10	Computational Mesh in the Transformed Plane	26
11	Graphical Representation of the Numerical Sweep Operators	30
12	Base Pressure Tap Location in the Flowfield	37
13	Typical Base Pressure Convergence, $P_j/P_\infty = 0.527$	38
14	Flowfield Schematic for an Axisymmetric Nozzle in a Supersonic External Stream	40
15	Computed Static Pressure Variation Along the Ogive Body Using a Parabolized Navier-Stokes Solver (Reference 23)	41
16	Upper Boundary Condition Schematic	43
17	Finite Difference Mesh Near the Nozzle Walls	49
18	Eddy Viscosity Model Domains	53
19	Eddy Viscosity Distribution Across a Boundary Layer	55
20	Typical Vorticity Profile Used to Compute Mixing Layer Thickness	57



## LIST OF ILLUSTRATIONS (Cont'd)

FIGURE		PAGE
21	Maximum Velocity Defect vs Distance Behind the Trailing Edge of a Two-Dimensional Flat Plate, $M_\infty = 1.60$	58
22	Viscous Layer Structure in the Near Wake	60
23	Computed Nozzle Base Pressure vs the Position of the Mixing Region Midpoint $X_m$	62
24	Computed Mixing Layer Thickness Used in the Wake Turbulence Model for the Wedge-Flat Plate Case	63
25	Adaptive Finite Difference Mesh, $P_j/P_\infty = 0.527$	68
26	Error in Computed Velocity Gradient vs Grid Courseness for a Turbulent Boundary Layer	70
27	Axisymmetric Nozzle Solution, $P_j/P_\infty = 0.150$	74
28	Axisymmetric Nozzle Solution, $P_j/P_\infty = 0.251$	75
29	Axisymmetric Nozzle Solution, $P_j/P_\infty = 0.527$	76
30	Axisymmetric Nozzle Solution, $P_j/P_\infty = 1.03$	77
31	Axisymmetric Nozzle Solution, $P_j/P_\infty = 1.59$	78
32	Computed Mach Number Contours in the Region Near the Shock Reflection at the Centerline	79
33	Computed Velocity Profiles, $P_j/P_\infty = 0.150$	81
34	Computed Velocity Fields in the Near Wake Region of the Nozzle Base Annulus	82
35	Position of the Dividing Streamline in the Computational Nozzle Solutions	83
36	Axial Variation in Computed Centerline Mach Number, $P_j/P_\infty = 0.150$	84
37	Shock Reflection Lengths Along the Nozzle Centerline vs Nozzle Pressure Ratio	85
38	Base Pressure Coefficient vs Nozzle Pressure Ratio	87
39	Schlieren Photographs (Reference 16) Showing the Eventual Deterioration of the Mach Disc with Decreasing Nozzle Pressure Ratio	89

## LIST OF ILLUSTRATIONS (Concluded)

FIGURE		PAGE
40	Heat Flux Balance Used to Determine the Nozzle Wall Temperature	94
41	Adaptive Mesh Schematic	98
42	Velocity Profile at the Trailing Edge of the Two-Dimensional Flat Plate	100
43	Computational Mesh Used in the Flat Plate Solution	102
44	Computed Flat Plate Velocity Profiles	102
45	Computational Boundary Conditions for the Two-Dimensional Wedge-Flat Plate	104
46	Computational Mesh Used for the Two-Dimensional Wedge-Flat Plate Solution	106
47	Two-Dimensional Wedge-Flat Plate with the Computed Mach Number Contours Shown	107
48	Computed Velocity Profiles in the Near Wake of the Two-Dimensional Wedge-Flat Plate	108
49	Static Pressure Along the Line of Symmetry in the Near Wake of the Two-Dimensional Wedge-Flat Plate	108
50	Pitot Pressure Profiles in the Near Wake of the Two-Dimensional Wedge-Flat Plate (Symbols-Experimental Data (Reference 34), Solid Lines - Computational Solution)	109
51	Computed Velocity Profiles Near the Nozzle Annulus for the Separated Flow Simulation	112
52	Computed Mach Number Contours for the Separated Flow Simulation	113
53	Comparison between the Computational Solution and the Error Present in the Continuity Equation, $P_j/P_\infty = 0.150$	116
54	Extension of the Downstream Boundary Showing Computed Mach Number Contours, $P_j/P_\infty = 0.251$	118
55	Extension of the Upper Boundary Showing Computed Mach Number Contours, $P_j/P_\infty = 0.251$	119

LIST OF TABLES

TABLE		PAGE
1	Computational Grid Parameters	67
2	Computational Jet Flow Parameters	71
3	Comparison Between a 1-D Analysis and the Computational Solution Across the Mach Disc for $P_j/P_\infty = 0.150$	80
4	Comparison of Shock Reflection Lengths	86
5	Comparison of Mach Disc Radii	86
6	Comparison of Base Pressure Coefficients	87

## LIST OF SYMBOLS

C	Constant used to obtain exponentially stretched mesh.
$C_A$	Adaptive mesh constant.
$C_f$	Local skin friction coefficient, $2\tau_w/\rho_\infty u_\infty^2$ .
$C_p$	Specific heat at constant pressure.
$C_v$	Specific heat at constant volume.
c	Speed of sound, $\sqrt{\gamma RT}$ .
E	Error vector.
e	Energy, $C_v T + (u^2 + v^2)/2$ .
F	Flux vector, Equation 28.
$F_D$	Damping vector, Equation 30.
f	Primitive flow variable $\rho$ , $u$ , $v$ , or $T$ .
G	Flux vector, Equation 28.
$G_D$	Damping vector, Equation 32.
H	Flux vector, Equation 28.
$H_o$	Total Enthalpy, $C_p T + (u^2 + v^2)/2$ .
$h_i$	Convective heat transfer coefficient, Appendix A.
h	Thickness of the two-dimensional wedge-flat plate.
i	Index for grid points in the axial direction.
IL	Total number of grid points in the axial direction.
IW	Number of grid points axially along the nozzle wall.
JL	Total number of grid points in the radial direction.
JWI	Radial index of the inner nozzle wall.
JWO	Radial index of the outer nozzle wall.
j	Index for grid points in the radial direction.
$j_o$	Exponent parameter equal to 0 or 1 for two-dimensional or axisymmetric flow, respectively.

## LIST OF SYMBOLS (Cont'd)

K	Ratio of radial grid point heights, $r(i,3)/r(i,2)$ .
$K_0$	Initial velocity profile constant in the wake region, Equation 111.
k	Thermal conductivity.
L	Length scale.
$L_b$	Experimental ogive body length
$L_m$	Length scale used to generate stretched mesh.
$L_\eta, L_\xi$	MacCormack difference operators in the $\eta$ and $\xi$ directions.
$\ell$	Prandtl turbulent mixing length.
M	Mach number, $(u^2 + v^2)^{1/2}/c$ .
P	Static pressure.
$P_B$	Base pressure.
$P_{T_2}$	Pitot pressure.
$p_B$	Base pressure coefficient, $(P_B - P_\infty)/q_\infty$ .
Pr	Prandtl number, $\mu C_p/k$ .
$\vec{q}$	Heat flux vector.
$\dot{q}_x, \dot{q}_r$	Heat flux in the axial and radial directions.
R	Gas constant for air.
Re	Reynolds number, $\rho(u^2 + v^2)^{1/2}L/\mu$ .
r	Spatial coordinate normal to the nozzle centerline.
$r_{gr}$	Length of the computational grid in the radial direction.
$r_m$	Mach disc radius.
S	Fluid stress tensor that includes pressure and viscous forces.
T	Absolute temperature.
t	Time.

## LIST OF SYMBOLS (Cont'd)

$t_{ch}$	Characteristic time, Equation 84.
$U$	Conservative flow variable vector, Equation 28.
$\vec{u}$	Velocity vector.
$u$	Velocity component along the x axis.
$u_{ch}$	Characteristic velocity, Equation 84.
$u^+$	Nondimensional velocity component, $u/(\tau_w/\rho)^{1/2}$ .
$V$	Volume.
$v$	Velocity component along the r axis.
$x$	Spatial coordinate parallel to the nozzle centerline.
$x_r$	Mach disc reflection length.
$x_{gr}$	Length of the computational grid in the axial direction.
$y$	Spatial coordinate normal to the x axis in a two-dimensional flow.
$y_B$	Radial thickness of the nozzle base annulus.
$y^+$	Nondimensional height, $y(\tau_w/\rho)^{1/2}/\nu$ .

## GREEK SYMBOLS:

$\alpha_\eta, \alpha_\xi$	Damping coefficients in the $\eta$ and $\xi$ directions.
$\gamma$	Ratio of specific heats, $C_p/C_v$ .
$\delta$	Flow deflection angle, Section I.
$\delta$	Momentum boundary layer thickness.
$\delta^*$	Momentum boundary layer displacement thickness.
$\delta_{ij}$	Kronecker delta, equal to 0 if $i \neq j$ or equal to 1 if $i = j$ .
$\epsilon$	Turbulent eddy viscosity coefficient.
$\eta$	Transformed coordinate normal to the nozzle centerline.
$\Delta$	Designates a finite difference when used as a prefix.
$\theta$	Local flow angle, $\arctan(v/u)$
$\theta$	Boundary layer momentum thickness, Appendix C.

LIST OF SYMBOLS (Cont'd)

$\lambda$	Viscosity diffusion coefficient, Equation 37.
$\lambda_I$	Left running characteristic line.
$\mu$	Absolute viscosity coefficient.
$\mu_M$	Mach angle of supersonic flow, Equation 49.
$\nu$	Kinematic viscosity, $\mu/\rho$ .
$\xi$	Transformed coordinate parallel to the nozzle centerline.
$\rho$	Fluid density.
$\sigma$	Normal stress on an element of fluid, Equations 29-31.
$\tau_{xr}$	Shear stress, Equation 32.
$\omega$	Vorticity.

SUBSCRIPTS:

aw	Adiabatic wall.
e	Evaluated at the edge of the boundary layer.
i,j	Grid point indices.
i,j	Indicial notation Section II.
j	Evaluated in the jet flow.
n	Normal to the nozzle wall.
s	Tangent to the nozzle wall.
t	Turbulent flow.
tr	Transition from regular shock reflection to Mach disc reflection.
w	Evaluated in the wake.
o	Stagnation value.
$\infty$	Evaluated in the external freestream.

LIST OF SYMBOLS (Concluded)

SUPERSCRIPITS:

$n$	Evaluated at known time, $n\Delta t$ .
$n+1/2$	Evaluated at intermediate predictor time level, $(n+1/2)\Delta t$ .
$n+1$	Evaluated at new corrector time level, $(n+1)\Delta t$ .
$o$	Evaluated at time level $t=0$ .

OTHER NOTATION:

$(^=)$	Denotes a two-dimensional matrix.
$(^-)$	Denotes time averaged values, Section II.
$( )'$	Denotes unsteady values due to turbulence, Section II.



## SUMMARY

The use of computational analysis in the design of propulsive nozzle installations has recently expanded as advanced digital computers have been developed which result in lowering computational costs versus actual wind tunnel test costs. Although a range of numerical techniques has been applied in this area, only those utilizing the full Navier-Stokes equations across the flow domain have successfully simulated the viscous phenomena associated with aft-end flowfields. Navier-Stokes methods are particularly useful for predicting off-design nozzle characteristics where the overexpanded or underexpanded flowfield is more complex and where viscous regions are more prevalent than at on-design conditions. One feature typical of these off-design conditions is the appearance of a strong normal shock wave referred to as a Mach disc. Viscous nozzle flowfields containing this phenomenon have not been adequately simulated in the past. This research details the development of a numerical Navier-Stokes method capable of accurately predicting nozzle flowfields which contain both highly viscous regions and complex shock structures typified by the Mach disc formation.

Numerical solutions to the Navier-Stokes equations are obtained for a domain containing an axisymmetric nozzle in a supersonic external stream ( $M_\infty = 1.94$ ,  $M_{jet} = 3.0$ ,  $Re_\infty = 2.2 \times 10^6$ ). Five nozzle pressure ratio conditions ranging from a highly overexpanded case ( $P_j/P_\infty = 0.15$ ) which exhibits a Mach disc shock formation, to a slightly underexpanded case ( $P_j/P_\infty = 1.59$ ) are examined and solved numerically. The weak conservative form of the two-dimensional (axisymmetric), time dependent Navier-Stokes equations is solved using MacCormack's explicit finite difference method. This algorithm is an efficient Lax-Wendroff type differencing scheme of second order accuracy which utilizes time-splitting and two-step predictor-corrector techniques. An adaptive grid scheme is utilized in the wake of the nozzle base annulus that allows the fine mesh region of the computational grid to remain in the mixing layer containing high flow gradients as each solution progresses towards convergence. Appropriate numerical boundary conditions are applied that allow the computational domain to be restricted to a

compact region surrounding the nozzle. Locally dependent eddy viscosity modelling is applied in the form of a Cebeci-Smith two-layer model in the boundary layer regions on the nozzle walls, and a form of the Prandtl mixing length model in the nozzle wake region.

The numerical solutions successfully reproduced all of the essential nozzle flow features including boundary layers, corner expansions, recompression shocks, the separated recirculation region along the nozzle base wall, and the evolution of the near wake to a far wake type of flow. Correct transition from regularly reflected shock waves at the line of symmetry in the jet core to the strong Mach disc shock reflection was numerically achieved, as was the simulation of the subsonic embedded region immediately behind the Mach disc shock structure. Numerically obtained nozzle base pressure coefficients were within seven percent of the experimentally determined values for all cases where the attached flow assumption in the divergent portion of the nozzle was valid.

Present solution times for 2,500 point grids are on the order of two to four hours when run on a Cyber 750 computer. A fully vectorized version of the present computer code can be expected to converge within five minutes on a CRAY-1 computer for similar grids, allowing the computation of more complex nozzle geometries and better resolution in the boundary layers through the use of a finer mesh in future efforts.

## SECTION I

### INTRODUCTION

#### 1. BACKGROUND

The increased importance of the aft-end drag problem associated with nozzle installations in current and future high performance aircraft has led to extensive and very costly experimental nozzle test programs. Any technique which can reduce this requirement for wind tunnel testing in the design of nozzle installations will result in a significant savings to the technical community of both time and resources.

Computational aerodynamics shows great promise as a field which can have a favorable impact on this requirement for nozzle design information. Current computational techniques in this area utilize advanced digital computers to simulate the flowfield surrounding the nozzle at projected flight conditions. It has been shown that boundary layer and shear layer growth, areas of separated flow, shock wave formation and interactions, and jet plume blockage and entrainment characteristic of nozzle flows can be analyzed using computational techniques. Unlike experimental testing, computational analysis is not necessarily restricted by wind tunnel Reynolds number or nozzle exhaust temperature limitations. Flowfields analyzed computationally can also eliminate the undesirable effects of support stings and test section walls that occur during experimental testing. As more advanced computers are developed, the cost of numerically analyzing a given nozzle configuration is decreasing. Since the cost of wind tunnel testing is steadily increasing, computational analysis is being utilized more extensively.

Several of the first computational solutions to include viscous effects inherent to aft end or nozzle flowfields consisted of patching techniques that divided the field into predominantly inviscid and viscous regions. Grossman and Melnik (Reference 1), and Cosner and Bower (Reference 2) obtained transonic boattail nozzle solutions using iterative techniques that divided the flowfield into an inviscid free-stream, an inviscid jet, and a viscous boundary layer and mixing layer region. The freestream solution procedure assumed irrotational potential

flow that could be solved by a relaxation algorithm applied to the potential flow equations. The rotational inviscid supersonic jet was solved using a hyperbolic marching technique. Imbedded shocks in the jet were explicitly fitted to satisfy the Rankine-Hugoniot equations. The viscous mixing region was assumed to be isobaric and was solved using integral techniques. Each region was solved separately and patched together iteratively using pressure and flow direction conditions at the common boundaries. Separation regions could not be accounted for, so equivalent fitted body blending was used to obtain reasonable flow solutions.

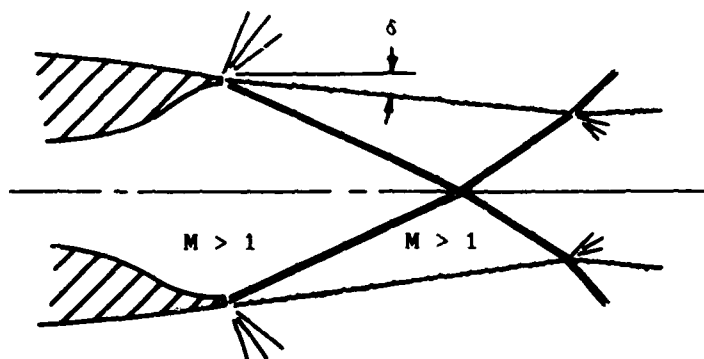
Pergament, Dash, and Wilmoth (Reference 3) introduced a displacement thickness correction to the inviscid plume boundary to account for the effects of jet entrainment on the inviscid external flow calculation. Their analysis also included the effects of species mixing and pressure gradients in the mixing region, but still could only account for separation regions by body blending techniques. Yeager (Reference 4) attempted to include a fourth separation region involving recirculating flow that was defined by a dividing streamline which connected separation and reattachment points. The extent of this region was determined using local control volume analyses, and it was found that reasonable reattachment points could only be predicted through the application of empirical corrections during the solution procedure. Although these iteratively patched solutions gave reasonable results for specific data sets, the required amount of empirical matching and explicit fitting limits the use of this type of computational method as a predictive technique.

A more adaptable method of simulating the viscous-inviscid interactions that occur in typical nozzle flowfields involves solving the time dependent, compressible Navier-Stokes equations uniformly over the entire nozzle flowfield. This approach has a direct advantage over the previously discussed iteratively patched methods where an accurate viscous-inviscid matching procedure is required in order to obtain reasonable results. In the direct approach, the predominantly inviscid and viscous flow regions are computed simultaneously with no matching required. Holst (Reference 5) used this approach to solve for supersonic

flow over axisymmetric boattail nozzles with plume simulators. Although a plume simulator does not model the entrainment and blockage of a jet plume, its flowfield does contain phenomena characteristic to nozzles such as turbulent boundary layers, recompression shock waves, and separated recirculating regions of flow. Holst's solutions were obtained using MacCormack's explicit finite difference algorithm, a stretched mesh aligned with the solid body through an analytic transformation and a two-layer eddy viscosity model to account for the Reynold's stresses that included a relaxation formula to model the separated flow region. Pressure distributions, skin friction coefficients and areas of separated flow were in good agreement with experimental data, particularly in the cases where a fine mesh was utilized. Mikhail (Reference 6) recently computed solutions for viscous supersonic flow around an axisymmetric boattail nozzle with a jet exhaust flow. MacCormack's explicit method was again used as the numerical algorithm, together with a surface oriented mesh system obtained through a numerical mapping procedure. Reynold's stresses were also accounted for through the application of algebraic eddy viscosity models. Reasonable agreement with experimental surface pressure data on the boattail was obtained.

Navier-Stokes solutions are especially useful for predicting the off-design nozzle characteristics where the flowfield is in either a significantly overexpanded or underexpanded state. At these conditions the flow structure is usually more complex with viscous regions becoming more prevalent than at on-design conditions. One feature typical of these off-design conditions is the establishment of a triple-point in the jet flow, and the appearance of a strong normal shock wave referred to as a Mach disc in axisymmetric flow or a Riemann wave in two-dimensional flow (Figure 1). This strong shock formation occurs when the deflection angle of the jet flow is large enough so that the resulting shock wave is too strong for a regular reflection at the centerline to exist. Near the centerline the Mach disc must be normal, since this is the only way a shock can occur without any change in flow direction. As shown in Figure 2, both the Mach disc and the reflected shock are curved near the triple point (Reference 7). A slip line emanates from the triple point, and the flow downstream of the Mach disc and reflected shock is

### REGULAR REFLECTION



### MACH REFLECTION

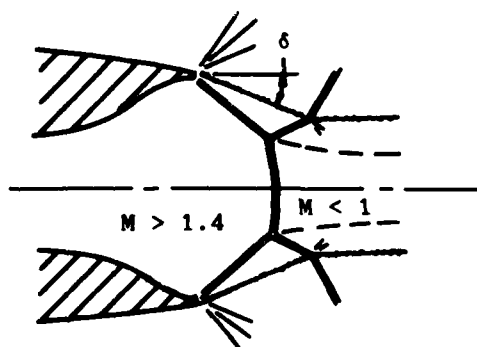


Figure 1. Shock Structure for a Typical Overexpanded Axisymmetric Nozzle

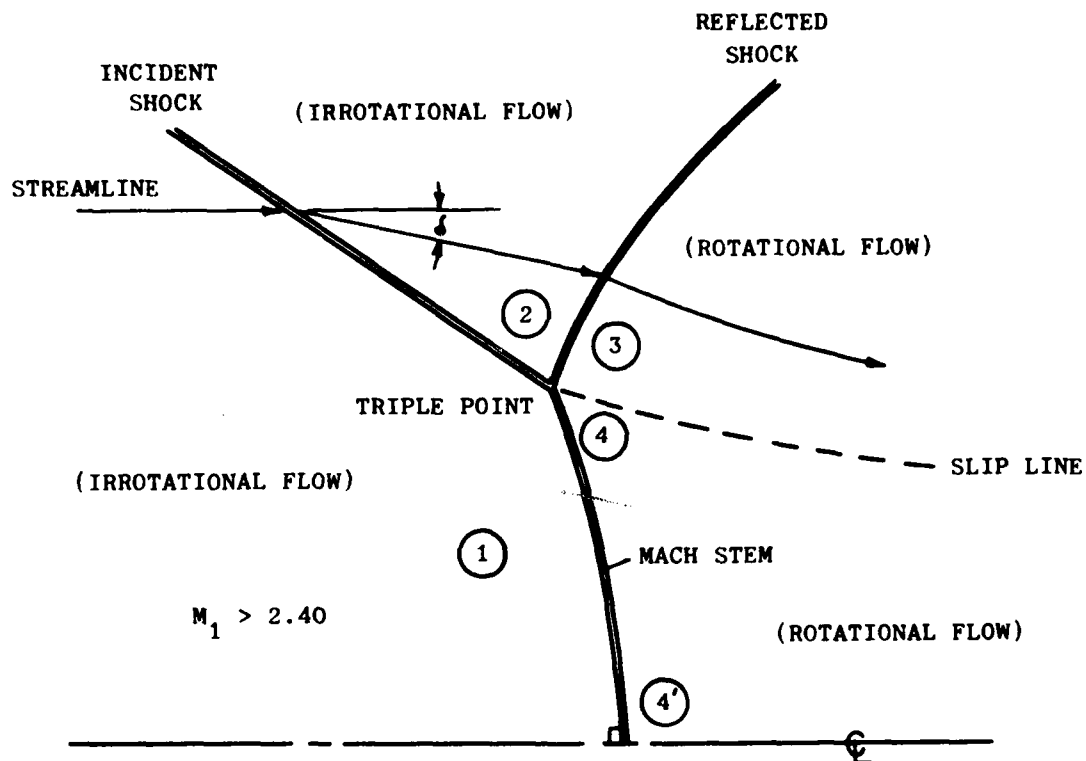


Figure 2. Schematic of a Typical Mach Reflection

rotational in nature due to the curvature of the shocks. As discussed by Henderson and Lozzi (Reference 8), this region downstream of the shocks may be either totally subsonic or contain both supersonic and subsonic regions. If the incident Mach number  $M_1$  is greater than 2.40, region 3 will be supersonic, while region 4 remains subsonic. Since the jet Mach numbers relevant to this investigation are greater than 2.40, the latter case in which a subsonic core only exists behind the Mach disc will be examined.

The transition from regular to Mach reflections can also be examined using a hodograph diagram shown in Figure 3. For deflection angles less than the transition angle ( $\delta_{tr}$ ), the flow can be brought to the required zero deflection at state 3 through a weak regular wave reflection. For deflection angles greater than the transition angle, the flow in region 3 cannot achieve a zero deflection state, and lies on the strong shock portion of the initial shock polar. The flow near the centerline passes through a strong normal shock to condition 4' with no deflection occurring. The flow state at the curved Mach disc then exists along the strong shock portion of the incident shock polar from a zero deflection state 4' near the centerline to a deflected state 4 near the triple point with a pressure and flow angle equal to that in region 3, but with different velocity and entropy values that generate the slip line.

The mixed supersonic-subsonic flow region surrounding the Mach disc greatly complicates the analysis of nozzle flowfields in which this shock structure is present. Flowfields containing this phenomena have not been adequately simulated in the past using viscous techniques. A variety of techniques for locating the triple point and the resulting normal shock have been presented that utilize an iterative combination of the method of characteristics and schemes involving approximate analyses such as pressure requirements downstream of the strong shock (References 9 and 10) or one-dimensional flow calculations downstream through a throat region in the flow (References 11 and 12). Although each of these methods give reasonable results for determining the triple point location and size of the resulting Mach disc, each is only valid for a limited range of nozzle pressure ratios and jet Mach numbers. In addition, none of these techniques



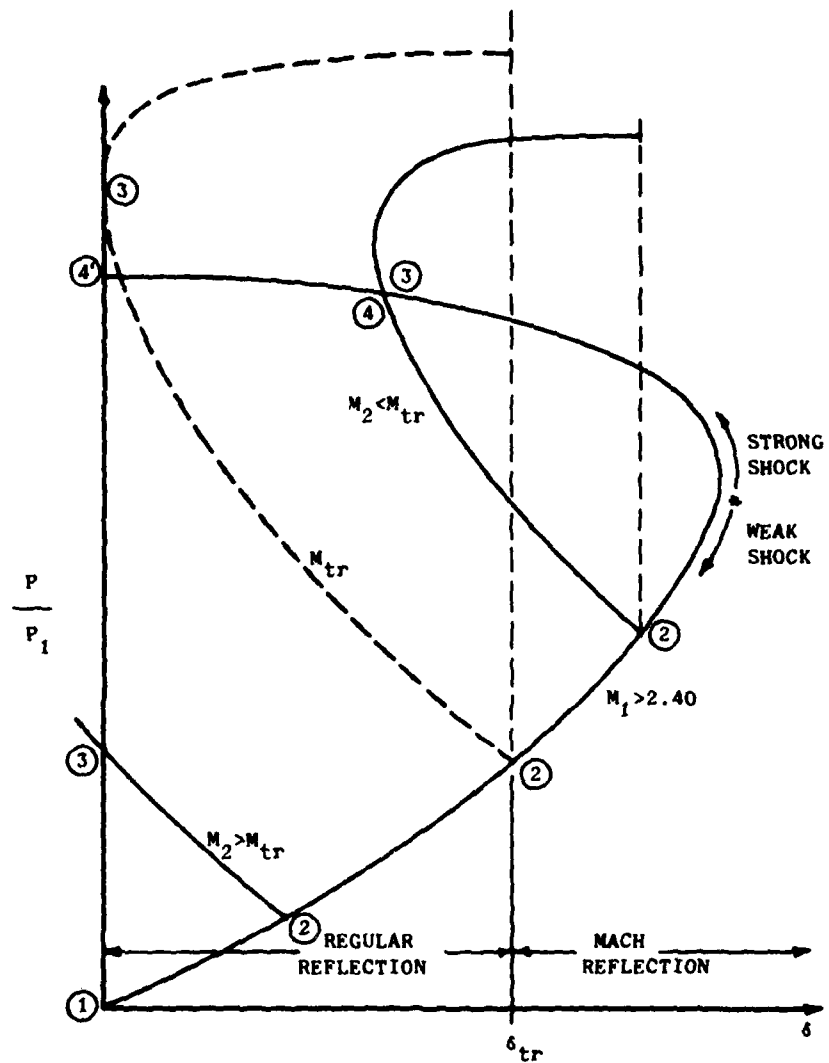


Figure 3. Hodograph Diagram Showing Shock Polar Intersections for Transition from Regular to Mach Reflection

give a solution for the subsonic core region downstream of the normal shock. At least two time-dependent inviscid techniques have been used to overcome the deficiencies of the semi-empirical methods previously mentioned. Jofre (Reference 13) performed a finite difference technique for an underexpanded jet with a Mach disc solution. A method of characteristics solution was used in the plume expansion region near the nozzle exit. This gave an upstream flow profile used in the time dependent solution further downstream. Sinha, Zakkay, and Erdos (Reference 14) analyzed a two-dimensional underexpanded jet containing a strong normal shock using a finite difference technique over the entire flowfield of interest. Both of these investigations used versions of Lax-Wendroff numerical algorithms and simple square grids. These solutions were much more adaptable than the previous semi-empirical techniques since the flow tends to adjust to its local environment so that the proper shock structure is automatically obtained as the solution develops. However, these solutions represent only a first approximation of the correct viscous solution (Reference 15), particularly in the region downstream of the normal shock as shown in Figure 4. Flow properties in this region were found to be heavily dependent on the level of damping used in the solution algorithm. For example, Jofre (Reference 13) found that an unrealistic region of reverse flow was generated immediately behind the normal shock unless heavy damping was applied in the solution procedure.

All of these inviscid solutions involved jets exhausting into a quiescent atmosphere. Solutions were not attempted for the more complex case of a nozzle in which the external flow stream interacts with the jet. A full Navier-Stokes solution which accounts for the viscous effects present in the flowfield at these off-design conditions is necessary in order to adequately simulate both the strong-shock structure with its resulting imbedded subsonic flow region as well as the interaction of the jet plume with the external flowfield.

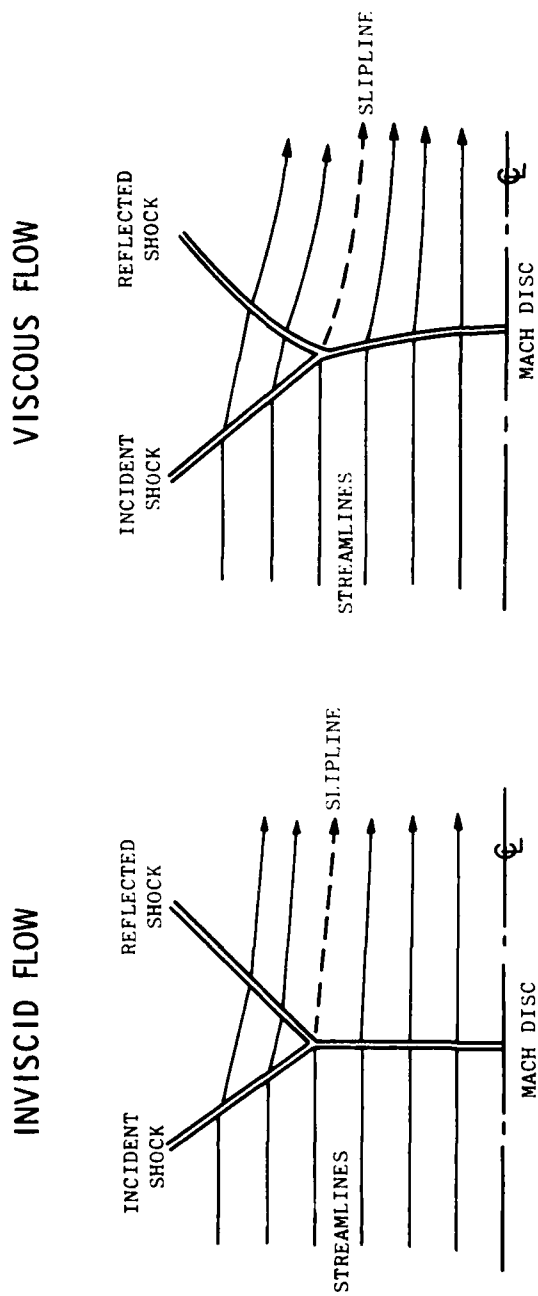


Figure 4. Viscous Effects on the Mach Disc Structure

## 2. RESEARCH OBJECTIVES

The primary objective of this research is the development of a numerical Navier-Stokes method capable of accurately predicting nozzle flowfields which contain both highly viscous regions and complex shock structure typified by the Mach disc shock formation. Overexpanded axisymmetric nozzles will primarily be simulated, since they meet the previous criteria while possessing fairly compact flow domains which contain the flow phenomena of interest. The experimental data of Bromm and O'Donnell (Reference 16) has been chosen as a basis for comparison in this research effort. Data in this reference is given for an axisymmetric Mach three isentropic nozzle embedded in a turbulent Mach 1.94 external flowfield as shown in Figure 5. Nozzle pressure ratios ranging from a slightly underexpanded condition to a highly overexpanded condition which exhibits the Mach disc structure were obtained experimentally. This particular nozzle possesses a relatively thick base annulus which generates a strong viscous-inviscid interaction in the near wake region of the nozzle. These interactions affect the development of the primarily inviscid shock structure, and can only be analyzed properly using a full Navier-Stokes methodology.

Although Mikhail achieved full Navier-Stokes solutions for an axisymmetric boattail nozzle, he was not able to generate an accurate solution for the condition at which a Mach disc shock structure was shown to exist experimentally (Reference 6). Possible causes of this inability to generate the strong shock structure include boundary condition formulation, mesh spacing and turbulence modeling. These three areas will be concentrated on in the present investigation in order to achieve the desired goal of an accurate predictive technique for both on-design and off-design nozzle performance.

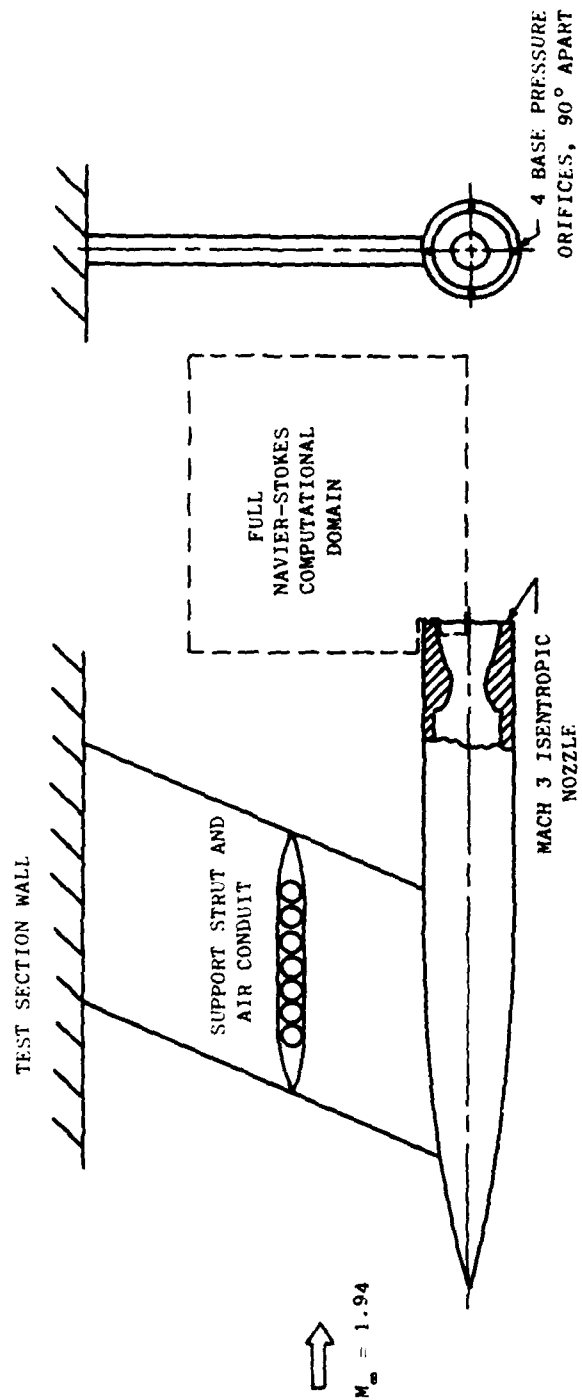


Figure 5. Schematic of the Axisymmetric Jet Model Used as a Basis for the Computational Solutions

## SECTION II

## MATHEMATICAL DESCRIPTION OF THE FLOW STRUCTURE

## 1. GOVERNING EQUATIONS

The governing equations for flows containing the shock and viscous phenomena of interest are the conservation equations for mass, momentum, and energy known as the Navier-Stokes equations. The gases involved are assumed to be single component, have constant specific heats, and obey the perfect gas equation of state:

$$P = \rho RT \quad (1)$$

In computational fluid dynamics, the Eulerian method is usually applied to the problem of interest. This method involves a fixed control volume that is specified relative to a given coordinate system. Properties of the fluid are then specified as functions of both time and space. The conservation equations are approached using this methodology.

## a. Conservation of Mass

For a given system in which matter is neither created or destroyed, the law of mass conservation can be written as

$$\iiint_V \left( \frac{\partial \rho}{\partial t} + \nabla \cdot \rho \vec{u} \right) dV = 0 \quad (2)$$

where  $V$  is an arbitrary volume fixed in space.

## b. Conservation of Momentum

For a given system, the law of momentum conservation states that the rate of change of momentum is equal to the sum of the external forces acting on the control volume. If body forces are neglected, this law can be written as:

$$\iiint_V \left[ \frac{\partial (\rho \vec{u})}{\partial t} + \nabla \cdot (\rho \vec{u} \vec{u}) \right] dV = \iiint_V (\nabla \cdot \vec{S}) dV \quad (3)$$

The variable  $\bar{\bar{S}}$  denotes a stress tensor involving pressure and viscous forces which acts on the fluid.

c. Conservation of Energy

The law of conservation of energy states that for a given system which does not contain any internal heat sources, the rate of change of the total energy of the system is equal to the heat added into the system plus the work done on the system by viscous and pressure forces. This can be stated as

$$\iiint_V \left[ \frac{\partial(\rho e)}{\partial t} + \nabla \cdot (\rho e) \vec{u} \right] dV = \iiint_V (\nabla \cdot \vec{u} \cdot \bar{\bar{S}} - \nabla \cdot \vec{q}) dV \quad (4)$$

Since these conservation equations are valid for any arbitrary volume  $V$ ; when the integrands are continuous, these equations imply that:

$$\partial \rho / \partial t + \nabla \cdot \rho \vec{u} = 0 \quad (5)$$

$$\partial(\rho \vec{u}) / \partial t + \nabla \cdot (\rho \vec{u}) \vec{u} - \nabla \cdot \bar{\bar{S}} = 0 \quad (6)$$

$$\partial(\rho e) / \partial t + \nabla \cdot (\rho e) \vec{u} + (\nabla \cdot \vec{q} - \nabla \cdot \vec{u} \cdot \bar{\bar{S}}) = 0 \quad (7)$$

It should be noted that these equations are written in conservative form where, for the two-dimensional and axisymmetric flows of interest, the applicable dependent variables are  $\rho$ ,  $\rho u$ ,  $\rho v$ , and  $\rho e$ . As shown by Roache (Reference 17), this conservative form allows the finite difference equations to preserve the Gauss divergence property of the continuum equations. This form allows a balance between the flux quantities and accumulation rates for a small control volume. Roache also states that the Rankine-Hugoniot shock relations were derived using the conservative form. Thus, shock jump conditions are automatically satisfied since the conservative variables are continuous across the shock and need no special treatment because of discontinuities. This approach is known as shock capturing or shock smearing. The conservation form of the equations then allows the finite difference formulation to satisfy the physical laws

on a macroscopic scale, not merely in some academic limit as  $\Delta x$ ,  $\Delta y$ , and  $\Delta t$  approach zero.

Since the flowfields of interest are turbulent, the solution of the conservation equations must take into account the effects of the random fluctuations of the dependent variables inherent to turbulent flows. In accounting for these effects, Cartesian tensor notation will be applied. The usual conventions of a repeated subscript indicating summation over the entire range of indices and a comma representing partial differentiation will be used to make the equations compact. Cartesian tensors are used to allow working directly with the physical components, while still being applicable to the 2-D and axisymmetric systems of interest. The conservation Equations 5 through 7 can then be written as:

$$\rho_{,t} + (\rho u_j)_{,j} = 0 \quad (8)$$

$$(\rho u_i)_{,t} + (\rho u_i u_j + \delta_{ij} P - \tau_{ij})_{,j} = 0 \quad (9)$$

$$(\rho e)_{,t} + (\rho e u_j + \dot{q}_j - u_i \tau_{ij})_{,j} = 0 \quad (10)$$

where the stress tensor  $S_{ij}$  has been expanded in the form:

$$S_{ij} = -P\delta_{ij} + \tau_{ij} \quad (11)$$

The dependent variables in the conservation equations can be expanded into the following form:

$$u = \bar{u} + u' \quad (12a)$$

$$v = \bar{v} + v' \quad (12b)$$

$$P = \bar{P} + P' \quad (12c)$$

$$\rho = \bar{\rho} + \rho' \quad (12d)$$

$$e = \bar{e} + e' \quad (12e)$$



In these expansions the barred variables represent time averaging over a time interval that is long compared to turbulent eddy fluctuations, yet small compared to macroscopic flow changes. The primed variables then represent fluctuations due to the turbulent nature of the flow. As discussed by Chapman (Reference 18), this time averaging approach is valid since the frequencies of most unsteady flows of interest are a factor of 10 to 100 below the mean frequency of the turbulent eddy motion.

If the dependent variables  $u$ ,  $v$ , and  $e$  are mass averaged as described in Reference 19, and  $\rho$  and  $P$  are mean (time averaged) state variables, then the conservation equations can be written in the form of mean flow equations as:

$$\bar{\rho}_{,t} + (\bar{\rho}\bar{u}_j)_{,j} = 0 \quad (13)$$

$$(\bar{\rho}\bar{u}_1)_{,t} + [(\bar{\rho}\bar{u}_1\bar{u}_j) + \bar{P}\delta_{1j} - (\bar{\tau}_{1j} - \overline{\rho u'_1 u'_j})]_{,j} = 0 \quad (14)$$

$$(\bar{\rho}e)_{,t} + [\bar{\rho}e\bar{u}_j + \bar{q}_j + \overline{\rho u'_j e'} - \bar{u}_1 (\bar{\tau}_{1j} - \overline{\rho u'_1 u'_j})]_{,j} = 0 \quad (15)$$

where a higher order mean energy dissipation term in  $u'_j$  has been neglected in the energy Equation 15.

The term  $[-\overline{\rho u'_1 u'_j}]$  is known as the Reynolds stress. It represents a momentum transfer caused by turbulent fluctuations present in the flow-field. This Reynolds stress term can be written as an apparent stress caused by the turbulent nature of the flow:

$$\tau_{1j}|_{\text{turb}} = -\overline{\rho u'_1 u'_j} \quad (16)$$

Since air is essentially an isotropic fluid, the mean stress term can be expanded into its normal and shear stress components as:

$$\bar{\tau}_{1j} = \lambda \bar{u}_{k,k} \delta_{1j} + \mu (\bar{u}_{1,j} + \bar{u}_{j,1}) \quad (17)$$

The turbulent stress term can then be written in analogous form as:

$$\bar{\tau}_{ij}|_{\text{turb}} = \lambda_t \bar{u}_{k,k} \delta_{ij} + \epsilon (\bar{u}_{i,j} + \bar{u}_{j,i}) \quad (18)$$

where  $\lambda_t$  and  $\epsilon$  are the turbulent viscosity coefficients of the flow. The coefficient  $\epsilon$  is known as the eddy viscosity, and is analogous to the molecular viscosity coefficient  $\mu$ . However,  $\epsilon$  is more a property of the dynamics of the flow, whereas  $\mu$  is only a property of the fluid. Combining the mean and turbulent stress terms, an overall stress term can be written as:

$$\bar{\tau}_{ij}|_{\text{total}} = (\lambda + \lambda_t) \bar{u}_{k,k} \delta_{ij} + (\nu + \epsilon) (\bar{u}_{i,j} + \bar{u}_{j,i}) \quad (19)$$

In the energy equation an additional unsteady term appears. This term is by nature an apparent heat flux caused by the fluctuations inherent to turbulent flow and can be written as:

$$\bar{\dot{q}}_j|_{\text{turb}} = \overline{\rho u'_j e'} \quad (20)$$

If the heat flux term  $\bar{\dot{q}}_j$  is defined by the Fourier heat equation as:

$$\bar{\dot{q}}_j = -k \bar{T}_{,j} = - (C_p \mu / Pr) \bar{T}_{,j} \quad (21)$$

then by the former analogy  $\bar{\dot{q}}_j|_{\text{turb}}$  can be written as:

$$\bar{\dot{q}}_j|_{\text{turb}} = - (C_p \epsilon / Pr_t) \bar{T}_{,j} \quad (22)$$

where again  $\epsilon$  is the eddy viscosity coefficient, and  $Pr_t$  is the turbulent Prandtl number of the flow. Combining these two heat fluxes, a total heat flux can be written as:

$$\bar{\dot{q}}_{j \text{ total}} = -C_p (\nu / Pr + \epsilon / Pr_t) \bar{T}_{,j} \quad (23)$$

The mean conservation equations can then be written in the following form, where the overbars on the terms are dropped for convenience, and where the values of the shear stresses and heat fluxes are the total values:

$$\rho_{,t} + (\rho u_j)_{,j} = 0 \quad (24)$$

$$(\rho u_1)_{,t} + [(\rho u_1) u_j + P \delta_{1j} - \tau_{1j}]_{,j} = 0 \quad (25)$$

$$(\rho e)_{,t} + [(\rho e) u_j + \dot{q}_j - u_1 \tau_{1j}]_{,j} = 0 \quad (26)$$

Since the flowfields of interest are either two-dimensional or axisymmetric in nature, the mean conservation equations can be written in the following compact vector form:

$$\frac{\partial U}{\partial t} + \frac{\partial F}{\partial x} + \frac{1}{r^{j_0}} \frac{\partial (r^{j_0} G)}{\partial r} = j_0 \cdot \frac{H}{r^{j_0}} \quad (27)$$

where  $j_0 = 0$  or  $1$  for either the two dimensional or axisymmetric cases, respectively, and

$$U = \begin{pmatrix} \rho \\ \rho u \\ \rho v \\ \rho e \end{pmatrix} ; \quad F = \begin{pmatrix} \rho u_2 \\ \rho u - \sigma_{xx} \\ \rho v - \tau_{xr} \\ \rho e + \dot{q}_x - u \sigma_{xx} - v \tau_{xr} \end{pmatrix} \quad (28)$$

$$G = \begin{pmatrix} \rho v \\ \rho u v - \tau_{xr} \\ \rho v^2 - \sigma_{rr} \\ \rho e + \dot{q}_r - u \tau_{xr} - v \sigma_{rr} \end{pmatrix} ; \quad H = \begin{pmatrix} 0 \\ 0 \\ -\sigma_H \\ 0 \end{pmatrix}$$

where

$$\sigma_{xx} = -P + (\lambda + \lambda_t) \operatorname{div} \vec{u} + 2(\mu + \epsilon) \frac{\partial u}{\partial x} \quad (29)$$

$$\sigma_{rr} = -P + (\lambda + \lambda_t) \operatorname{div} \vec{u} + 2(\mu + \epsilon) \frac{\partial v}{\partial r} \quad (30)$$

$$\sigma_H = -P + (\lambda + \lambda_t) \operatorname{div} \vec{u} + 2(\mu + \epsilon) \frac{v}{r} \quad (31)$$

$$\tau_{xr} = (\mu + \epsilon) \left( \frac{\partial u}{\partial r} + \frac{\partial v}{\partial x} \right) \quad (32)$$

$$\dot{q}_x = -C_p \left( \frac{\mu}{Pr} + \frac{\epsilon}{Pr_t} \right) \frac{\partial T}{\partial x} \quad (33)$$

$$\dot{q}_r = -C_p \left( \frac{\mu}{Pr} + \frac{\epsilon}{Pr_t} \right) \frac{\partial T}{\partial r} \quad (34)$$

and

$$\operatorname{div} \vec{u} = \frac{\partial u}{\partial x} + \frac{\partial v}{\partial r} + j_0 \frac{v}{r} \quad (35)$$

The coefficient of viscosity  $\mu$  for air can be assumed to vary according to Sutherland's law (Reference 19):

$$\mu = (2.27 \cdot 10^{-8}) T^{1.5} / (T + 198.6) \text{ (lbf - sec/ft}^4\text{)} \quad (36)$$

The second coefficient of viscosity is assumed as the following by applying Stokes Hypothesis:

$$(\lambda + \lambda_t) = -2/3 (\mu + \epsilon) \quad (37)$$

The governing equations for the problem of interest now consist of the four conservation equations in matrix form (Equation 27) with four unknown dependent variables  $\rho$ ,  $\rho u$ ,  $\rho v$  and  $\rho e$ . The perfect gas law is used to define the pressure in terms of these conservative variables, and a model of the dependence of the eddy viscosity on the mean flow must be introduced to overcome the "turbulent closure" problem inherent in the turbulent mean conservation equations.

For numerical computation in a transformed  $(\xi, \eta)$  Cartesian plane, the matrix form of the conservation equations (Equation 27) can be written as:

$$\begin{aligned} \frac{\partial U}{\partial \tau} + \left[ \xi_x \frac{\partial F}{\partial \xi} + \frac{1}{r j_0} \xi_r \frac{\partial (r^j \circ G)}{\partial \xi} \right] \\ + \left[ \eta_x \frac{\partial F}{\partial \eta} + \frac{1}{r j_0} \eta_r \frac{\partial (r^j \circ G)}{\partial \eta} \right] = j_0 \frac{H}{r j_0} \end{aligned} \quad (38)$$

where  $\xi$  and  $\eta$  are now the independent variables, and the transformation derivatives  $\xi_x$ ,  $\xi_r$ ,  $\eta_x$ , and  $\eta_r$  are obtained numerically from a mapping procedure. Equation 38 is actually in weak conservation form due to the varying coefficients in front of the derivatives, and also due to the source term in the axisymmetric case.

## 2. BOUNDARY AND INITIAL CONDITIONS

Boundary and initial conditions must be given in order to solve the conservation equations which govern the flowfield. These conditions must be carefully specified, since many flow features such as shock waves, boundary layers, and recirculation areas arise from boundary conditions. For the solution of a symmetric two-dimensional or axisymmetric supersonic jet embedded in a supersonic external flowfield, the domain of interest can be defined as shown in Figure 6. Only one-half of the total nozzle flowfield needs to be considered due to the axis of symmetry on the jet centerline. The remainder of this chapter will detail the specific boundary conditions that are pertinent to this problem.

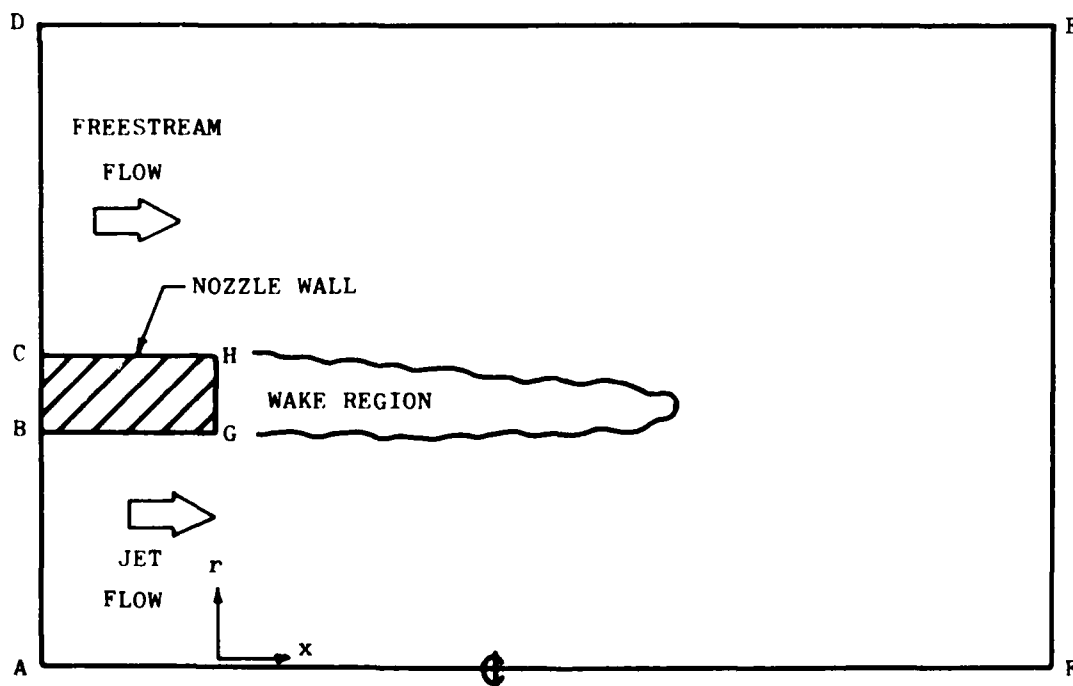


Figure 6. Physical Domain for the Computational Solutions

## a. The Upstream Boundary

Inflow conditions on the upstream jet boundary (AB) and the upstream external boundary in the freestream (CD) are completely specified. Velocity, pressure, and temperature profiles determined from auxiliary computations or known experimentally on this boundary fix  $\rho$ ,  $\rho u$ ,  $\rho v$ , and  $\rho e$  for the duration of the problem solution at the boundary.

## b. The Upper Boundary

The upper boundary (DE) must accurately represent a free flight condition where mass flow is allowed across this boundary embedded in the supersonic external flowfield. Weak shock waves and Prandtl-Meyer expansion waves must also exit this boundary without being reflected artificially back into the domain of interest. One condition that allows this is the assumption of a simple wave solution:

$$\left. \frac{\partial u}{\partial \lambda_1} \right|_{DE} = 0 \quad (39)$$

where  $\lambda_1$  is the straight left running characteristic line passing through each point on the upper boundary. This characteristic line is determined only by the value of the Mach number and flow angle of the supersonic flow present near the upper boundary. This condition assumes that the flow along this boundary is inviscid and homentropic.

## c. The Downstream Boundary

The downstream boundary (EF) is unique in that no rigorous assumptions can be made about either the variables or their gradients unless the boundary is placed a great distance downstream. In this case a no change condition

$$\left. \frac{\partial f}{\partial x} \right|_{EF} = 0 \quad (40)$$

could be assumed, where  $f$  denotes the primitive variables  $\rho$ ,  $u$ ,  $v$ , and  $T$ . For the case where the downstream boundary is placed where gradients do exist, an extrapolation method based on this fact can be reasonably

applied. One such method is to assume that a flow gradient accurate to second order can exist. This can be implemented as:

$$\left( \Delta x \frac{\partial^3 f}{\partial x^3} \right) \Big|_{EF} = 0 \quad (41)$$

In other words, gradients can occur which are parabolic with respect to  $x$ . This condition is reasonable if the gradients at this boundary are not severe as in the case where a strong shock wave exits the boundary.

d. The Centerline

The centerline boundary (AF) is a line of symmetry with no mass or energy flux across it. Therefore, the following boundary conditions can be applied

$$v \Big|_{AF} = 0 \quad (42)$$

$$\frac{\partial \rho}{\partial r} \Big|_{AF} = 0 \quad (43)$$

$$\frac{\partial u}{\partial r} \Big|_{AF} = 0 \quad (44)$$

Since the  $v$  component of velocity is zero on the centerline, this boundary is also a streamline in the jet flow. For steady, adiabatic flow with negligible volume forces, the total enthalpy along any streamline is a constant. Therefore, along the centerline,

$$h_o \Big|_{AF} = \left( C_p T + \frac{u^2}{2} \right) \Big|_{AF} = \text{constant} \quad (45)$$

Since the condition at the jet exit is specified, the centerline boundary can be properly posed using this approach.

AFWAL-TR-81-3161

e. Nozzle Walls

The nozzle walls (BG, GH, and CH) are considered to be no-slip, impermeable boundaries. This assumption gives the conditions that:

$$u|_{\text{wall}} = 0 \quad (46a)$$

and

$$v|_{\text{wall}} = 0 \quad (46b)$$

Since the stainless steel nozzle consists of thin-walled material with a thermal conductivity much greater than that of the surrounding fluid, the nozzle walls are assumed to be at a constant temperature:

$$T|_{\text{wall}} = \text{constant} \quad (47)$$

This wall temperature is determined by applying a heat flux balance across the jet and freestream boundary layers as outlined in Appendix A.

The pressure on each nozzle wall is unknown, but can be approximated by applying the degenerate form of the appropriate normal momentum equation at each nozzle surface to obtain the following:

$$\frac{\partial p}{\partial n}|_{\text{wall}} = \frac{\partial \tau_{sn}}{\partial s}|_{\text{wall}} = 0 \quad (48)$$

In this expression  $n$  is the directional normal to the wall surface, and  $s$  is the direction parallel to the surface.

f. Initial Conditions

Since the governing equations contain time dependent terms, initial conditions must be specified before the solution process can begin. The specification of these initial conditions is somewhat arbitrary in nature, although steep gradients must be avoided to prevent numerical divergence during the solution process. Since the flow is predominantly supersonic in nature, the incoming flow profiles will have a dominant effect on the solution in the whole computational domain. The incoming flow conditions are imposed on the complete domain as discussed in the section on initial condition implementation of Section IV.



AFWAL-TR-81-3161

### SECTION III

#### NUMERICAL PROCEDURE

The numerical procedure consists of solving the governing equations with applicable boundary and initial conditions through the use of appropriate finite difference techniques on a high-speed computer. This procedure can be broken down into several elements which include the finite difference coordinate system, the solution algorithm, and the convergence criteria used in the computational solution. Each of these areas will be discussed in this chapter.

#### 1. COORDINATE SYSTEM

##### a. Domain of Computation

The physical domain of computation consists of a rectangular area defined by orthogonal coordinates (x,r) as shown in Figure 7. The mesh consists of IL points on the x axis and JL points on the r axis, where IL and JL are dependent on the extent of the physical domain required for the particular jet plume case of interest.

##### b. Mesh Stretching

In order to obtain an accurate numerical solution of a viscous flowfield, the mesh spacing must be much finer in areas containing relatively high gradients of the variable properties such as velocity, density, and temperature. In the nozzle flowfield these high gradient areas include the boundary layers on the nozzle walls and the shear layer in the wake of the nozzle annulus. This stretching is accomplished through the use of a patched exponential stretching scheme of the following form:

$$r(j) = L_m \frac{e^{Cn(j)} - 1}{(e^C - 1)} \text{ for } j = 1, N \quad (49)$$

where  $L_m$  and  $n$  are defined as shown in Figure 8. The constant  $C$  is determined by the minimum spacing  $\Delta r_{\min}$  desired for the mesh next to the wall boundary. Applying the desired  $\Delta r_{\min}$  to Equation 49 gives

$$C = \frac{1}{\Delta \eta} \log_e \left( 1 + \frac{\Delta r_{\min}}{L_m} (e^C - 1) \right) \quad (50)$$

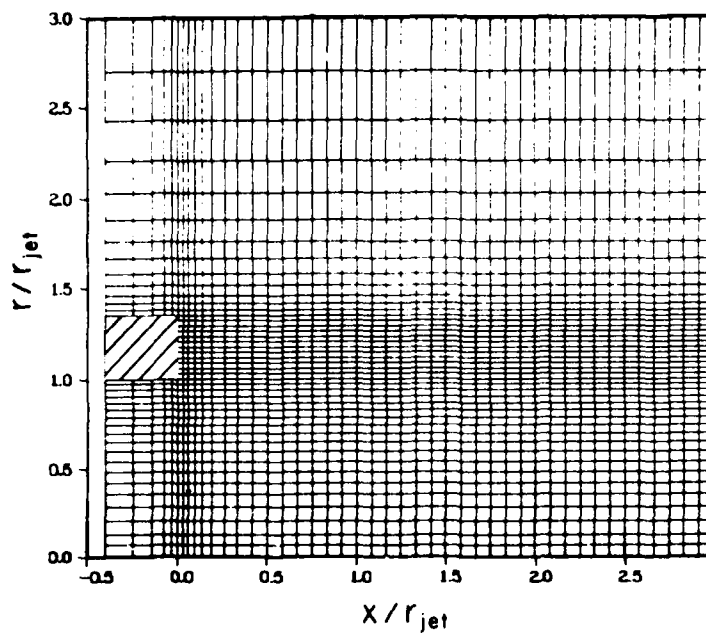


Figure 7. Finite Difference Mesh in Physical Space

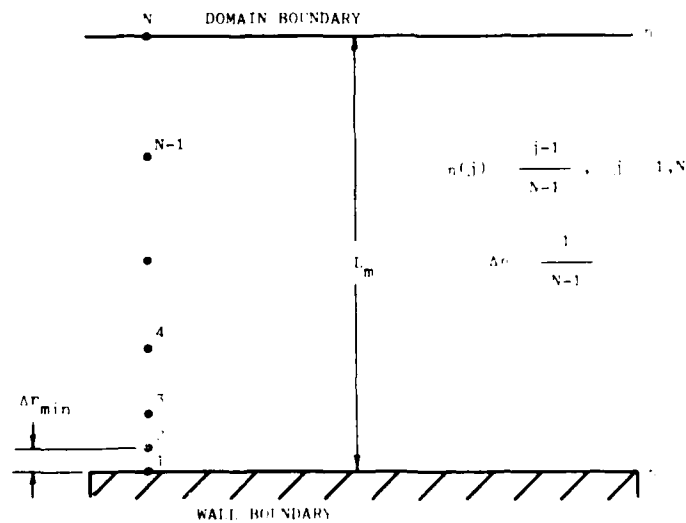


Figure 8. Exponentially Stretched Mesh Schematic

The value of  $C$  is then obtained through the use of an iterative Aitken extrapolation technique.

This mesh stretching procedure is applied in the radial direction on both sides of the nozzle wall where boundary layers are present. It is also applied in the axial direction at the end of the nozzle where the jet flow begins to expand or contract and where the near wake due to the nozzle annulus begins to form.

#### c. Adaptive Mesh

It is desirable that the fine mesh remain in the areas of relatively high velocity and temperature gradients as the solution progresses towards convergence. This is not a problem in the case of boundary layers that are adjacent to a fixed wall, but is a concern in the free shear layer area generated by the nozzle wake and the interaction between the jet and freestream flows. This shear region on the jet plume boundary will deflect to a degree that is primarily dependent on the nozzle pressure ratio. The fine mesh region should therefore also be adapted to conform to the general position of the shear region.

Hirt (Reference 21) has used a technique in the solution of free surface flows that allows the grid to adapt as the solution progresses. The following kinematic equation is applied in the region where the shear layer is present.

$$\frac{\partial r}{\partial t} = C_A (v - u \frac{\partial r}{\partial x}) \quad (51)$$

This equation insures the condition that as the solution converges, the physical slope of the constant  $n$  finite difference cell boundaries is the same as that of the velocity vectors near each cell. When applied in a finite difference format, the grid can then adapt to the placement of the shear layer as shown in Figure 9. Details of this process are explained in Appendix B.

#### d. Coordinate Transformation

The physical domain as typically shown in Figure 9 is mapped to a unit square in the computational plane shown in Figure 10. The constant  $\eta$  lines are aligned parallel to the centerline and the constant  $\xi$  lines are in the direction normal to the centerline. The numerical algorithm

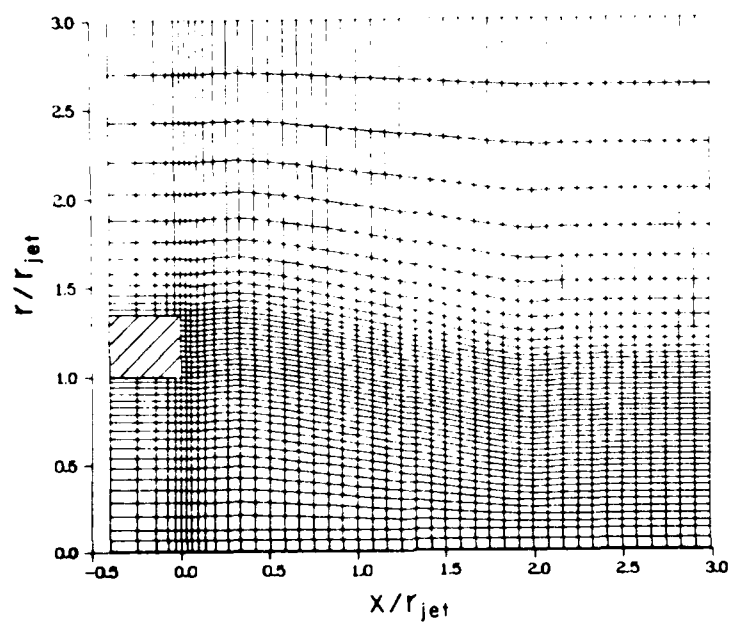


Figure 9. Adaptive Finite Difference Mesh,  $P_j/P_\infty = 0.150$

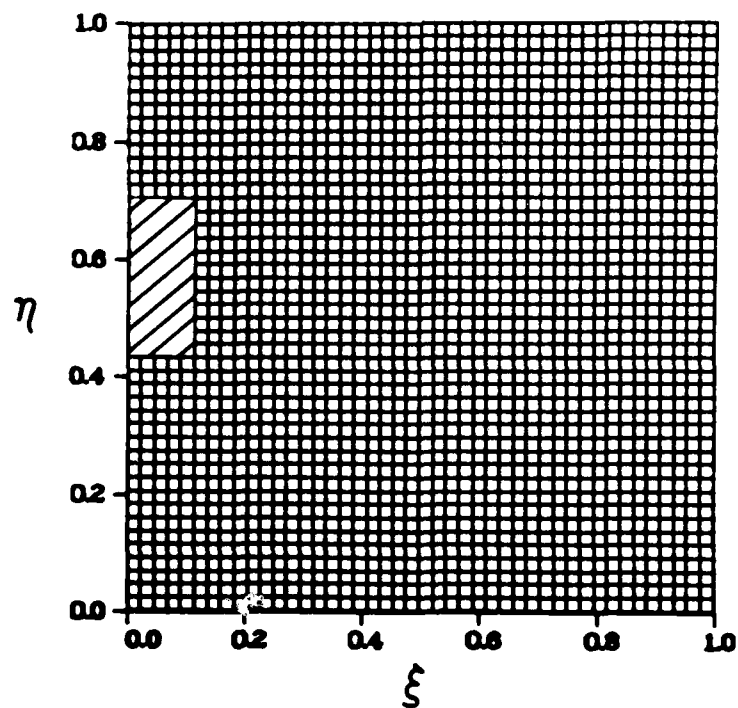


Figure 10. Computational Mesh in the Transformed Plane

operates on this coordinate system using the transformed conservation equations (Equation 38). Care must be taken in generating the physical mesh so that smoothness of the transformation coefficients ( $\xi_x$ ,  $\xi_r$ ,  $\eta_x$ , and  $\eta_r$ ) is retained in order to reduce numerical errors caused by the mesh configuration.

## 2. SOLUTION ALGORITHM

### a. MacCormack's Method

The weak conservative form of the two-dimensional, time-dependent Navier-Stokes Equations (Equation 38) is solved using MacCormack's explicit finite difference method (Reference 22). This algorithm is an efficient Lax-Wendroff type differencing scheme of second order accuracy which utilizes time-splitting and two step predictor-corrector techniques. MacCormack's algorithm was chosen for application to the nozzle problem because of its previous success in computing inviscid-viscous interacting flows, its stability in supersonic flow, and its computational efficiency achieved by time-splitting the finite difference operators.

The computational solution is advanced in time by applying the numerical operator to the solution of the flowfield at time  $t$ . This can be written as:

$$U(\xi, \eta, t + \Delta t) = L(\Delta t) \cdot U(\xi, \eta, t) \quad (52)$$

where  $L(\Delta t)$  is the two-dimensional numerical operator representing MacCormack's algorithm acting on the transformed conservation equations. Through the use of a time-splitting technique, this two-dimensional operator  $L(\Delta t)$  is separated into two one-dimensional sweep operators in the  $\xi$  and  $\eta$  directions. The operator  $L_\xi(\Delta t)$  denotes the solution of the equation:

$$\frac{\partial U}{\partial t} + \xi_x \frac{\partial F}{\partial \xi} + \frac{1}{r^{j_0}} \xi_r \frac{\partial (r^{j_0} G)}{\partial \xi} = 0 \quad (53)$$

in the  $\xi$  direction by time increment  $\Delta t$  seconds. Similarly, the operator  $L_\eta(\Delta t)$  represents the solution of

$$\frac{\partial U}{\partial t} + \eta_x \frac{\partial F}{\partial \eta} + \frac{1}{r j_\phi} \eta_r \frac{\partial (r j_\phi G)}{\partial \eta} = j_\phi \frac{H}{r j_\phi} \quad (54)$$

in the  $\eta$  direction by a time increment  $\Delta t$  seconds. The dependent variable vector  $U(\xi, \eta, t)$  can then be advanced in time as

$$U(\xi, \eta, t + \Delta t) = [L_\xi^{M/2}(\Delta t/M) \cdot L_\eta(\Delta t) \cdot L_\xi^{M/2}(\Delta t/M)] \cdot U(\xi, \eta, t) \quad (55)$$

with

$$\Delta t = \Delta t_\xi \quad \text{if} \quad \Delta t_\xi < \Delta t_\eta$$

or as

$$U(\xi, \eta, t + \Delta t) = [L_\eta^{N/2}(\Delta t/N) \cdot L_\xi(\Delta t) \cdot L_\eta^{N/2}(\Delta t/N)] \cdot U(\xi, \eta, t) \quad (56)$$

with

$$\Delta t = \Delta t_\eta \quad \text{if} \quad \Delta t_\eta < \Delta t_\xi$$

In these equations  $M$  and  $N$  are the smallest even integers of the quotients  $(\Delta t_\eta / \Delta t_\xi)$  and  $(\Delta t_\xi / \Delta t_\eta)$ , respectively, and  $\Delta t_\xi$  and  $\Delta t_\eta$  are the maximum allowable time steps in the  $\xi$  and  $\eta$  directions as determined by the Courant-Friedrichs-Lewy (CFL) limit discussed in the next section on stability. The values of  $M$  and  $N$  are usually equal to two for the grid distribution used in the solution of the nozzle problem. This sets up a truly alternating direction procedure that is desirable when gradients exist in more than one direction.

The finite difference forms of the sweep operators consist of a predictor-corrector procedure which increases the accuracy of the time-dependent term evaluations. This method utilizes one-sided differencing in the direction of sweep, but central differencing in the direction perpendicular to the sweeping coordinate. At the completion of the predictor-corrector process, this method is equivalent to a second order central differencing scheme in two dimensions.

The  $L_{\xi}(\Delta t)$  sweep operator represents the following numerical procedure. A predicted intermediate value is computed by the expression:

$$U_{i,j}^{n+1/2} = U_{i,j}^n - \frac{\Delta t}{\Delta \xi} [(\xi_x)_{i,j} (F_{i,j}^n - F_{i-1,j}^n) + \frac{1}{r_{i,j}^{j_0}} (\xi_r)_{i,j} (r_{i,j}^{j_0} G_{i,j}^n - r_{i-1,j}^{j_0} G_{i-1,j}^n)] \quad (57)$$

where  $U_{i,j}^n$  is the known value at time  $t$ , and  $U_{i,j}^{n+1/2}$  is the intermediate predictor value. The actual computed value at time  $(t+\Delta t)$  is then calculated by applying the following corrector algorithm:

$$U_{i,j}^{n+1} = 1/2 \{ U_{i,j}^n + U_{i,j}^{n+1/2} - \frac{\Delta t}{\Delta \xi} [(\xi_x)_{i,j} (F_{i+1,j}^{n+1/2} - F_{i,j}^{n+1/2}) + \frac{1}{r_{i,j}^{j_0}} (\xi_r)_{i,j} (r_{i+1,j}^{j_0} G_{i+1,j}^{n+1/2} - r_{i,j}^{j_0} G_{i,j}^{n+1/2})] \} \quad (58)$$

In this  $\xi$  sweep predictor-corrector algorithm, the matrices  $F$  and  $G$  are functions of the following difference quotients:

$$F_{i,j}^m, G_{i,j}^m = \delta (U_{i,j}^m, \frac{U_{i+1,j}^m - U_{i,j}^m}{\Delta \xi}, \frac{U_{i,j+1}^m - U_{i,j-1}^m}{2\Delta \eta}) \quad (59)$$

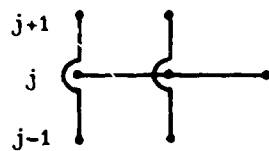
This scheme can be depicted graphically as shown in Figure 11.

The  $L_{\eta}(\Delta t)$  numerical sweep operator is formulated in a similar manner. The intermediate predictor value is given by the expression:

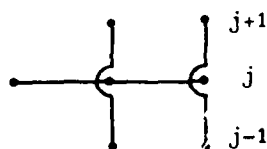
$$U_{i,j}^{n+1/2} = U_{i,j}^n - \frac{\Delta t}{\Delta \eta} [(\eta_x)_{i,j} (F_{i,j}^n - F_{i,j-1}^n) + \frac{1}{r_{i,j}^{j_0}} (\eta_r)_{i,j} (r_{i,j}^{j_0} G_{i,j}^n - r_{i,j-1}^{j_0} G_{i,j-1}^n)] + \frac{j_0 \Delta t H_{i,j}^n}{r_{i,j}^{j_0}} \quad (60)$$

# $\xi$ SWEEP

PREDICTOR

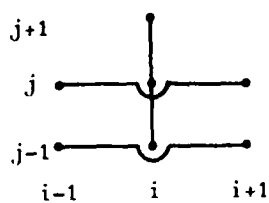


CORRECTOR



# $\eta$ SWEEP

PREDICTOR



CORRECTOR

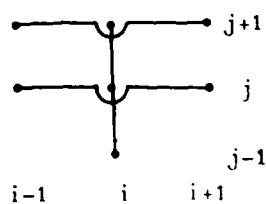


Figure 11. Graphical Representation of the Numerical Sweep Operators



The corrector value at time  $(t+\Delta t)$  is then given by:

$$U_{1,j}^{n+1} = 1/2 \left\{ U_{1,j}^n + U_{1,j}^{n+1/2} - \left( \frac{\Delta t}{\Delta \eta} \right) [(\eta_x)_{1,j} (F_{1,j+1}^{n+1/2} - F_{1,j}^{n+1/2}) + \frac{1}{r_{1,j}^{j_0}} (\eta_r)_{1,j} (r_{1,j+1}^{j_0} G_{1,j+1}^{n+1/2} - r_{1,j}^{j_0} G_{1,j}^{n+1/2})] + \frac{j_0 \Delta t H_{1,j}^{n+1/2}}{r_{1,j}^{j_0}} \right\} \quad (61)$$

The matrices  $F$  and  $G$  are now functions of the following difference quotients:

$$F_{1,j}^m, G_{1,j}^m = (U_{1,j}^m, \frac{U_{1+1,j}^m - U_{1-1,j}^m}{2\Delta \xi}, \frac{U_{1,j+1}^m - U_{1,j}^m}{\Delta \eta}) \quad (62)$$

This scheme is also depicted graphically in Figure 11.

The MacCormack algorithm satisfies the requirements of stability, consistency, and accuracy if the following conditions are met: It is stable if the time step limit satisfies the CFL stability condition given in the next section. It is consistent if the sum of the time steps for each of the sweep operators is equal, and the algorithm is second order accurate if the sequence of sweep operators is symmetric.

#### b. Stability Condition

Although the stability of the finite difference equations cannot be analyzed when applied to the complete set of Navier-Stokes equations, MacCormack and Baldwin (Reference 23) have shown that considerable insight can be gained by separately analyzing the inviscid, diffusion, and mixed derivative parts of these equations. Stability criteria are determined by calculating the eigenvalues of the associated amplification matrix for each part. If this eigenvalue procedure is applied to the inviscid

terms of the Navier-Stokes equations for flow in a Cartesian coordinate system, the following stability conditions emerge:

$$\Delta t_x \leq \frac{\Delta x}{|u| + c} \quad (63)$$

and

$$\Delta t_r \leq \frac{\Delta r}{|v| + c} \quad (64)$$

where  $c$  is the local speed of sound. Consideration of only the diffusive terms which contain  $\partial^2 U / \partial x^2$  and  $\partial^2 U / \partial r^2$  in the complete Navier-Stokes equations gives the conditions:

$$\Delta t_x \leq 1/2 \frac{\Delta x^2}{\frac{\gamma}{\rho} \left( \frac{\mu}{Pr} + \frac{\epsilon}{Pr_t} \right)} \quad (65)$$

and

$$\Delta t_r \leq 1/2 \frac{\Delta r^2}{\frac{\gamma}{\rho} \left( \frac{\mu}{Pr} + \frac{\epsilon}{Pr_t} \right)} \quad (66)$$

Finally, analysis of the mixed derivative terms found in the Navier-Stokes equations gives the condition:

$$\Delta t_x = \Delta t_r \leq \frac{\Delta x \Delta r}{\frac{1}{\rho} [-(\lambda + \lambda_r) (\mu + \epsilon)]^{1/2}} \quad (67)$$

For the finite difference equations applied to the complete set of Navier-Stokes equations, the stability criteria can then be estimated as:

$$\Delta t \leq \underset{i,j}{\text{minimum}} (\Delta t_x, \Delta t_r) \quad (68)$$

where

$$\Delta t_x \leq \frac{\Delta x}{|u| + c + \frac{1}{\rho} \left\{ \frac{2\gamma}{\Delta x} \left( \frac{\mu}{Pr} + \frac{\epsilon}{Pr_t} \right) + \frac{1}{\Delta x} [-(\lambda + \lambda_t)(\mu + \epsilon)]^{1/2} \right\}} \quad (69)$$

and

$$\Delta t_r \leq \frac{\Delta r}{|v| + c + \frac{1}{\rho} \left\{ \frac{2\gamma}{\Delta r} \left( \frac{\mu}{Pr} + \frac{\epsilon}{Pr_t} \right) + \frac{1}{\Delta r} [-(\lambda + \lambda_t)(\mu + \epsilon)]^{1/2} \right\}} \quad (70)$$

For the present non-Cartesian jet flow cases that were computed, the maximum time step was calculated as:

$$\Delta t = K_{cfl} \cdot \underset{i,j}{\text{minimum}} (\Delta t_\xi, \Delta t_\eta) \quad (71)$$

where

$$\Delta t_\xi = \frac{\Delta S_\xi}{|u_\xi| + c + \frac{1}{\rho} \left\{ \frac{2\gamma}{\Delta S_\xi} \left( \frac{\mu}{Pr} + \frac{\epsilon}{Pr_t} \right) + \frac{1}{\Delta S_\xi} [-(\lambda + \lambda_t)(\mu + \epsilon)]^{1/2} \right\}} \quad (72)$$

and

$$\Delta t_\eta = \frac{\Delta S_\eta}{|u_\eta| + c + \frac{1}{\rho} \left\{ \frac{2\gamma}{\Delta S_\eta} \left( \frac{\mu}{Pr} + \frac{\epsilon}{Pr_t} \right) + \frac{1}{\Delta S_\eta} [-(\lambda + \lambda_t)(\mu + \epsilon)]^{1/2} \right\}} \quad (73)$$

where

$$\Delta S_\xi = [(x_{i,j} - x_{i-1,j})^2 + (r_{i,j} - r_{i-1,j})^2]^{1/2} \quad (74)$$

$$\Delta S_\eta = [(x_{i,j} - x_{i,j-1})^2 + (r_{i,j} - r_{i,j-1})^2]^{1/2} \quad (75)$$

$$u_\xi = \text{Maximum} (u_{i,j}, v_{i,j}, u_{i-1,j}, v_{i-1,j}) \quad (76)$$

$$u_\eta = \text{Maximum} (u_{i,j}, v_{i,j}, u_{i,j-1}, v_{i,j-1}) \quad (77)$$

CFL factors,  $K_{cfl}$ , varying between 0.35 and 0.80 were used during the computations. Flow solutions involving relatively large viscous wakes containing recirculation regions required much smaller allowable time-steps with CFL factors on the order of 0.35-0.40.

### c. Numerical Damping

Strong shocks imbedded in a flowfield being solved computationally can often cause numerical oscillations (Reference 17) which may lead to program failure due to physically unrealistic values of computed pressure, density or temperature (Gibb's phenomenon). These oscillations are caused by numerical truncation errors and can be reduced by refining the grid in the areas of shock locations. However, this can be impractical when the oscillations are of a transient nature caused by computational start-up or re-start procedures, or where the shock location varies for different experimental cases and mesh refinement for each individual case is undesirable. In this situation, a fourth order pressure-gradient damping concept as introduced by MacCormack and Baldwin (Reference 23) can be applied to increase the stability of the numerical algorithm by adding artificial viscosity.

This damping scheme is applied in both the  $\xi$  and  $\eta$  directional sweeps. In the  $\xi$  numerical sweep, damping is implemented by replacing  $F_{ii,j}$  by  $(F_{ii,j} + F_{D_{ii,j}})$  and  $G_{ii,j}$  by  $(G_{ii,j} + G_{D_{ii,j}})$  in Equation 53. The predictor and corrector steps in this case are represented by  $ii=i$  and  $ii = i+1$ , respectively. The damping terms  $F_D$  and  $G_D$  are in the following form:

$$F_{D_{ii,j}} = \alpha_{\xi} (|u_{ii,j}| + c_{ii,j}) \frac{|P_{i+1,j} - 2P_{i,j} + P_{i-1,j}|}{(P_{i+1,j} + 2P_{i,j} + P_{i-1,j})} \quad (78)$$

and 
$$\cdot (U_{i+1,j} - U_{i,j})$$

$$G_{D_{ii,j}} = \alpha_{\eta} (|v_{ii,j}| + c_{ii,j}) \frac{|P_{ii,j+1} - 2P_{ii,j} + P_{ii,j-1}|}{(P_{ii,j+1} + 2P_{ii,j} + P_{ii,j-1})} \quad (79)$$

$$\cdot (U_{ii,j+1} - U_{ii,j-1}) \cdot r_{ii,j}^j$$

In the  $\eta$  sweep, a similar procedure is implemented by replacing  $F_{i,jj}$  by  $(F_{i,jj} + F_{D_{i,jj}})$  and  $G_{i,jj}$  by  $(G_{i,jj} + G_{D_{i,jj}})$  where

$$F_{D_{i,jj}} = \alpha_{\xi} (|u_{i,jj}| + c_{i,jj}) \frac{|P_{i+1,jj} - 2P_{i,jj} + P_{i-1,jj}|}{(P_{i+1,jj} + 2P_{i,jj} + P_{i-1,jj})} \cdot (U_{i+1,jj} - U_{i-1,jj}) \quad (80)$$

and

$$G_{D_{i,jj}} = \alpha_{\eta} (|v_{i,jj}| + c_{i,jj}) \frac{|P_{i,j+1} - 2P_{i,j} + P_{i,j-1}|}{(P_{i,j+1} + 2P_{i,j} + P_{i,j-1})} \cdot (U_{i,j+1} - U_{i,j}) \cdot r_{i,jj}^j \quad (81)$$

In this case the predictor and corrector steps are represented by  $jj = j$  and  $jj = j+1$ , respectively. For both sweeps  $\alpha_{\xi}$  and  $\alpha_{\eta}$  are damping constants where normally

$$\alpha_{\xi} = \alpha_{\eta} = 0.5 \quad (82)$$

This damping technique produces fourth order viscosity like terms of the form

$$\alpha_{\xi} \Delta t \Delta \xi^3 \frac{\partial}{\partial \xi} \left[ \frac{|u|+c}{4P} \left| \frac{\partial^2 P}{\partial \xi^2} \right| \frac{\partial U}{\partial \xi} \right] + \alpha_{\eta} \Delta t \Delta \eta^3 \frac{\partial}{\partial \eta} \left[ \frac{|v|+c}{4P} \left| \frac{\partial^2 P}{\partial \eta^2} \right| \frac{\partial U}{\partial \eta} \right]$$

which are added to the difference equations. The magnitude of these damping terms is proportional to the second derivative of pressure and is significant only in regions of pressure oscillation where the truncation error is already adversely affecting the solution.

### 3. CONVERGENCE CRITERIA

Convergence, as applied in this section, refers to iteration convergence as opposed to truncation convergence, which involves the convergence of the solution of the FDE to the solution of the PDE as  $\Delta x$ ,  $\Delta r$ , and  $\Delta t \rightarrow 0$ . Iteration convergence refers to the arrival at a

solution to the discretized Navier-Stokes equations within some acceptable tolerance through the use of an iterative process. As stated by Roache (Reference 17), there are no definitive criteria for iteration convergence. A somewhat subjective judgement of convergence must be made based upon an examination of the iterative behavior of the solution flow variables. Different flow variables, as well as variables at different locations, converge at different rates. If the slowest converging variable in the flowfield is known, it should be the most closely examined for convergence.

In the present case for a coflowing supersonic nozzle with a relatively thick base annulus, an examination of the flow variables revealed that the slowest converging variable was the base pressure of the nozzle annulus. The location of this base pressure is within the subsonic flow area involving recirculation in the wake of the nozzle annulus as shown in Figure 12. The flow variables in this subsonic region converged much more slowly than did those in the predominantly supersonic jet and free-stream flows.

Since the coflowing nozzle problem primarily involves high Reynolds number flow, the advective terms in the conservation equations dominate the viscous diffusion terms. A characteristic time for a disturbance to cross the flowfield may then be characterized by:

$$t_{ch} = \frac{L}{u_{ch}} \quad (83)$$

where  $L$  is the length of the flowfield in the direction parallel to the characteristic velocity  $u_{ch}$ . For the jet problem  $u_{ch}$  was represented by  $u_{\infty}$ . Since in general the magnitude of  $u_{\infty}$  was less than  $u_{jet}$ , this gave a more conservative estimate of the characteristic time.

The convergence criteria was then established by the following procedure. The numerical solution was either initially started, or restarted from a previous case. As the solution converged, the base pressure was monitored until its magnitude varied less than  $\pm 1\%$  for one characteristic time period. At the end of this characteristic time period the solution was stopped as convergence was achieved. Visual comparison

of Mach Number and density profiles over the flowfield confirmed the convergence of the solution using this procedure. A sample base pressure convergence plot is shown in Figure 13.

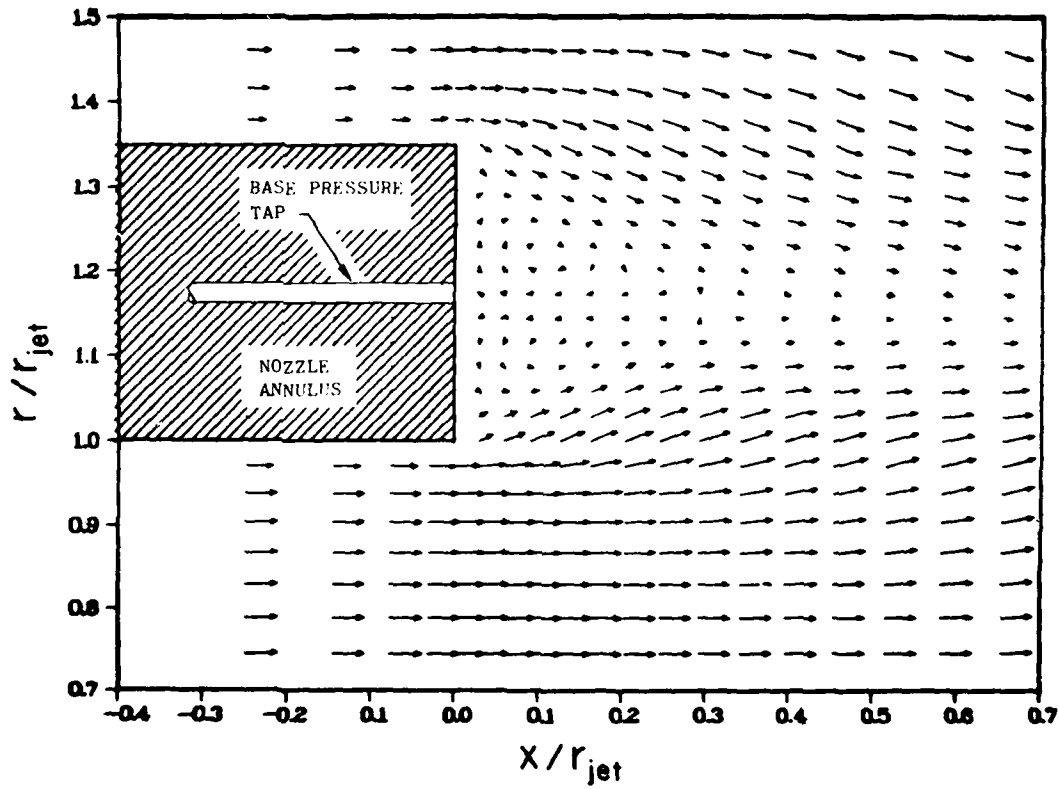


Figure 12. Base Pressure Tap Location in the Flowfield

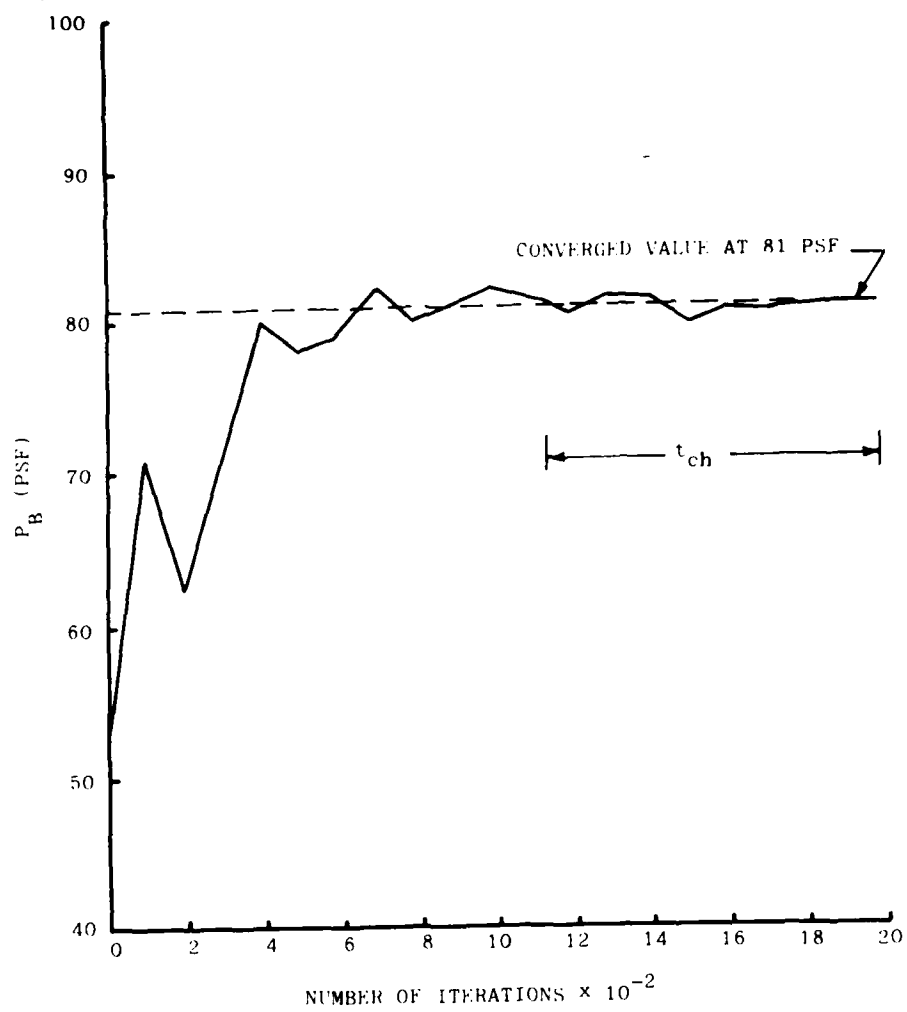


Figure 13. Typical Base Pressure Convergence,  $P_j/P_\infty = 0.527$



## SECTION IV

## BOUNDARY AND INITIAL CONDITION IMPLEMENTATION

As in Section II, boundary and initial conditions must be defined in order to solve the conservation equations which govern the flowfield. Values of the dependent variables for points on the boundaries of the computational domain must be specified in order for the numerical operators to solve the flowfield correctly. This section presents the numerical formulation of the boundary and initial conditions used for the solution of the axisymmetric nozzle. The conditions were presented in a mathematical context in Section II.

## 1. THE UPSTREAM BOUNDARY

The flow properties on the upstream boundary (AB and CD of Figure 6) are held fixed for the duration of the computational solution. The values of these properties were derived in the following manner. In the external flowfield, a parabolized Navier-Stokes solution (Reference 24) was computed for the ogive body used in the experimental nozzle tests as shown in Figure 14. This solution determined that the pressure gradient at the inflow boundary in the external flow stream is negligible, and that the static pressure at the inflow boundary is 99% of that in the undisturbed flow in the wind tunnel. The static pressure along the ogive body surface shown in Figure 15 was then used as an input to a two-dimensional turbulent boundary layer code (References 25 and 26) along with the other specified freestream conditions ( $M_\infty$ ,  $T_{0\infty}$ ,  $Re_\infty$ ,  $T_w$ ) to produce input velocity component and temperature profiles at the upstream boundary. The conservative variables on this boundary (CD) are then calculated using these profiles and the static pressure along the boundary. Flow variables on the upstream boundary in the jet flow (AB) are determined in a similar manner. The same boundary layer code is applied using the jet exit conditions and the length from the nozzle throat to the nozzle exit plane as the boundary layer starting length. Again, profiles for the velocity components and temperature are obtained along the boundary. Values for the conservative variables are then computed using these profiles and the value of the pressure at the jet exit. Since the value

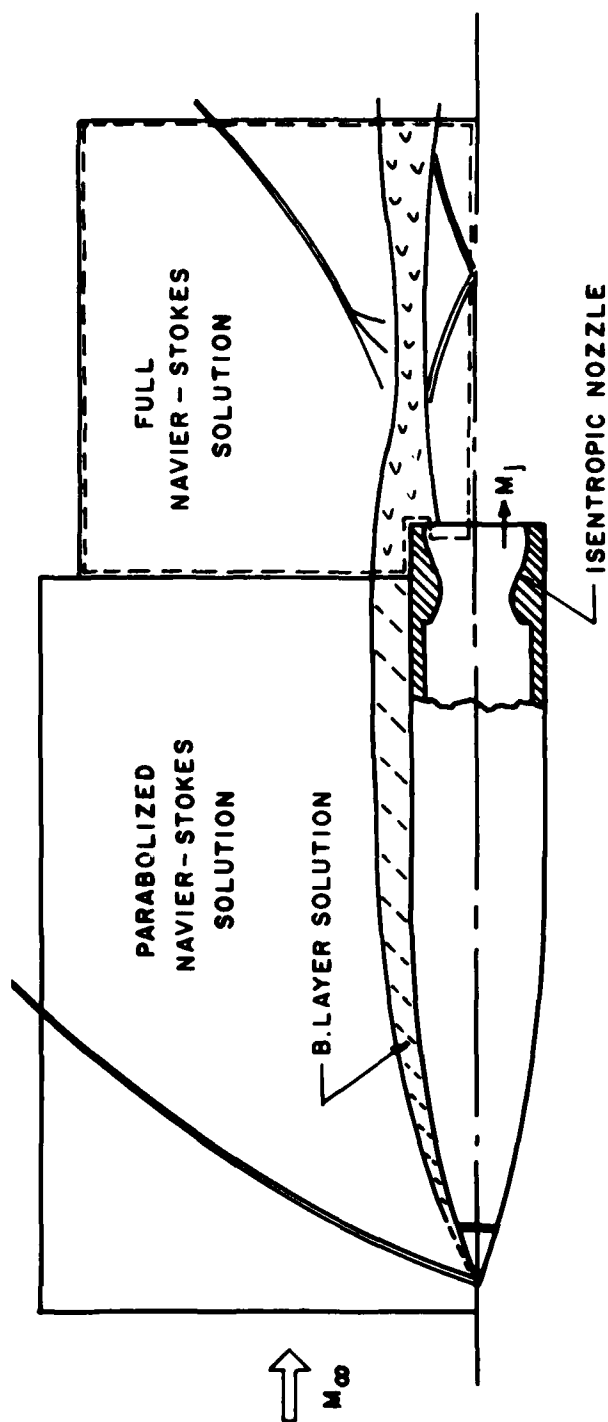


Figure 14. Flowfield Schematic for an Axisymmetric Nozzle in a Supersonic External Stream

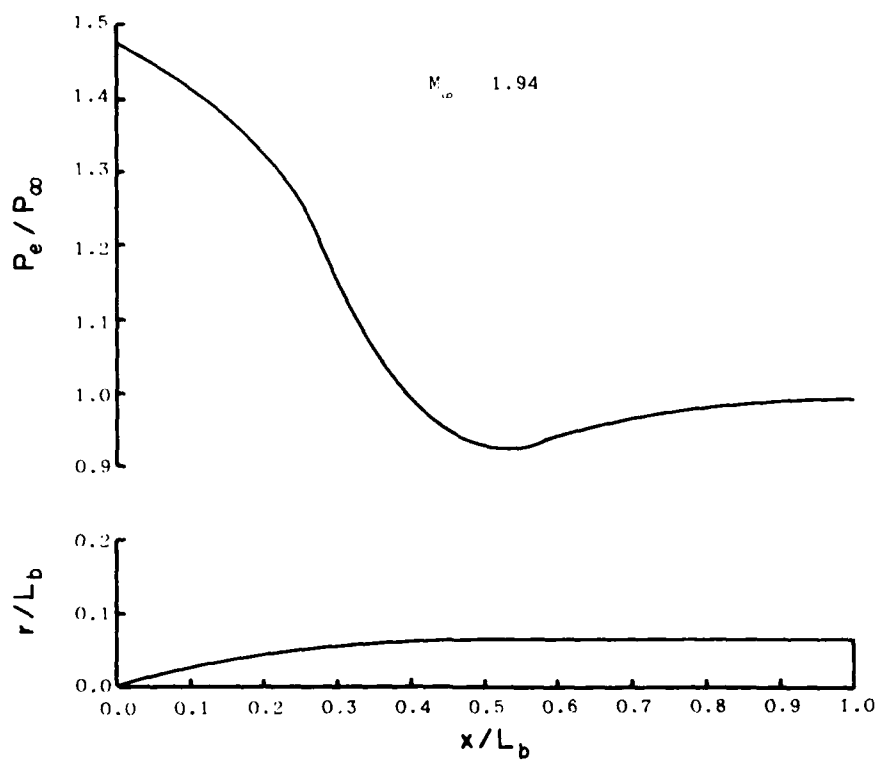


Figure 15. Computed Static Pressure Variation Along the Ogive Body Using a Parabolized Navier-Stokes Solver (Reference 23)

of the vertical velocity component is zero on the centerline boundary, a polynomial fit is used to set the vertical velocity profile from the edge of the boundary layer to the centerline.

## 2. THE UPPER BOUNDARY

The upper boundary, labeled DE on Figure 6, utilizes the simple wave procedure outlined by Roache (Reference 17, pp 282-283). This procedure assumes that properties are constant along a straight, left-running characteristic line passing through each point on the upper boundary. The position of this line running through a boundary point  $(i, JL)$  is determined by the angle  $(\mu_M + \theta)$ , where

$$\mu_M = \arcsin (1/M_{1,j}) \quad (84)$$

is the local Mach angle for supersonic flow, and

$$\theta = \arctan (v/u) \quad (85)$$

is the local flow direction. The properties on this characteristic line are determined by linear interpolation involving the properties at points  $(i-1, JL)$ ,  $(i-1, JL-1)$ , and  $(i, JL-1)$  as shown in Figure 16. Points  $(i-1, JL-1)$  and  $(i, JL-1)$  are points interior to the computational domain, and point  $(i-1, JL)$  is either a point on the inflow boundary ( $i = 1$ ) or a previously defined point on the upper boundary resulting from the left to right sweep along the boundary using this technique.

As shown in Figure 16, one of two possible interpolation schemes is applied depending on the local values of the quantities  $(\mu_M + \theta)$  and  $(\Delta r/\Delta x)$ . For the case of  $\tan (\mu_M + \theta)_{i-1, JL-1} > \Delta r/\Delta x$ , the position of the characteristic line lies between the points  $(i-1, JL-1)$  and  $(i, JL-1)$ . The properties at the point  $p$ , and thus at point  $(i, JL)$ , can then be determined by:

$$f_{i,JL} = f_p = f_{i-1,JL-1} + \left(\frac{\Delta x}{\Delta r}\right)(f_{i,JL-1} - f_{i-1,JL-1}) \quad (86)$$

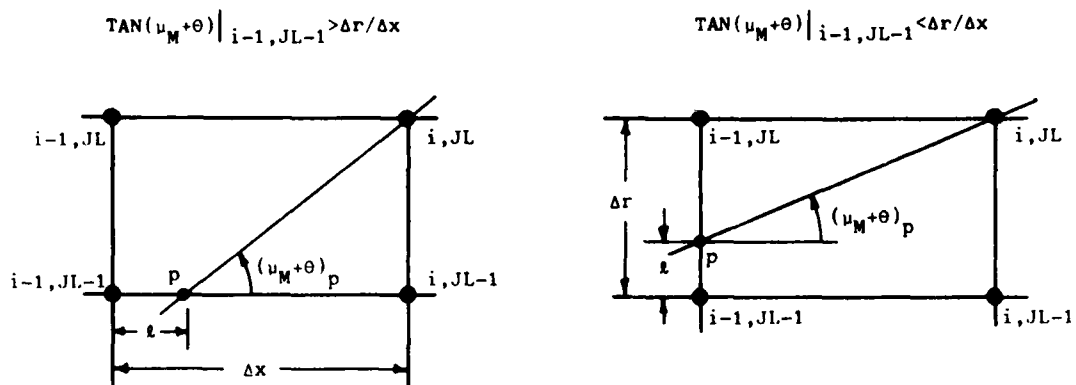


Figure 16. Upper Boundary Condition Schematic

The value of  $\ell$ , and thus the position of the point p, can be determined by the following procedure. If the quantity w is defined by:

$$w = \tan [90^\circ - (\mu_m + \theta)] \quad (87)$$

then by geometry:

$$w_p = (\Delta x - \ell) / \Delta r \quad (88)$$

If the interpolation procedure of Equation 86 is applied, then

$$w_p = w_{i-1, JL-1} + \left(\frac{\ell}{\Delta x}\right) (w_{i, JL-1} - w_{i-1, JL-1}) \quad (89)$$

Equating Equation 88 to Equation 89 and solving for  $\ell$  gives:

$$\ell = \frac{(\Delta x / \Delta r) - w_{i-1, JL-1}}{(w_{i, JL-1} - w_{i-1, JL-1}) / \Delta x + (1 / \Delta r)} \quad (90)$$

For the alternate case of  $\tan (\mu_m + \theta)_{i-1, JL-1} < (\Delta r / \Delta x)$ , the position of the characteristic line lies between the points (i-1, JL-1) and (i-1, JL). The properties at p are then determined by the equation:

$$f_{i, JL} = f_p = f_{i-1, JL-1} + (\ell / \Delta r) (f_{i-1, JL} - f_{i-1, JL-1}) \quad (91)$$

In this case, the quantity w is defined as

$$w = \tan (\mu_m + \theta) \quad (92)$$

and by geometry

$$w_p = (\Delta r - \ell) / \Delta x \quad (93)$$

The interpolation scheme for  $w_p$  now gives the expression:

$$w_p = w_{i-1, JL-1} + (\ell / \Delta r) (w_{i-1, JL} - w_{i-1, JL-1}) \quad (94)$$

Again, equating Equation 93 to Equation 94 and solving for  $l$  gives:

$$l = \frac{(\Delta r / \Delta x) - w_{i-1, JL-1}}{(w_{i-1, JL} - w_{i-1, JL-1}) / \Delta r + (1 / \Delta x)} \quad (95)$$

Applying the computed values of the interpolation length to the respective interpolation equation (either Equation 86 or Equation 91) gives the proper value of the desired flow variable at the boundary point ( $i, JL$ ).

### 3. THE DOWNSTREAM BOUNDARY

The downstream boundary (EF) is placed in a region where gradients in the flow variables are expected to exist. A quadratic extrapolation can be used on this boundary that lets  $\partial f / \partial x$  and  $\partial^2 f / \partial x^2$  be nonzero, thus satisfying this gradient condition. Assuming a constant grid spacing  $\Delta x$  near this boundary, Taylor series expansions can be performed in the following manner from a point ( $IL, j$ ) on the boundary to the following three points interior to the boundary:

$$f_{IL-1, j} = f_{IL, j} + \Delta x \left. \frac{\partial f}{\partial x} \right|_{IL, j} + \frac{\Delta x^2}{2} \left. \frac{\partial^2 f}{\partial x^2} \right|_{IL, j} + O(\Delta x^3 \left. \frac{\partial^3 f}{\partial x^3} \right|_{IL, j}) \quad (96)$$

$$f_{IL-2, j} = f_{IL, j} + 2\Delta x \left. \frac{\partial f}{\partial x} \right|_{IL, j} + 2\Delta x^2 \left. \frac{\partial^2 f}{\partial x^2} \right|_{IL, j} + O(\Delta x^3 \left. \frac{\partial^3 f}{\partial x^3} \right|_{IL, j}) \quad (97)$$

$$f_{IL-3, j} = f_{IL, j} + 3\Delta x \left. \frac{\partial f}{\partial x} \right|_{IL, j} + \frac{9\Delta x^2}{2} \left. \frac{\partial^2 f}{\partial x^2} \right|_{IL, j} + O(\Delta x^3 \left. \frac{\partial^3 f}{\partial x^3} \right|_{IL, j}) \quad (98)$$

If the assumption is made that the last term in each equation can be neglected, i.e.

$$\Delta x^3 \left. \frac{\partial^3 f}{\partial x^3} \right|_{IL, j} \approx 0 \quad (99)$$

then Equations 96 through 98 can be solved simultaneously to give the following expression for the boundary point  $(IL, j)$  in terms of the interior points:

$$f_{IL,j} = 3 f_{IL-1,j} - 3 f_{IL-2,j} + f_{IL-3,j} \quad (100)$$

This condition works well as long as large pressure gradients do not exist at this boundary, as in the case when a normal shock wave exits the boundary. If this does occur, the term involving  $\partial^3 f / \partial x^3$  is no longer negligible. Equation 100 then can become numerically unstable.

Numerical divergence did occur when the previous extrapolation condition was applied to regions of subsonic flow present at this out-flow boundary. Therefore, the following first order, zero gradient condition was applied at points  $(IL, j)$  when the Mach number at points  $(IL-1, j)$  was found to be subsonic:

$$f_{IL,j} = f_{IL-1,j} \quad (101)$$

#### 4. THE CENTERLINE

The centerline boundary (AF in Figure 6) is a line of symmetry with no mass or energy flux across it. The vertical velocity component condition (Equation 36) is applied by setting:

$$v_{1,1} = 0 \text{ for } 1 \leq i \leq IL \quad (102)$$

The symmetry conditions for the density and  $u$  component of velocity (Equations 37 and 38) which are valid only at the centerline are applied in the following manner. Taylor series expansions are performed for  $\rho$  and  $u$  from a centerline boundary point  $(i,1)$  to points  $(i,2)$  and  $(i,3)$  which are distances  $\Delta r$  and  $K\Delta r$ , respectively, above the centerline



boundary. The series expansions to these points give the following equations for density:

$$\rho_{1,2} = \rho_{1,1} + \Delta r \left. \frac{\partial \rho}{\partial r} \right|_{1,1} + \frac{\Delta r^2}{2} \left. \frac{\partial^2 \rho}{\partial r^2} \right|_{1,1} + O(\Delta r^3 \left. \frac{\partial^3 \rho}{\partial r^3} \right|_{1,1}) \quad (103a)$$

$$\rho_{1,3} = \rho_{1,1} + K \Delta r \left. \frac{\partial \rho}{\partial r} \right|_{1,1} + \frac{K^2 \Delta r^2}{2} \left. \frac{\partial^2 \rho}{\partial r^2} \right|_{1,1} + O(\Delta r^3 \left. \frac{\partial^3 \rho}{\partial r^3} \right|_{1,1}) \quad (103b)$$

If the centerline symmetry condition (Equation 37) is applied and the higher order term in each equation is neglected, these two equations can be solved simultaneously to obtain:

$$\rho_{1,1} = \frac{K^2 \rho_{1,2} - \rho_{1,3}}{(K^2 - 1)} \quad (103c)$$

A similar expression can be obtained for the u component of velocity:

$$u_{1,1} = \frac{K^2 u_{1,2} - u_{1,3}}{(K^2 - 1)} \quad (103d)$$

The previous extrapolation boundary conditions for the density and the horizontal velocity component were applied only to regions of supersonic flow at the centerline. Undesirable pressure wiggles occurred if these conditions were applied to regions of subsonic flow. The following first order zero gradient condition was applied at the centerline points (i,1) when the Mach number at points (i,2) was found to be subsonic

$$\rho_{1,1} = \rho_{1,2} \quad (103e)$$

$$u_{1,1} = u_{1,2} \quad (103f)$$

Since the v component of velocity is zero on the centerline, this boundary can be considered as a streamline. As discussed in Section II,

the stagnation enthalpy is then constant on this boundary. Since the total enthalpy at the inflow boundary is known, then

$$H_o|_{i,1} = H_o|_{1,1} \text{ for } 1 < i \leq IL \quad (104)$$

Since the value of  $u_{i,1}$  has been previously determined by Equation 103, the definition of the stagnation enthalpy can be expanded to determine the value of temperature at each boundary point  $(i,1)$ :

$$T_{i,1} = T_{1,1} + [(u_{1,1})^2 - (u_{i,1})^2]/2c_p \quad (105)$$

The values of the primitive variables  $\rho$ ,  $u$ ,  $v$ , and  $T$  have now been determined for each centerline boundary point, so that the required values of the conservative variables can be computed along this boundary.

#### 5. THE NOZZLE WALLS

The nozzle walls (BG, GH, and CH in Figure 6) are treated as no-slip, impermeable boundaries. The no-slip condition is imposed on the three wall faces by imposing the following conditions (see Figure 17):

Inner wall

$$u_{i,JWI} = v_{i,JWI} = 0 \text{ for } 1 < i \leq IW \quad (106a)$$

Outer wall

$$u_{i,JWO} = v_{i,JWO} = 0 \text{ for } 1 < i \leq IW \quad (106b)$$

Base (vertical) wall

$$u_{IW,j} = v_{IW,j} = 0 \text{ for } JWI < j < JWO \quad (106c)$$

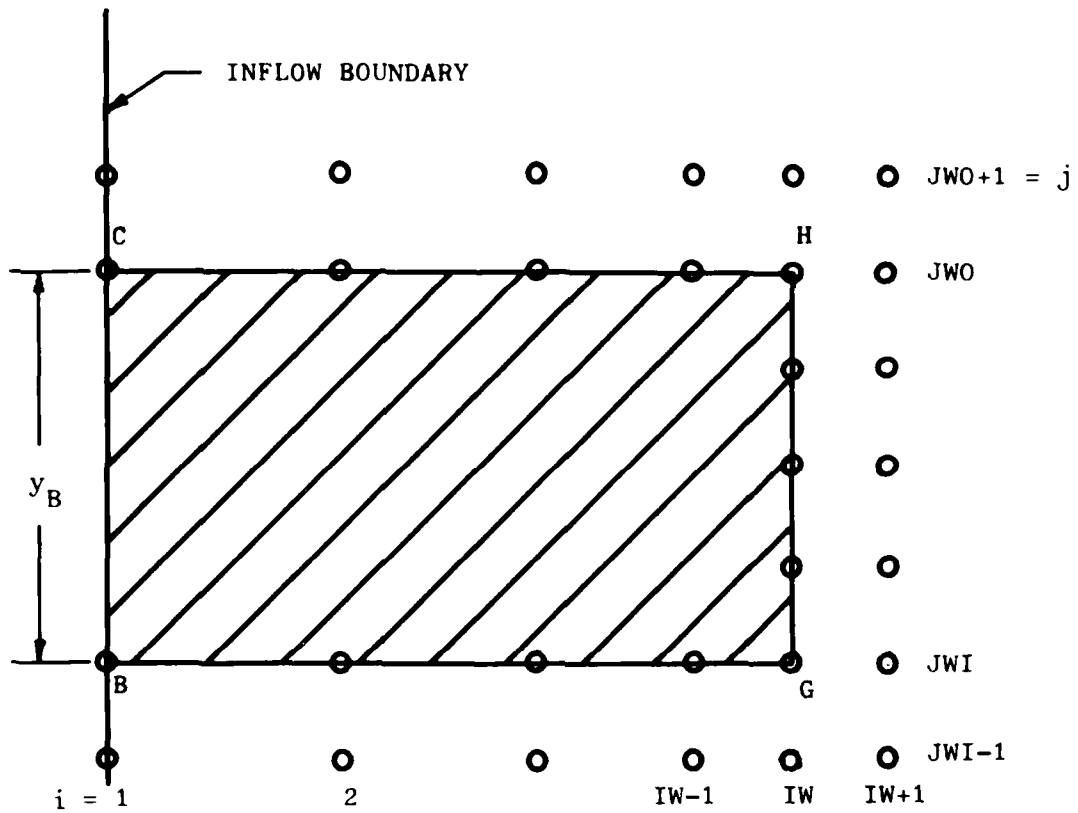


Figure 17. Finite Difference Mesh Near the Nozzle Walls

As discussed in Section II, a constant wall temperature is imposed on the nozzle walls. This condition is applied simply as:

$$T_{i,JWI} = T_{i,JWO} = T_W \text{ for } 1 < i \leq IW \quad (107a)$$

and

$$T_{IW,j} = T_W \text{ for } JWI < j < JWO \quad (107b)$$

A first order pressure gradient condition derived from Equation 48 is applied on each wall. This is imposed as:

$$P_{i,JWI} = P_{i,JWI-1} \text{ for } 1 < i < IW \quad (108a)$$

$$P_{i,JWO} = P_{i,JWO+1} \text{ for } 1 < i < IW \quad (108b)$$

$$P_{IW,j} = P_{IW+1,j} \text{ for } JWI < j < JWO \quad (108c)$$

Since the points (IW, JWI) and (IW, JWO) are positioned at sharp corner points, the simple pressure condition applied in Equation 108 is not applicable. An averaging scheme was therefore used to allow the pressure to adjust at the corners. This averaging is applied as:

$$P_{IW,JWI} = (P_{IW, JWI-1} + P_{IW+1, JWI})/2 \quad (109a)$$

and

$$P_{IW,JWO} = (P_{IW, JWO+1} + P_{IW+1, JWO})/2 \quad (109b)$$

The primitive variables  $u$ ,  $v$ ,  $P$ , and  $T$  have now been defined on the wall boundaries. The required values of the conservative variables can then be computed on this boundary.

## 6. INITIAL CONDITIONS

As discussed in Section II, initial values of the conservative variables must be imposed over the computational domain. Since the

incoming flow variables are fixed in time, they are initially imposed over the complete computational domain as follows:

$$u_{i,j}^o = u_{1,j}^o, \quad j \leq \text{JWI} \text{ and } \text{JWO} \leq j \quad (110)$$

The value of the  $u$  component of velocity in the wake region ( $\text{JWI} \leq j \leq \text{JWO}$ ) would be zero from the input profile. Therefore, the  $u$  component in the wake is set to grow exponentially using the following equation:

$$u_{i,j}^o = k_o (1 - e^{[(x_{\text{IW},j} - x_{i,j})/y_B]}) \quad (111)$$

where

$$k_o = u_{1,\text{JWI}-1}^o + (u_{1,\text{JWO}+1}^o - u_{1,\text{JWI}-1}^o) \frac{(r_{1,j} - r_{1,\text{JWI}-1})}{(r_{1,\text{JWO}+1} - r_{1,\text{JWI}-1})} \quad (112)$$

for  $\text{IW} < i \leq \text{IL}$  and  $\text{JWI} \leq j \leq \text{JWO}$ . Use of this scheme allows the velocity in the far wake to be close to that of the two streams, thus accelerating convergence.

Once an initial case for the nozzle flowfield had numerically converged to a valid solution, each succeeding case was initialized by imposing a new jet input profile on the inflow boundary of the preceding converged solution. This technique allowed the new solution to converge at a much greater rate, since the subsonic recirculation zone in the near wake was already in existence from the previous solution.

## SECTION V

### TURBULENCE MODELING

The experimental tests used as a basis for the computational solutions were conducted at a Reynolds number of  $2.2 \times 10^6$ , based on the ogive body length and the external flow conditions. The external flow in the region of the nozzle is thus expected to be of a fully turbulent nature. Reynolds numbers in the interior jet flow covered a range from  $1 \times 10^5$  to  $1.7 \times 10^6$ , based on nozzle exit conditions and the nozzle throat to exit plane length. Considering the effects of compressibility and the existence of a favorable pressure gradient in the divergent portion of the nozzle, a transition Reynolds number of  $5 \times 10^5$  was used to determine the condition at which the jet flow possessed turbulent characteristics (Reference 27).

The turbulent nature characteristic of these flows can be accounted for in the computational solution by a variety of eddy viscosity models ranging from locally dependent algebraic models to the more complex higher-order closure models such as the turbulent kinetic energy methods. Although the higher order methods can account for the time history of the turbulence in a flow, they require that accurate initial profiles of the turbulent shear stress be known or reliably calculated (Reference 28). If this initial profile condition cannot be satisfied, then this type of prediction method cannot be effectively utilized. Since this proved to be the case for the jet problem under consideration, locally dependent eddy viscosity models were carefully applied over the computational domain.

As shown in Figure 18, the computational domain contains three distinct regions in which various eddy viscosity models are applied. These regions consist of an area containing boundary layers, a far wake region downstream of the nozzle exit, and a near wake region close to the nozzle exit plane.

#### 1. BOUNDARY LAYER MODEL

In the first region, the dominating flow features are the boundary layers along the nozzle walls. Since the experimental boundary layer thicknesses are at least an order of magnitude smaller than the nozzle

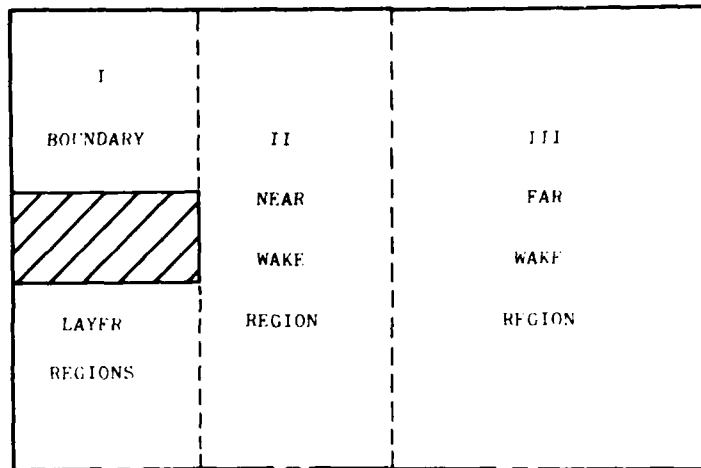


Figure 18. Eddy Viscosity Model Domains

radius, a two-dimensional turbulence model was judged to be sufficient for the axisymmetric cases. The eddy viscosity model applied in this region is a two layer Cebeci-Smith model (Reference 29). The inner layer of this model accounts primarily for the laminar sublayer adjacent to the wall, with the outer layer accounting for the remainder of the boundary layer region.

The expression for the inner model is based on Prandtl's mixing-length theory, which can be written as:

$$\epsilon_1 = \rho \, l_1^2 \left| \frac{\partial u_t}{\partial r_n} \right| \quad (113)$$

where  $u_t$  is the local tangential velocity parallel to the wall surface, and  $r_n$  is the normal distance measured from the wall. The mixing length in this model is adapted from Van Driest's sublayer model, and is expressed as:

$$l_1 = 0.4 \, r_n \left( 1 - e^{-\frac{r_n \sqrt{\rho \tau_w}}{26\mu}} \right) \quad (114)$$

This inner model assumes the flat plate pressure condition ( $dp/dx = 0$ ), but could be modified to account for a pressure gradient in the direction parallel to the wall within the sublayer.

The outer region eddy viscosity model consists of a Clauser-type displacement thickness model defined by the equation:

$$\epsilon_o = 0.0168 \rho u_e \delta^* \gamma_1 \quad (115)$$

where  $u_e$  is the appropriate tangential velocity at the boundary-layer edge and

$$\delta^* = \int_0^\delta \left(1 - \frac{u}{u_e}\right) dr_n \quad (116)$$

is the incompressible displacement thickness. This model also includes Klebanoff's intermittency factor  $\gamma_1$  defined by the following equation:

$$\gamma_1 = [1 + 5.5 \cdot (y/\delta)^6]^{-1} \quad (117)$$

The inner and outer regions of each boundary layer are defined by the requirement that the eddy viscosity remain continuous across the entire layer. This is accomplished by applying the inner model outward from the wall until  $\epsilon_i = \epsilon_o$  at a value  $r_c$ . The outer model is then applied from  $r_c$  outward across the remainder of the flowfield in the boundary layer region. Figure 19 shows a typical eddy viscosity profile across this region.

## 2. FAR WAKE MODEL

In the region downstream of the nozzle exit, the initial boundary layers on the nozzle walls merge to form a shear layer containing an imbedded wake region. This region in the flowfield can be further divided into two separate areas: the near wake region close to the nozzle exit that contains flow features such as the corner expansions, a "deadwater" zone, recompression shocks, and the far wake region further downstream where the flow eventually tends to a similar free shear layer type of flow. The eddy viscosity model for the far wake region will be discussed in this section, and then be extended for the near wake region in the next section.



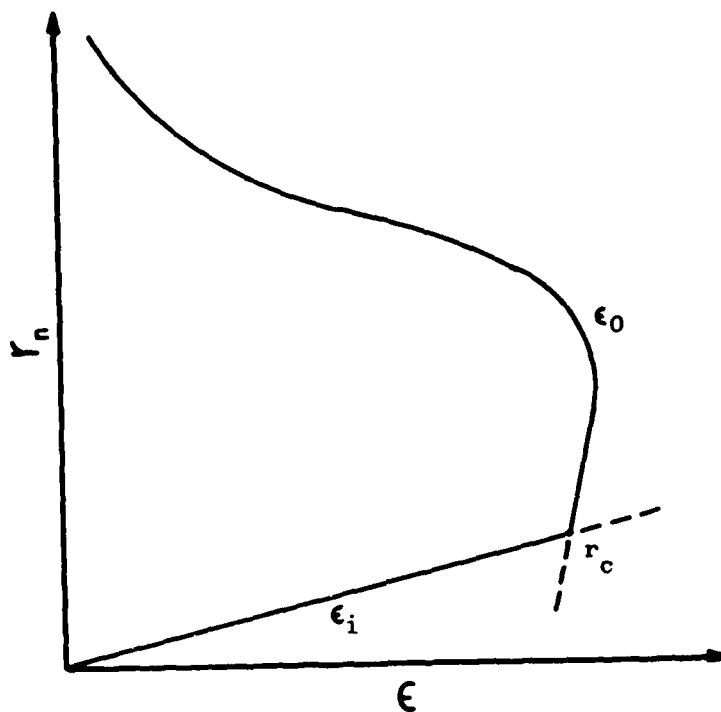


Figure 19. Eddy Viscosity Distribution Across a Boundary Layer

The eddy viscosity in the far wake region is in the form of the following Prandtl mixing length model:

$$\epsilon = \rho l^2 |\omega| \quad (118)$$

where  $\omega$  is defined as the vorticity:

$$|\omega| = \left| \frac{\delta u}{\delta r} - \frac{\delta v}{\delta x} \right| \quad (119)$$

and the mixing length  $l$  uses the same formulation as that of Dash, et al. (References 30 and 31) in their wake mixing length model for the core region of a coflowing nozzle:

$$l = 0.065 \delta_w \quad (120)$$

In this model,  $\delta_w$  is the representative thickness of the shear layer at any axial position in the wake. This model accounts for the variation

in eddy viscosity across the mixing layer through its dependence on the local value of vorticity. As in the eddy viscosity model utilized by Baldwin and Lomax (Reference 32), the vorticity profile across the mixing layer can be utilized to determine the thickness parameter  $\delta_w$ . This eliminates the somewhat complicated process of finding the outer edges of the shear layer based on velocity profiles for each axial position in the computational flowfield.

For the axisymmetric coflowing nozzle cases that were solved numerically, the maximum absolute value of vorticity in the wake was found to be in the following range:

$$1 \times 10^5 < |\omega_{\max}| < 1 \times 10^6 \text{ sec}^{-1} \quad (121)$$

The cutoff value used to define a representative edge of the mixing layer was:

$$|\omega_{\text{edge}}| = 1 \times 10^4 \text{ sec}^{-1} \quad (122)$$

This value gave a reasonable value of  $\delta_w$  as shown by a typical vorticity profile in Figure 20. The absolute value of vorticity typically dropped to less than one percent of  $|\omega_{\max}|$  within one gridpoint outside of the cutoff point.

A flat plate validation case was computed using the far wake model to check its accuracy in a known turbulent flowfield. The data of Toyoda and Hiriyama (Reference 33) for a flat plate in turbulent flow at a Mach number of 1.6 was used as the basis for a computational solution. The velocity defect in the wake obtained both experimentally and numerically is shown in Figure 21. As shown by this figure, the results generated by the numerical turbulence model compared very well with the thin flat plate data. Further details of this computation are listed in Appendix C.

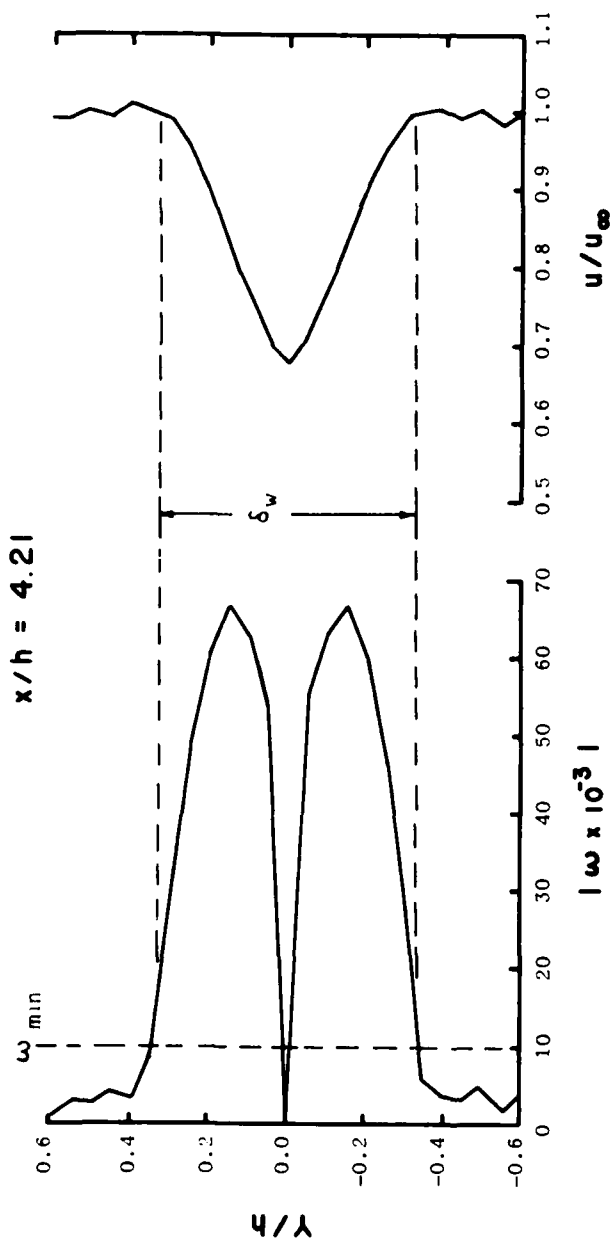


Figure 20. Typical Vorticity Profile Used to Compute Mixing Layer Thickness

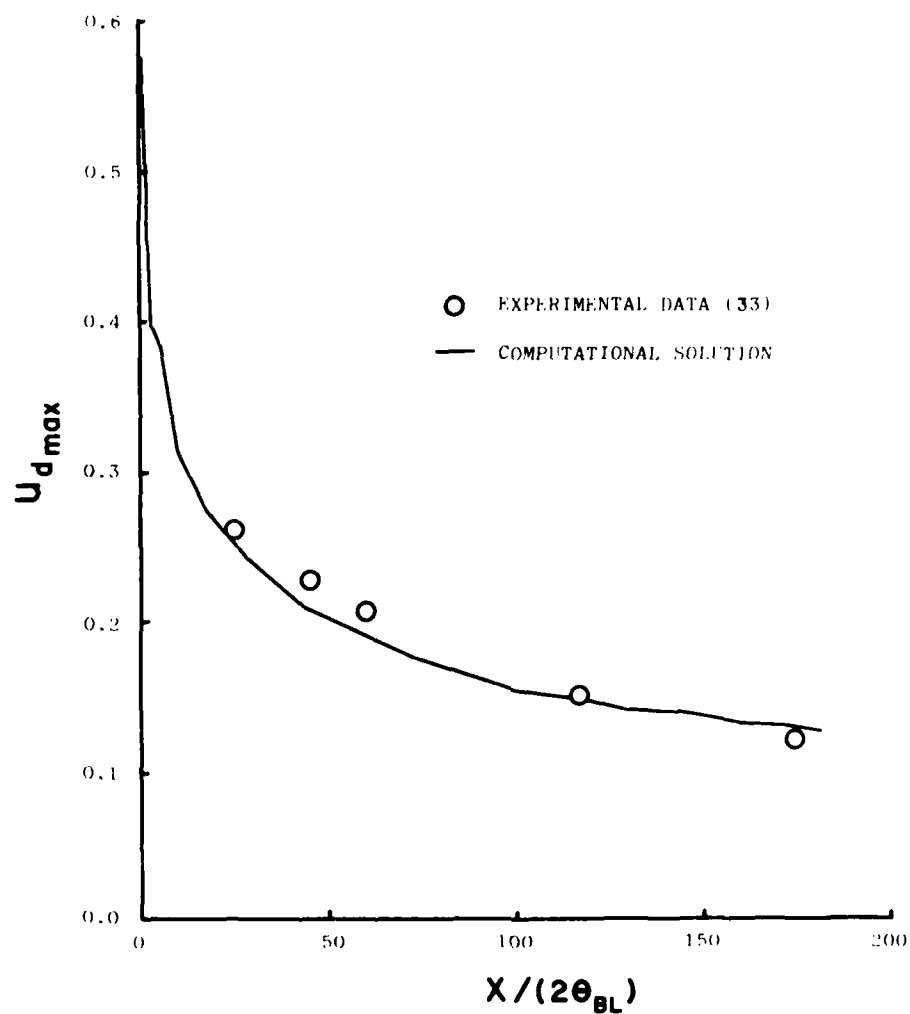


Figure 21. Maximum Velocity Defect vs Distance Behind the Trailing Edge of a Two-Dimensional Flat Plate,  $M_\infty = 1.60$

### 3. NEAR WAKE MODEL

The accuracy of a Prandtl type mixing length turbulence model is substantially dependent on the use of length scales that are truly representative of the flow in a given region. In the far wake region where a single mixing layer exists, the previous definition of the length scale involving  $\delta_w$  is valid. However, for the case of a nozzle with a thick base annulus, several length scales need to be defined in the near wake region. As shown in Figure 22, the existence of the subsonic, recirculating "dead water" region adjacent to the nozzle base wall complicates the flow simulation. In the near wake, the length scales must transition from the appropriate boundary layer thickness at the nozzle exit plane to the single mixing layer thickness ( $\delta_w$ ) that exists in the far wake region.

This transition is accomplished using the following procedure. The exterior edges of the mixing layers in the near wake are determined using the vorticity limits previously defined for the far wake. The interior edges of the dual shear layers are then defined by the Mach 0.5 contour line surrounding the "dead water" region as shown in Figure 22. The vorticity turbulence model defined by Equations 118 and 120 is then applied in the near wake region from the end of the boundary layer zone to the start of the initial mixing zone with

$$\delta = \delta_o \text{ in the free stream flow}$$

$$\delta = \delta_j \text{ in the jet stream flow}$$

$$\delta = 0.5 (\delta_o + \delta_j) \text{ inside the Mach 0.5 contour of the "dead water" region}$$

An initial mixing zone, one base height in length, is used to smoothly adjust the thickness of the dual shear layers ( $\delta_o$  and  $\delta_j$ ) that exist in the expansion and recompression zones of the near wake region to that of the single shear layer ( $\delta_w$ ) in existence further downstream. The following exponential equation is applied in this region:

$$\delta(x) = \delta_w|_{x_o} - (\delta_w|_{x_o} - \delta_o \text{ or } \delta_j|_{x_1}) e^{-k_1 x} \quad (123)$$

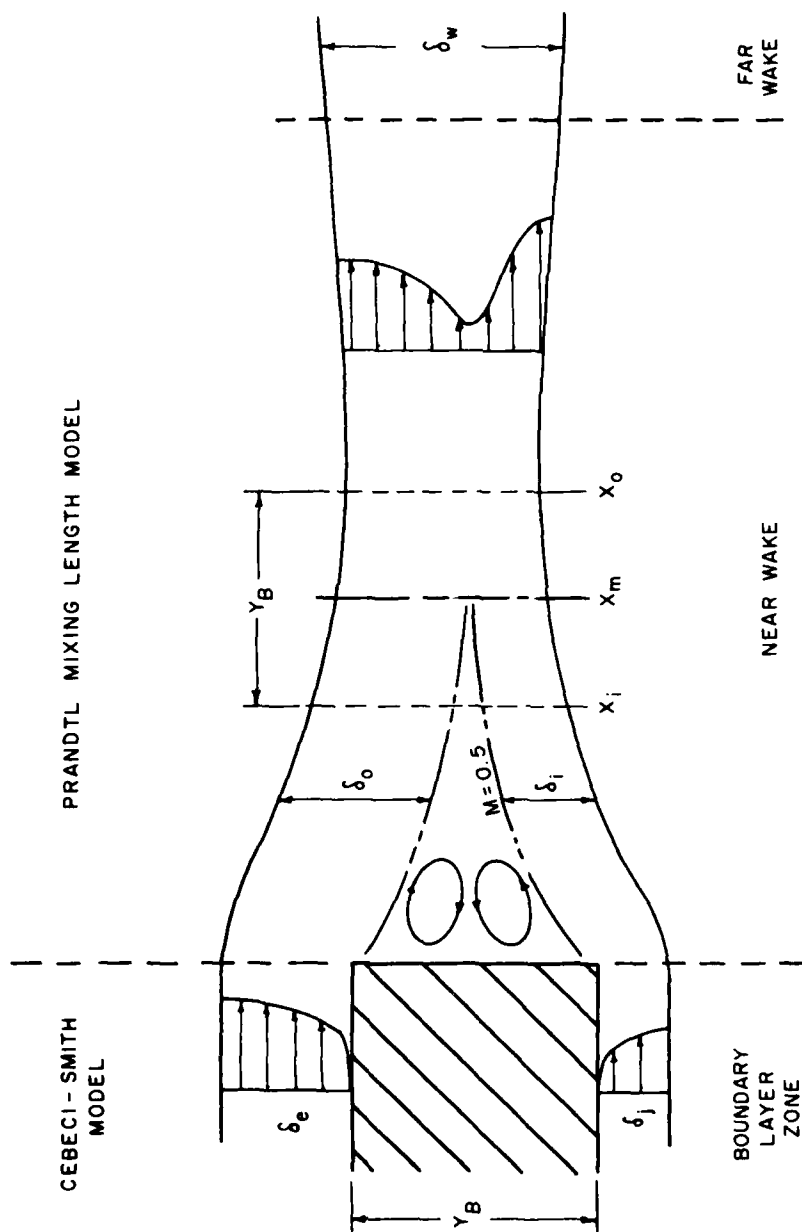


Figure 22. Viscous Layer Structure in the Near Wake

where  $k_1$  is determined by the expression

$$k_1 = 2 \left( \frac{x_m}{y_B} - \frac{x}{y_B} - 0.5 \right) \quad (124)$$

and the value of  $x$  lies in the following range:

$$x_m - 0.5y_B < x < x_m + 0.5y_B$$

The point  $x_m$  is centered in the mixing region. It was determined that the position of the midpoint  $x_m$  must be specified. If allowed to float, the near wake eddy viscosity region stretched to unrealistic lengths and gave erroneous values of nozzle base pressure. Using the very slightly underexpanded experimental case ( $P_j/P_\infty = 1.03$ ) as a basis, the midpoint  $x_m$  was varied to obtain its effect on nozzle base pressure. As shown in Figure 23, the value

$$x_m/y_B = 2.0$$

gave the best agreement with the experimental data. This value of  $x_m$  was then fixed for the entire series of flow calculations at the various pressure ratios. The variation in nozzle base pressure shown in Figure 23 illustrates the dependence of base pressure on the magnitude of the eddy viscosity applied in the near wake region.

A two-dimensional wedge-flat plate validation case was computed in order to obtain the accuracy of the turbulence model in the near wake and transition zone to the far wake. The data of Rom, Seginer, and Kronzon (References 34 and 35) for a one centimeter thick wedge-flat plate in turbulent flow at a Mach number of 2.25 was used as the basis for a computational solution.

All of the near wake features were accurately reproduced by the computational solution, and are discussed in Appendix D. Both the static pressure axially along the line of symmetry and the pitot pressure profiles in the near wake are in good agreement with the experimental data. The variation in the mixing length ( $\delta$ ) used in the turbulence model is shown in Figure 24. This figure exhibits the correct physical behavior

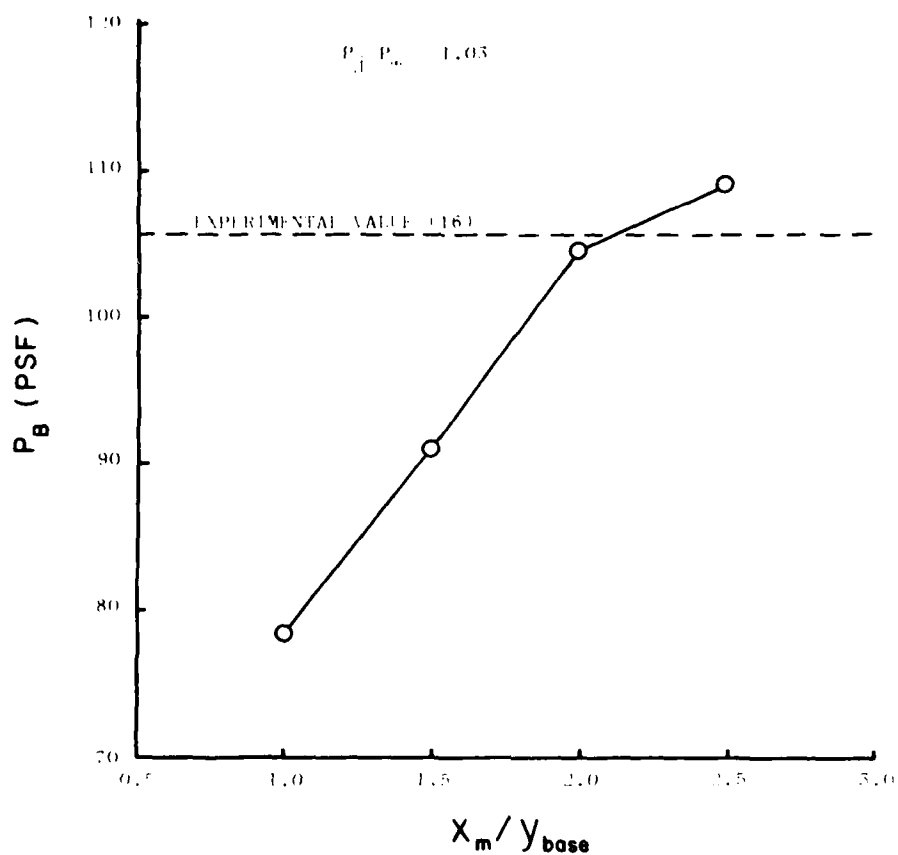


Figure 23. Computed Nozzle Base Pressure vs the Position of the Mixing Region Midpoint  $x_m$



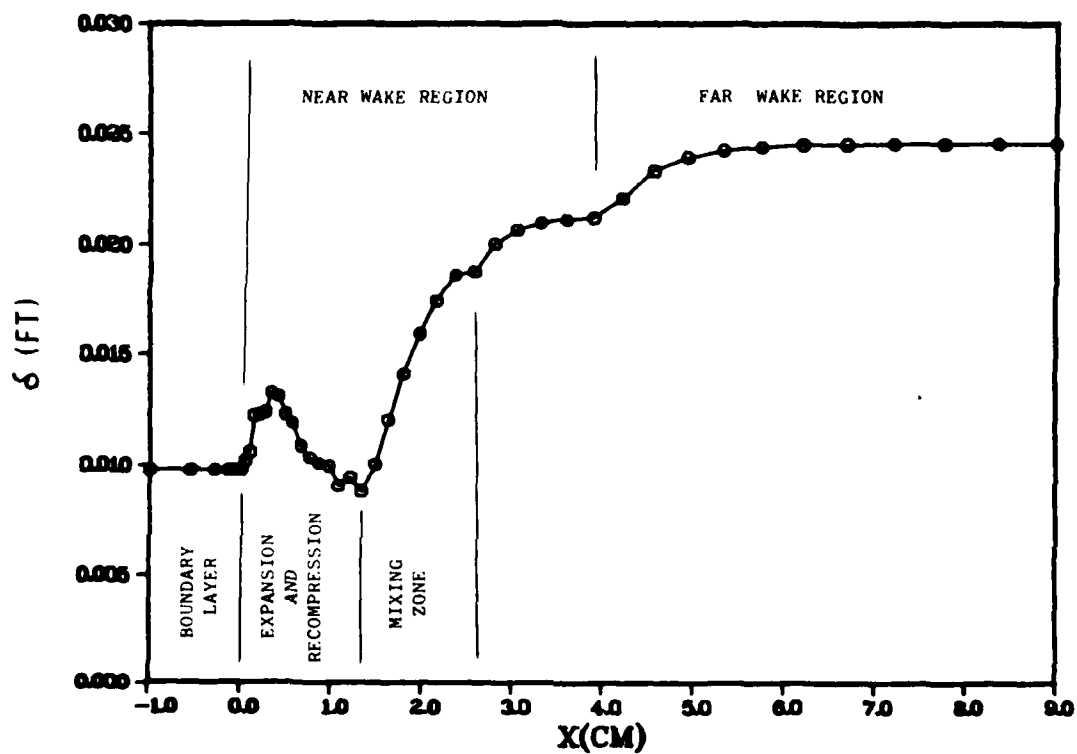


Figure 24. Computed Mixing Layer Thickness Used in the Wake Turbulence Model for the Wedge-Flat Plate Case

AFWAL-TR-81-3161

of the growth of  $\delta$  as the flow expands around the corner and the subsequent decrease in  $\delta$  as the flow recompresses in the near wake region. The exponential growth in the transition region is also evident. This case confirms that the eddy viscosity model used in the coflowing nozzle is a reasonable one that should account for the thrubulence effects in a correct manner.

## SECTION VI

## NUMERICAL RESULTS

This section will discuss the numerical results of the computational solutions using the algorithm, boundary conditions, and turbulence modeling detailed in previous chapters. The first portion of this section will discuss the experimental cases taken as the basis for comparison with the numerical solutions for the coflowing nozzle. The next portion discusses details involved in the actual computational procedure. The last part covers the comparison between the experimental and computational solutions, including some analyses of the accuracy of the simulations and discrepancies between the numerical solutions and the experimental data.

## 1. EXPERIMENTAL DATA BASE

As outlined in Section I, the data of Bromm and O'Donnell (Reference 16) is used as the experimental basis for this research effort. Supersonic fields of flow generated experimentally contain both highly viscous flow regions as well as shock structures ranging from weak regularly reflected shock waves to the strong Mach disc shock formation. Five different experimental nozzle pressure ratio conditions are used as the basis for the computational solutions. Nozzle base pressure measurements and schlieren photographs are the basis for experimental versus computational comparisons.

## a. Model

The model, a stainless steel body of revolution, consisted of a one-inch diameter cylindrical body with a 16.25 inch radius ogive nose (see Figure 15). The total length of the model was 7.5 inches. The model was supported by a 10% thick hollow side strut that acted as a conduit for the air flow to the jet as shown in Figure 5. The effects of this strut were found to be negligible on the flowfield downstream. This model was fitted with a nozzle which gave essentially isentropic flow with an exit Mach number of 3.00. The inner diameter of this nozzle at the exit plane was 0.742 inches, and the length from the nozzle throat to the exit plane was 1.20 inches. Four base pressure orifices were used to obtain the base pressure measurements as shown on Figure 5.

b. External Flow

The external flow conditions were generated in the NASA Langley 9-inch supersonic wind tunnel. The free stream Mach number was set at 1.94, and the free stream Reynolds number was fixed at  $2.2 \times 10^6$  based on the body length of the model. A turbulent boundary layer on the model at these conditions was insured through the use of a transition strip near the nose. The tests were conducted at a tunnel stagnation pressure of one atmosphere (assumed to be 2116 psf). Using these given conditions, the stagnation temperature of the free stream was calculated to be equal to 580.5°R.

c. Jet Flow

The flow just upstream of the jet exit plane was given to be at a Mach 3, zero divergence angle condition. The total pressure in the jet flow was varied to obtain the desired nozzle static pressure ratio. The jet static pressure at the nozzle exit plane was not measured directly, but was calculated using the given nozzle area ratio and the jet total pressure. A total temperature in the jet flow was not given experimentally, but was assumed to be equal to the freestream stagnation temperature (580.5°R).

2. COMPUTATIONAL DETAILS

Solutions were computed for the axisymmetric nozzle at the following five nozzle static pressure ratios:  $P_j/P_\infty = 0.150, 0.251, 0.527, 1.03$  and 1.59. These solutions were all performed on a CDC Cyber 175 digital computer located at Wright-Patterson AFB, Ohio. The average rate of data processing was 0.0015 second per grid point per iterative time increment. In this section further details of these computations will be discussed.

a. Grid Parameters

Important parameters of the computational grid including the number of grid points and axis length utilized in both the axial and radial directions are listed in Table 1 for each nozzle pressure ratio condition. The value of the axial field length includes a length increment of 0.4 upstream of the nozzle exit plane, with the exit plane at a value of  $x/r_{jet} = 0.0$ . A compact 45 x 45 point grid was used in the

TABLE 1

## COMPUTATIONAL GRID PARAMETERS

$P_j/P_\infty$	IL	JL	$x_{gr}/r_{jet}$	$r_{gr}/r_{jet}$
0.150	45	45	3.4	3.0
0.251	45	45	3.4	3.0
0.527	57	45	4.4	3.0
1.03	57	45	6.4	3.0
1.59	57	45	8.4	4.0

two most highly overexpanded cases ( $P_j/P_\infty = 0.150, 0.251$ ). Twelve additional grid points were then added in the axial direction downstream of the original grid to form a 57 x 45 grid for the next case where  $P_j/P_\infty = 0.527$  (Figure 25). This methodology gave a consistent cell length in the axial direction for each of these three cases in which both a regular shock reflection ( $P_j/P_\infty = 0.527$ ) and Mach discs ( $P_j/P_\infty = 0.251, 0.150$ ) should occur. The computational domain was then stretched using the 57 x 45 point grid to the degree necessary to cover the phenomena of interest for the two underexpanded cases.

Minimum grid spacing in both the axial and radial directions occurred adjacent to the nozzle walls, and was set at:

$$\Delta x/r_{jet} = \Delta r/r_{jet} = 0.030$$

The patched exponential stretching outlined in Section III was then applied to form each grid initially for the various cases. The adaptive grid procedure was applied in the radial direction during the solution procedure as discussed in Section III and Appendix B to obtain the final grid geometry for each case.

#### b. Coarse Grid Effects on Boundary Layer Resolution

The numerical solution of the Navier-Stokes equations can involve significant truncation errors in regions containing high velocity gradients such as within turbulent boundary layers when relatively coarse computational grids are employed. Errors in computed velocity gradients

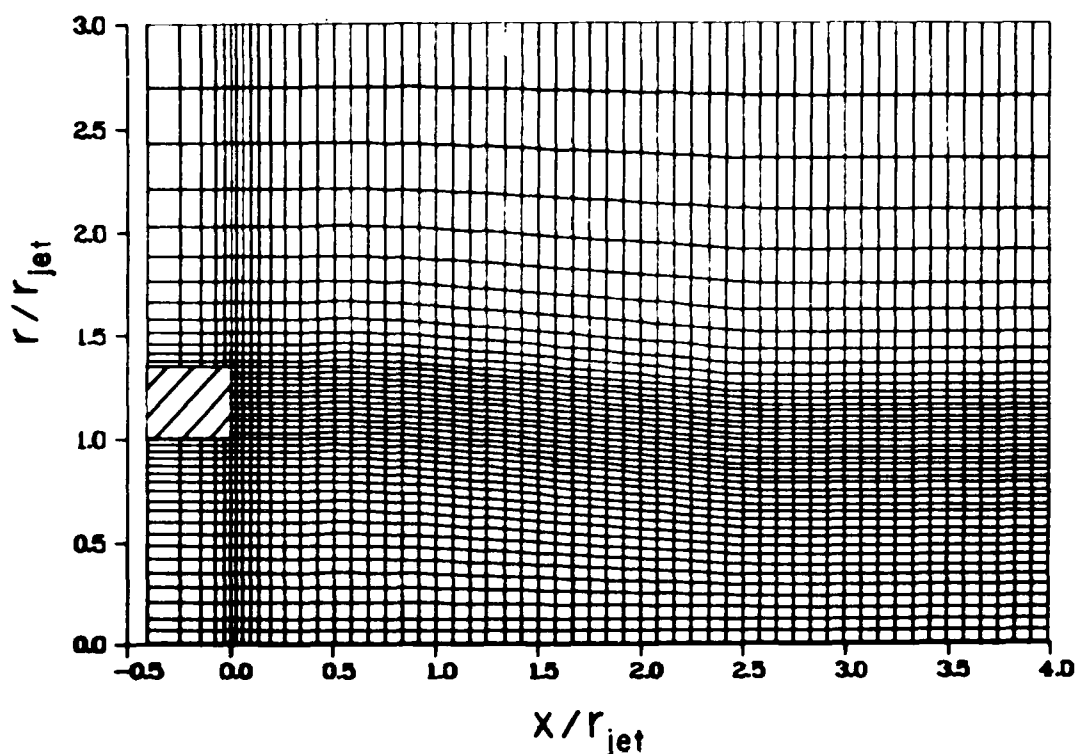


Figure 25. Adaptive Finite Difference Mesh,  $P_j/P_\infty = 0.527$

involved in shear force terms at the wall can result in erroneous values of the pressure gradient along the wall. The extent of these errors can be realized by assuming the existence of a turbulent boundary layer possessing a velocity profile in the following form (Reference 36):

$$u^+ = y^+ \quad 0 < y^+ \leq 11 \quad (125a)$$

$$u^+ = 2.50 \ln(y^+) + 5.10 \quad 11 < y^+ < y_{BL \text{ edge}}^+ \quad (125b)$$

where

$$u^+ = u\sqrt{\rho/\tau_w} \quad \text{and} \quad y^+ = \frac{y}{\nu} \sqrt{\tau_w/\rho}$$

Since the dominant term in the shear stress is the gradient  $\frac{\partial u}{\partial y}$ , a comparison of the value obtained using this profile can be made with that obtained using the numerical algorithm. MacCormack's algorithm

computes this gradient using a first order finite difference in the direction of the sweep for the predictor step. At the wall this gradient is computed as:

$$\left. \frac{\Delta u}{\Delta y} \right|_w = u_{1,jw+1} / \Delta y_w \quad (126)$$

where  $jw+1$  is the first grid point above the wall, and  $\Delta y_w$  is the grid spacing adjacent to the wall. If a nominal Reynolds number of  $1 \times 10^6$  based on body length is applied to the previous turbulent velocity profile, the ratio of actual wall velocity gradient given by the previous profile to that computed using Equation 126 can be displayed as a function of the ratio of  $u$  velocity component at the first point above the wall to the freestream velocity as shown in Figure 26. For grid spacing substantially greater than the sublayer ( $u_1/u_e = 0.475$ ), excessive error in the computed velocity gradient occurs. Since in the nozzle solutions the previously stated minimum grid spacing gives values of  $(u_1/u_e)|_\infty = 0.72$  and  $(u_1/u_e)|_{jet} = 0.90$ , a correction is needed. This is accomplished by applying the value of  $C_f$  given by a boundary layer analysis at the inflow boundary along the nozzle wall when  $j = jw$ , instead of using the standard differencing procedure in the algorithm. This procedure has resulted in smooth pressure profiles near the inflow boundary instead of slight pressure jumps previously observed in coarse mesh cases. This concept is analogous to the wall functions described by Launder and Spaulding (Reference 37) and employed by Peery and Forester (Reference 38).

#### c. External Flow Parameters

Values for the external flow variables were input numerically by applying the experimental values of  $M_\infty$ ,  $P_{0\infty}$ ,  $T_{0\infty}$ , and the boundary layer profiles generated for use on the inflow boundary. A value for the turbulent skin friction coefficient of  $C_f = 0.00286$  was obtained from the boundary layer input profiles and was applied on the external nozzle wall as discussed in the last section. A wall temperature of  $551^\circ R$  was calculated using the analysis in Appendix A. The wall temperature was given a constant value for all five cases since the analysis showed that this temperature should not vary more than one degree over the range of simulated flow conditions.

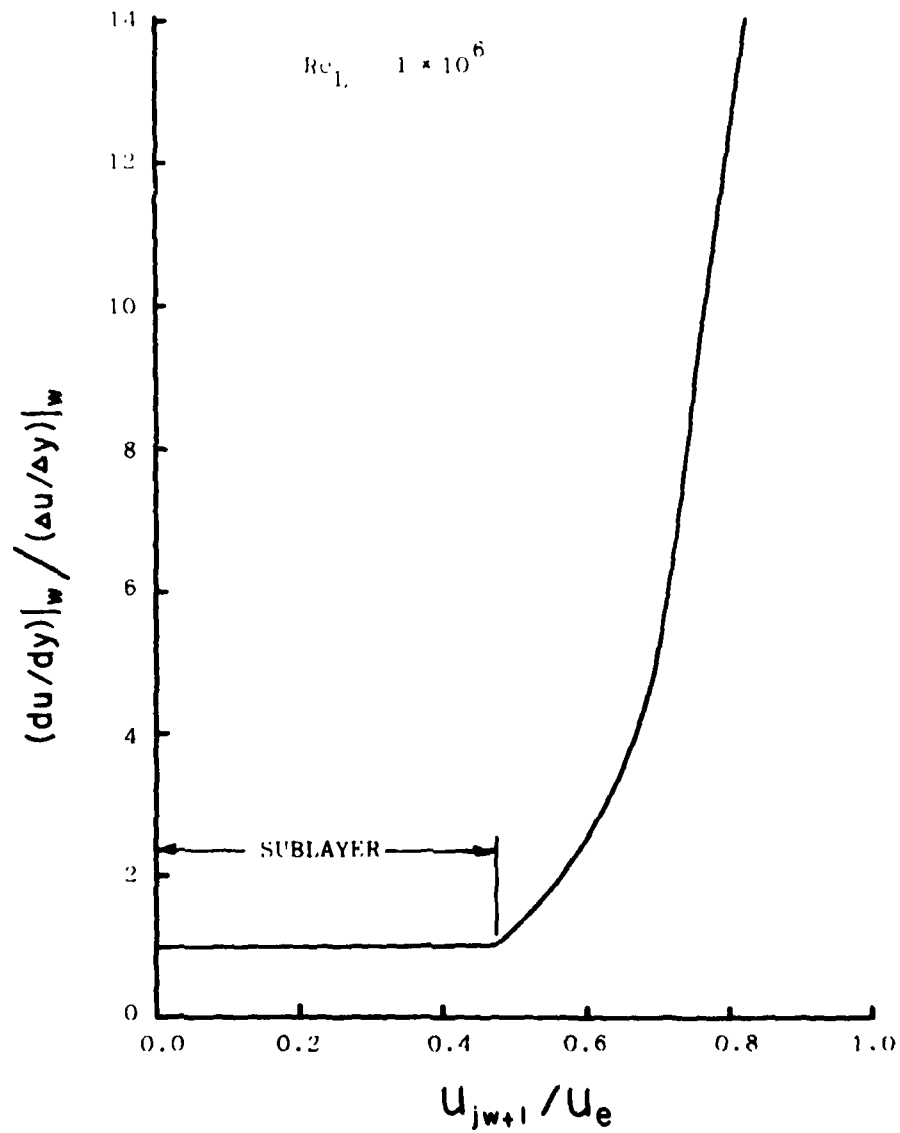


Figure 26. Error in Computed Velocity Gradient vs Grid Coarseness for a Turbulent Boundary Layer



## d. Jet Flow Parameters

The numerical jet field of flow was determined by applying the experimental values of the jet Mach number and total temperature given in the previous section along with the values of the jet total pressure and skin friction coefficient listed in Table 2. Since the nozzle wall temperature was considered to be constant, the value for the internal nozzle wall was also set at 551°R. As shown in the table, the state of the jet boundary layer in all of the cases except the lowest nozzle pressure ratio condition ( $P_j/P_\infty = 0.150$ ) was considered to be turbulent at the nozzle exit plane. Since the case where  $P_j/P_\infty = 0.251$  possessed a Reynolds number below the previously set transition point, a solution using a laminar jet boundary layer was also obtained. At this pressure condition, both the laminar and turbulent jet boundary layers gave nearly identical values for the nozzle base pressure and normal shock position. However, the laminar case exhibited a mild shear layer oscillation for the duration of the solution procedure. For this reason the results of the turbulent case are presented. It is interesting to note that no mixing layer oscillations were observed in the other laminar jet condition ( $P_j/P_\infty = 0.150$ ).

TABLE 2  
COMPUTATIONAL JET FLOW PARAMETERS

$P_j/P_\infty$	$P_{o_{jet}}$ (psf)	$Re_j \times 10^{-5}$	Bound. Layer Character	$C_{f_j} \times 10^3$
0.150	1636.	1.61	Laminar	1.60
0.251	2738.	2.70	Turbulent	3.39
0.527	5747.	5.67	Turbulent	2.86
1.030	11230.	11.08	Turbulent	2.50
1.590	17340.	17.11	Turbulent	2.30

## e. Boundary Condition Application

The specific numerical boundary conditions given in Section IV were applied to the computational domain in order to achieve solutions for the axisymmetric nozzle. No significant problems were encountered

with the application of the upstream boundaries, the upper boundary, or the nozzle wall boundaries. Difficulties were encountered with both the downstream boundary and the centerline boundary when a significant portion of the flow along each boundary was subsonic in nature. This condition only occurred for the highly overexpanded case ( $P_j/P_\infty = 0.150$ ), where a substantial embedded subsonic region exists downstream of the Mach disc shock structure.

The quadratic extrapolation given by Equation 100 produced very reasonable results for those cases where the outflow was either entirely supersonic, or only subsonic at a very few points in the nozzle wake. For the case where a substantial area of subsonic flow existed behind a Mach disc structure and extended to the downstream boundary, numerical divergence occurred when Equation 100 was applied. A second order zero gradient condition was then applied in regions of subsonic flow along this boundary. Application of this condition did not produce numerical divergence, but did give unrealistic pressure jumps at this boundary. A first order zero gradient condition given in Equation 101 was then successfully applied to subsonic regions on this boundary with reasonable results.

An almost identical situation occurred along the centerline boundary for subsonic regions containing fairly strong radial flow gradients close to the centerline. Both the extrapolation condition given by Equations 103c, d and a second order zero gradient condition produced unrealistic radial oscillations in the numerical solution (called wiggles) within these regions of subsonic flow. The application of a first order zero gradient condition given by Equations 103e, f helped reduce these oscillations to achieve a reasonable solution.

Two solutions were also computed where first the downstream boundary, and subsequently, the upper boundary were repositioned greater distances from the nozzle as discussed in Appendix E. No changes were detected in either the shock structure or the nozzle base pressure coefficient. These test cases validate the effectiveness of these boundary conditions at the positions utilized in the actual nozzle solutions.

## f. Convergence

As stated in Section III, the numerical solutions were either initially started using only the boundary layer profiles across the computational domain, or restarted from a previous solution by applying new input profiles at the jet inflow boundary. Solution times based upon the convergence criteria discussed in Section III varied significantly for the two methods of initial startup. Solution times on the Cyber 175 using only the boundary layer profiles to form the initial conditions were approximately 3.0 hours for the 45 x 45 point mesh and 3.8 hours for the 57 x 45 point mesh. Solution times for cases restarted from previous solutions were approximately 1.7 hours for the 45 x 45 mesh and 2.1 hours for the 57 x 45 mesh. The large difference in these solution times is mainly attributed to the length of time required for the subsonic recirculation region in the near wake to form and achieve a steady state condition.

## 3. COMPARISON WITH EXPERIMENTAL DATA

Comparisons between the numerical solutions and the experimental data can be made both qualitatively and quantitatively. Figures 27 through 31 give a good visual comparison between the numerical solutions depicted as Mach number contours and the experimental schlieren photographs. In these figures the computed solutions above the centerline were reflected to give a total nozzle flowfield to compare with the schlieren photographs. All features typical of afterbody types of flows such as the shock structure internal to the jet core flow, external recompression shocks, and shear layer development are readily discernible and in very good agreement with the experimental data.

As shown by the previous figures, the pressure condition at which the jet flow shock structure transitions from a regular reflection on the centerline to the Mach disc formation lies between the two cases where  $P_j/P_\infty = 0.527$  and  $P_j/P_\infty = 0.251$ . Although the shock structure near the centerline appears similar in the computational solutions for these two cases, an enlargement of this region as shown in Figure 32 reveals several differences. The shock strength (related to the Mach number jump across the shock) is much greater in both of the strong Mach

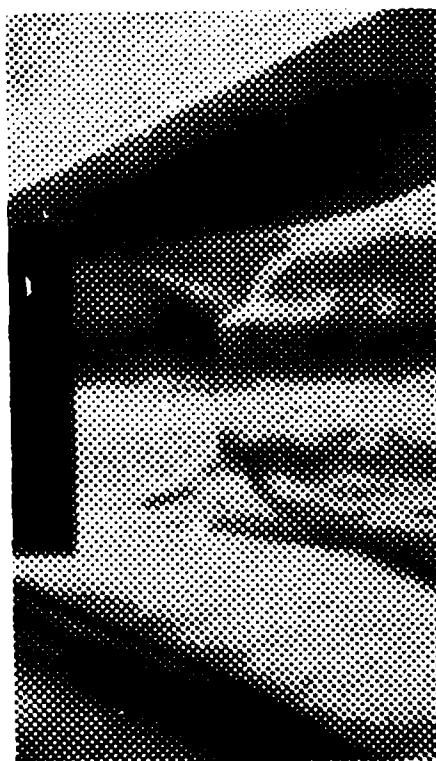
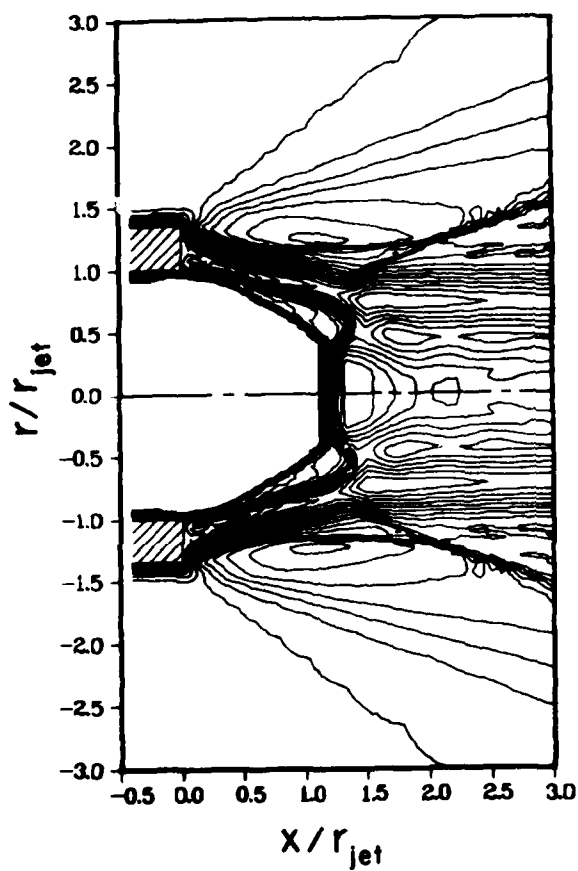


Figure 27. Axisymmetric Nozzle Solution,  $P_j/P_\infty = 0.150$

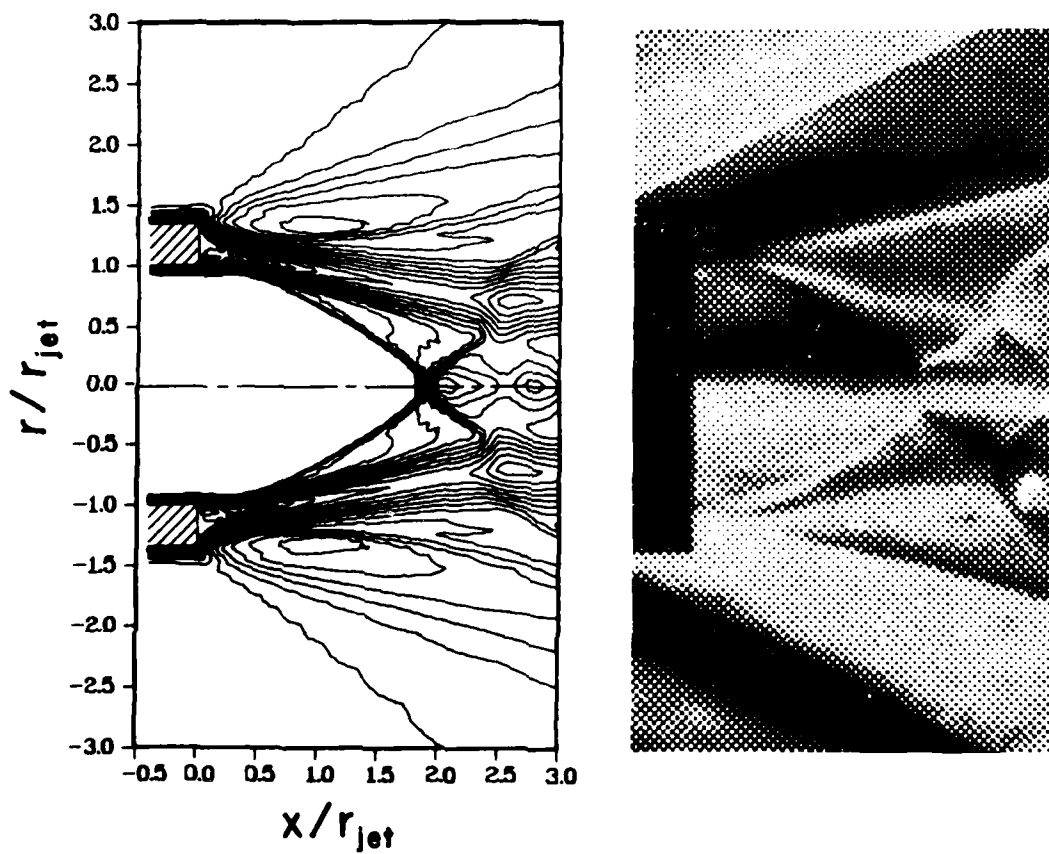


Figure 28. Axisymmetric Nozzle Solution,  $P_j/P_\infty = 0.251$

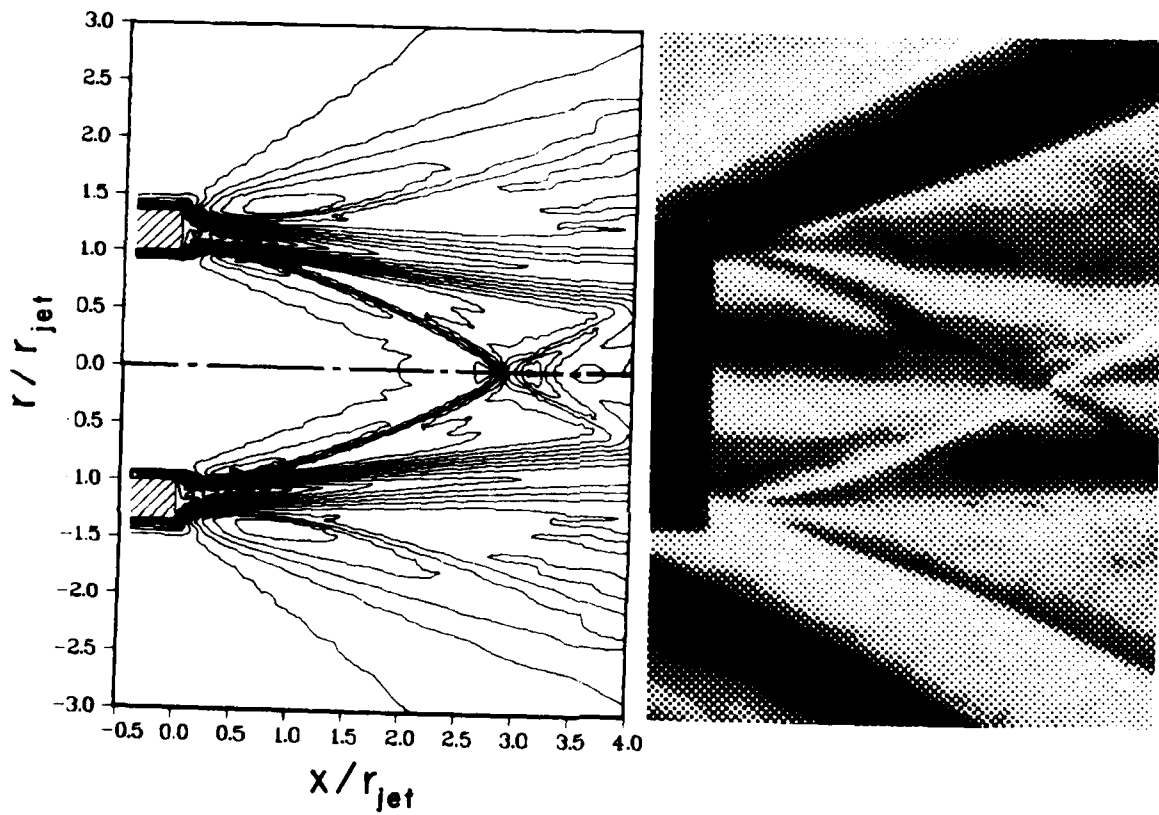


Figure 29. Axisymmetric Nozzle Solution,  $P_j/P_\infty = 0.527$

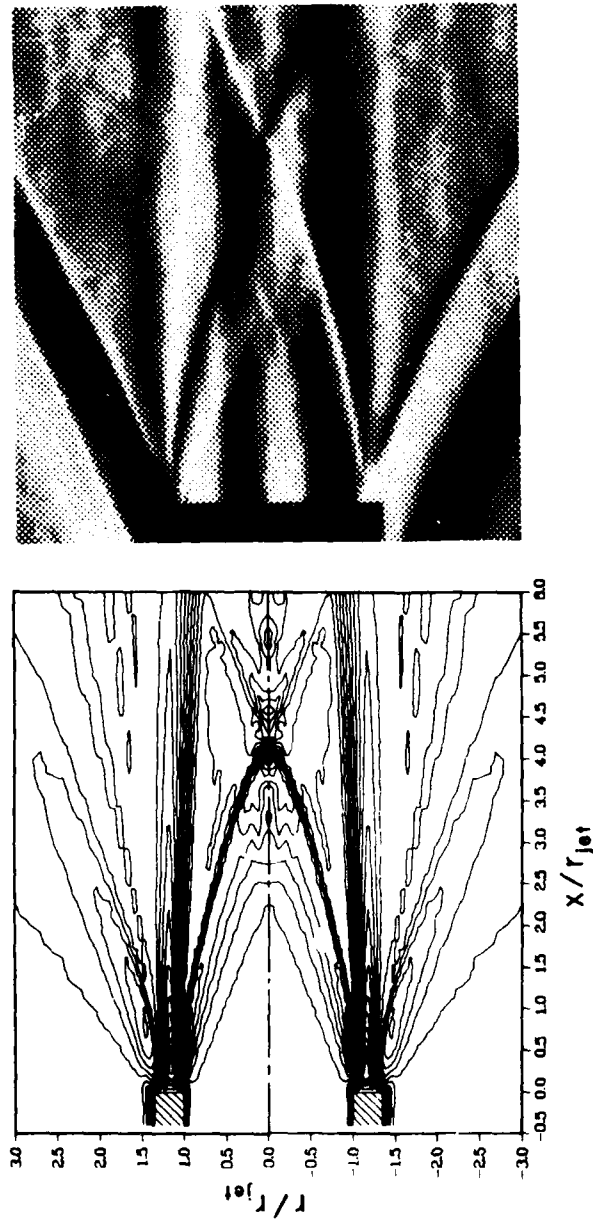


Figure 30. Axisymmetric Nozzle Solution,  $P_j/P_\infty = 1.03$

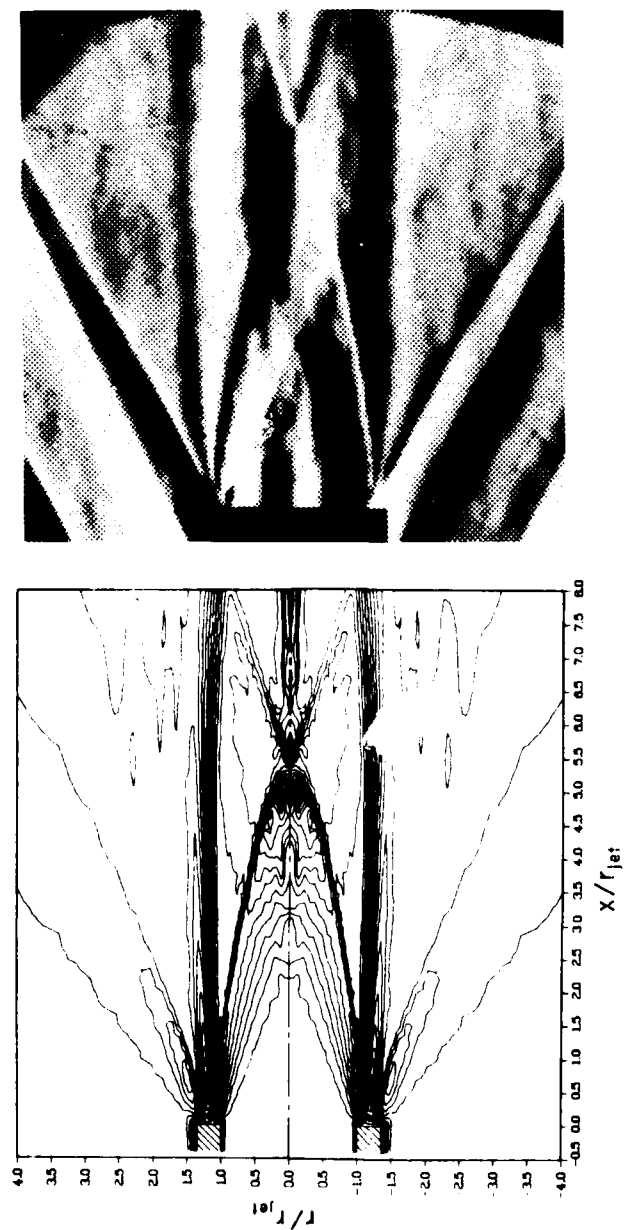


Figure 31. Axisymmetric Nozzle Solution,  $P_j/P_\infty = 1.59$



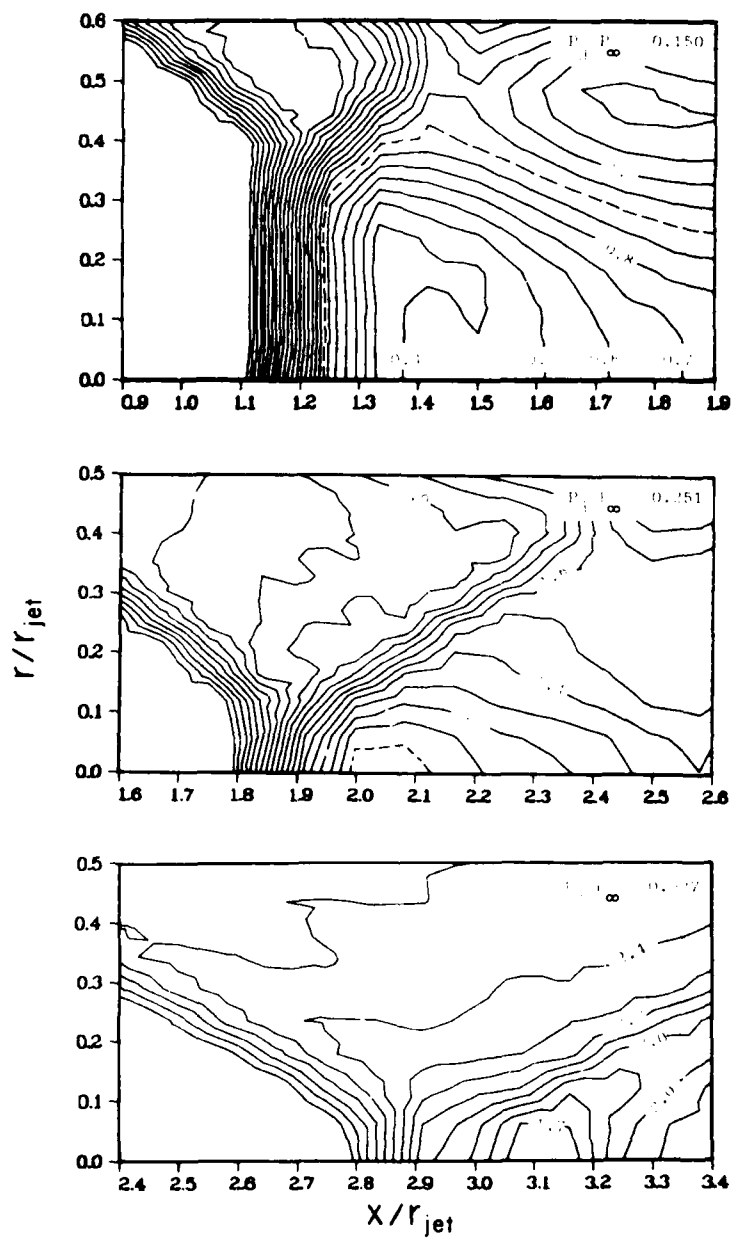


Figure 32. Computed Mach Number Contours in the Region Near the Shock Reflection at the Centerline

AD-A119 074

AIR FORCE WRIGHT AERONAUTICAL LABS WRIGHT-PATTERSON AFB OH F/G 20/4  
NAVIER-STOKES SOLUTIONS FOR AN AXISYMMETRIC NOZZLE IN A SUPERSO--ETC(U)  
MAR 82 G A HASEN  
AFWAL-TR-81-3161

UNCLASSIFIED

NL

2 of 2  
FOIA  
1997

END  
DATE  
FILMED  
10-82  
DTIC

disc cases ( $P_j/P_\infty = 0.150$  and  $0.251$ ) then in the regularly reflected case ( $P_j/P_\infty = 0.527$ ). The sonic lines in this region are displayed as dashed lines in Figure 32 in order to easily identify regions of subsonic flow. Both Mach disc cases contain areas of subsonic flow downstream of the shock along the centerline, whereas the minimum Mach number behind the regularly reflected shock is approximately equal to 1.65.

A check was made on the solution to the highly overexpanded case ( $P_j/P_\infty = 0.150$ ) to determine if the numerical solution correctly simulated the flow conditions across the strong normal shock in the region near the centerline. Since the  $v$  velocity components are very small near the centerline, a one-dimensional analysis based on the Rankine-Hugoniot relations across normal shocks can be applied. As shown in Table 3, the computational solution was within 2% of the exact one-dimensional analysis.

TABLE 3  
COMPARISON BETWEEN A 1-D ANALYSIS AND THE COMPUTATIONAL  
SOLUTION ACROSS THE MACH DISC FOR  $P_j/P_\infty = 0.150$

	$M_1$	$M_2$	$P_2/P_1$	$\rho_2/\rho_1$	$T_2/T_1$
Exact (1-D)	3.00	.475	10.33	3.857	2.679
Computational	3.00	.442	10.52	3.906	2.695
% Error	----	1.1	1.8	1.3	0.6

Several other phenomena associated with afterbody flows are evident in Figure 33, which displays computed velocity profiles at given axial stations for the large Mach disc case. The separated "deadwater zone" of recirculating flow is readily apparent in the near wake region, as is the development of the near wake to a far wake velocity profile. The existence of the strong Mach disc near the centerline is very evident, and the flow in the subsonic core region behind the shock accelerates in the correct manner to a slightly supersonic condition at the outflow boundary.

A closer look at the near wake region is shown in Figure 34 for two of the computational cases. This figure illustrates the change in the shape of the "deadwater region" from a predominantly symmetric nature

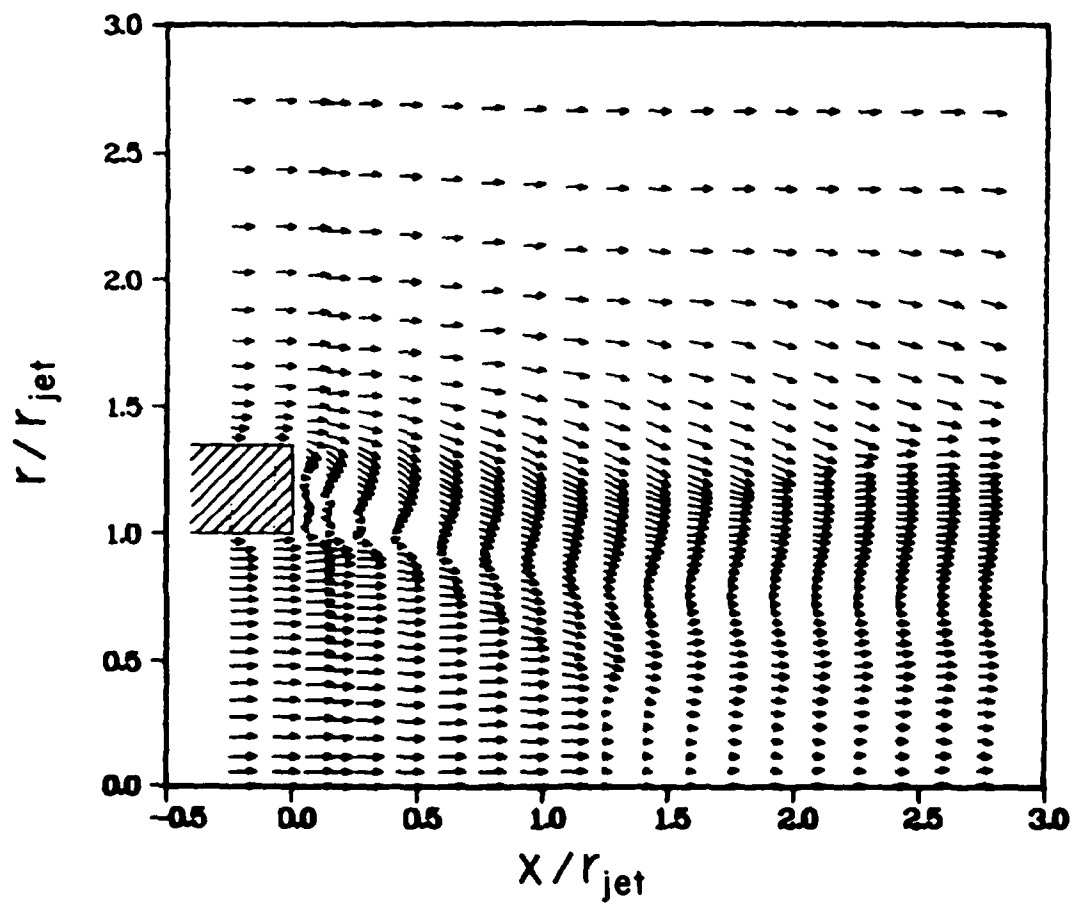


Figure 33. Computed Velocity Profiles,  $P_j/P_\infty = 0.150$

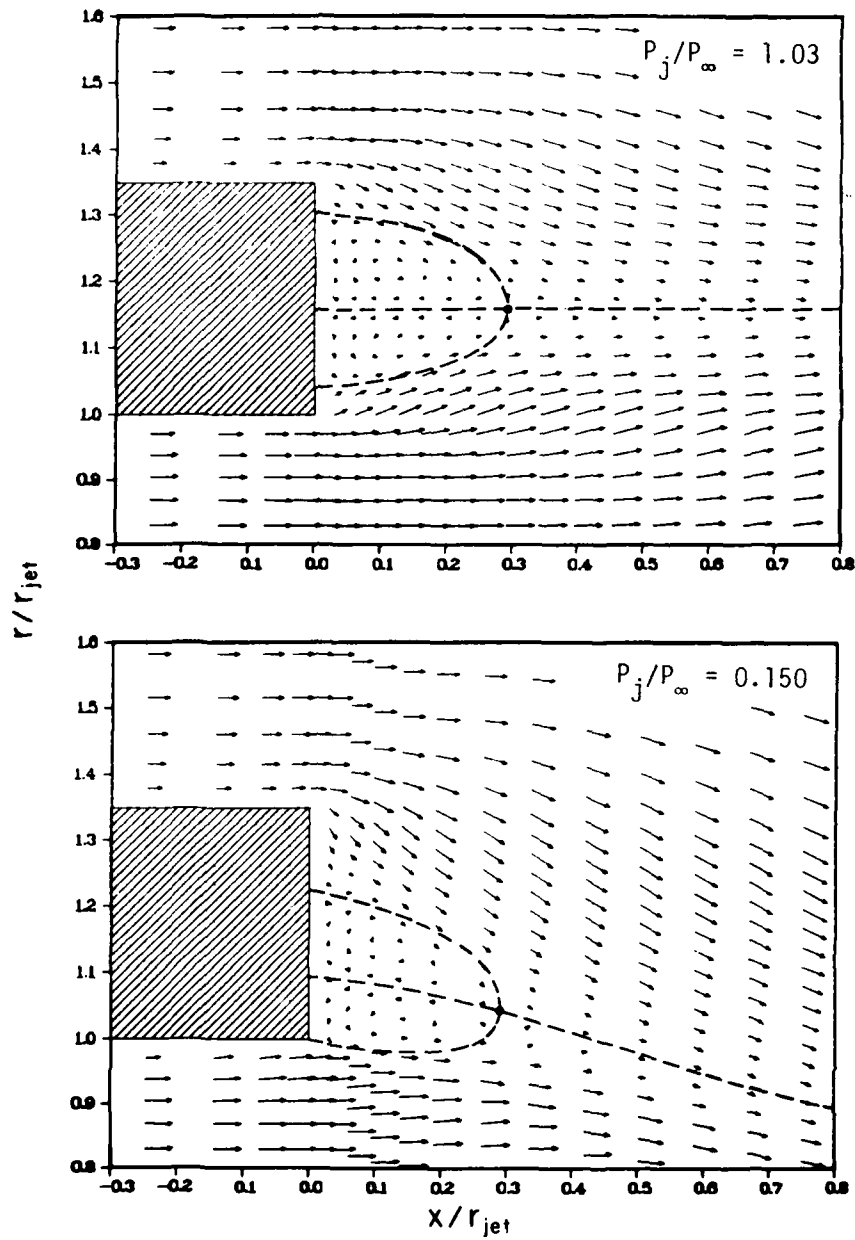


Figure 34. Computed Velocity Fields in the Near Wake Region of the Nozzle Base Annulus

at  $P_j/P_\infty = 1.03$  to one with an asymmetric nature at  $P_j/P_\infty = 0.150$ . In this figure the dashed lines denote the dividing streamline and the streamlines through the stagnation point in the near wake flow for each case. As shown in Figure 35, the dividing streamline moves toward the inner wall of the nozzle as the total pressure in the jet is decreased. Although the stagnation point in the near wake region moves radially as the jet stagnation pressure is changed, it remains in a relatively constant position axially for the cases computed.

Quantitative comparisons between the experimental data and the computed solutions are based primarily on two parameters: the axial distance along the centerline from the nozzle exit plane to the point of reflection of the incident shock wave at the line of symmetry, and the value of the nozzle base pressure coefficient. This reflection length, along with the type of shock reflection (either strong or weak), is a good indication that the inviscid flow features in the jet core caused by viscous-inviscid

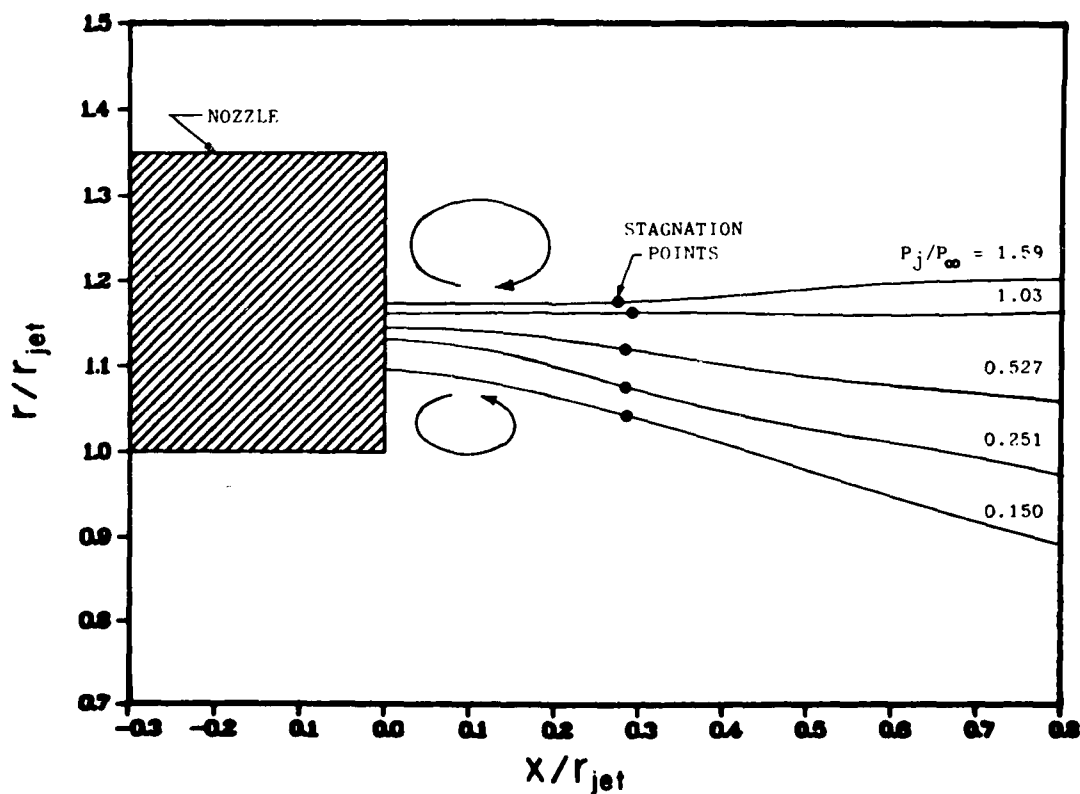


Figure 35. Position of the Dividing Streamline in the Computational Nozzle Solutions

interaction are properly simulated. These computed shock reflection lengths are obtained by examining the axial variation in Mach number along the centerline as shown in Figure 36 for a typical case. As shown in this figure, the shock reflection is diffused over three cell lengths, with the computational value of the reflection length taken as being at the midpoint of these three cells. Comparisons between the experimental and computational values of these reflection lengths are shown in Figure 37 and Table 4. Excellent agreement was obtained, with the computational results being within 2% of the experimental data.

An additional quantitative comparison was also made of the computed and observed Mach disc radii for the two cases at which the Mach disc was observed. This comparison is listed in Table 5. The computed Mach radius was taken as the radial height of the sonic line immediately behind the strong shock wave. Very good agreement was obtained for the highly

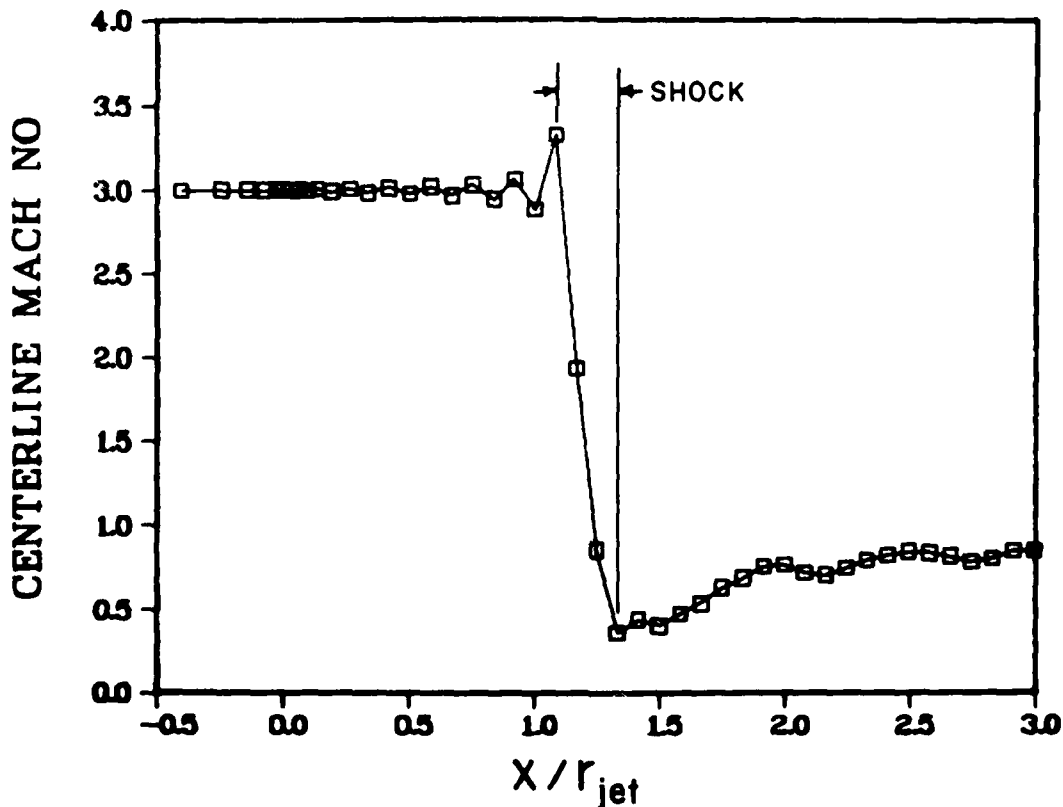


Figure 36. Axial Variation in Computed Centerline Mach Number,  
 $P_j/P_\infty = 0.150$

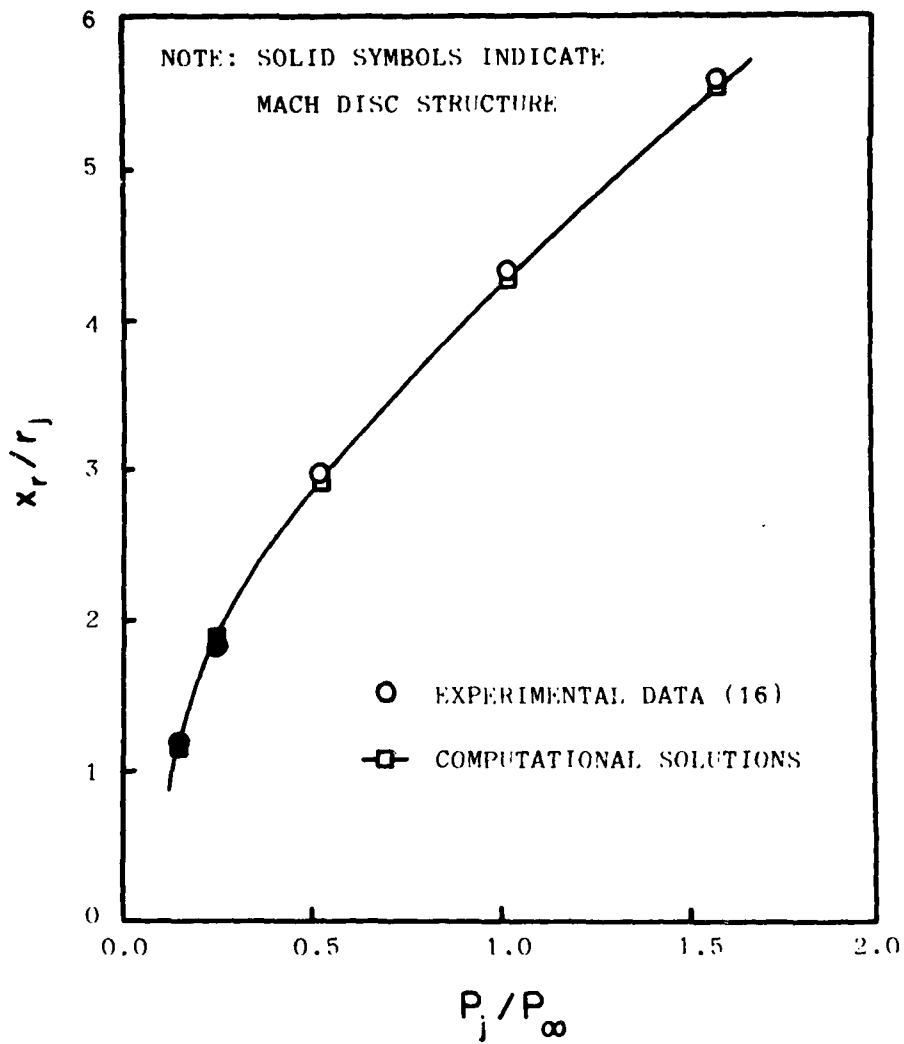


Figure 37. Shock Reflection Lengths Along the Nozzle Centerline vs Nozzle Pressure Ratio



TABLE 4

## COMPARISON OF SHOCK REFLECTION LENGTHS

$P_j/P_\infty$	Experimental $x_r/r_{jet} (+0.05)$	Computational $x_r/r_{jet} (+0.04)$	% Error
0.150	1.19	1.17	-0.3
0.251	1.88	1.91	+0.5
0.527	2.98	2.91	-1.2
1.030	4.37	4.26	-1.9
1.590	5.64	5.53	-2.0

TABLE 5

## COMPARISON OF MACH DISC RADII

$P_j/P_\infty$	Experimental $r_m/r_{jet} (+0.05)$	Computational $r_m/r_{jet} (+0.04)$	% Error
0.150	0.45	0.44	-2.2
0.251	0.17	0.06	-24.

overexpanded case ( $P_j/P_\infty = 0.150$ ) in which a fairly large Mach disc occurs. Poorer agreement was obtained for the case that was much nearer to transition to a regular shock reflection, with a very small Mach disc radius ( $r_m/r_{jet} = 0.17$ ). The first cell height adjacent to the centerline in the computational solution possessed a value of  $r/r_{jet} = 0.06$ , so that numerical truncation error played a large part in the discrepancy between the experimental and computed values of the Mach disc radial height at this pressure ratio condition.

Comparisons between the experimental and computational values of nozzle base pressure coefficient are shown in Figure 38 and Table 6. Since the experimental data points for the base pressure coefficients were not obtained at the same pressure ratio values as the Schlieren data, experimental values for the base pressure coefficients in Table 6 were interpolated from the available data points at the five given nozzle pressure ratios. Values of the computed nozzle base pressure were in

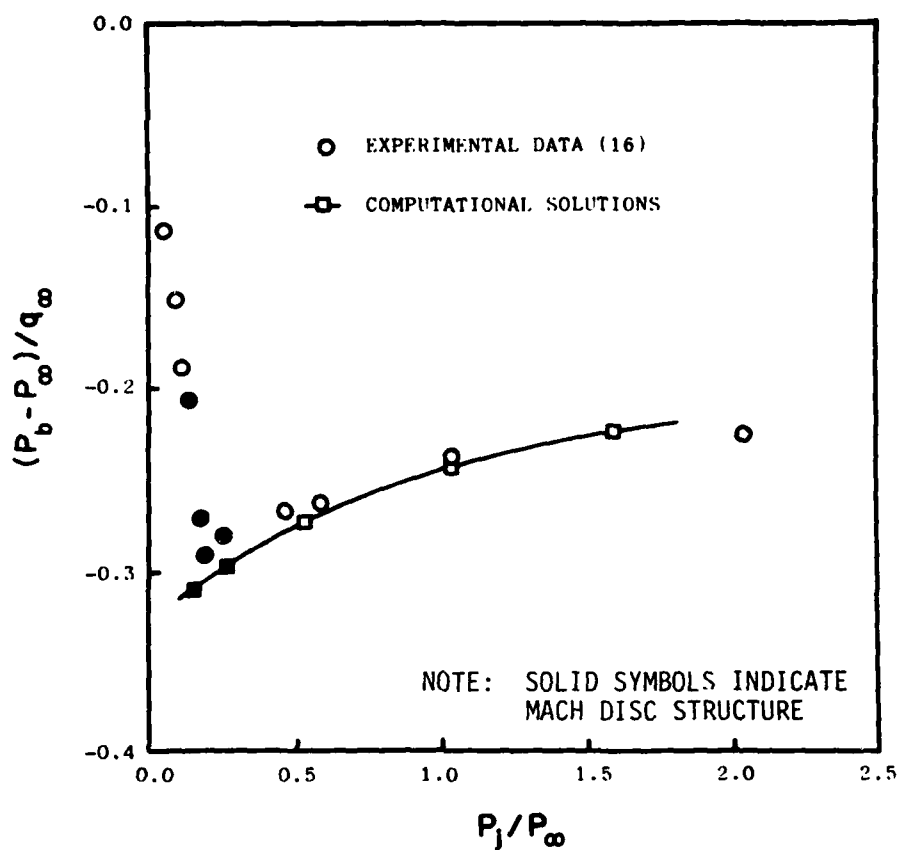


Figure 38. Base Pressure Coefficient vs Nozzle Pressure Ratio

TABLE 6

COMPARISON OF BASE PRESSURE COEFFICIENTS

$P_j/P_\infty$	Experimental* $p_B (+0.003)$	Computational $p_B (+0.002)$	% Error
0.150	-0.240	-0.310	-25.0
0.251	-0.280	-0.299	- 6.8
0.527	-0.265	-0.276	- 3.9
1.030	-0.237	-0.245	- 2.9
1.590	-0.226	-0.219	+ 2.5

good agreement with the experimental data (3-7% error), with the exception of the highly overexpanded case at which  $P_j/P_\infty = 0.150$ . Figure 38 shows that as the pressure ratio of the nozzle is lowered, the decreasing trend in nozzle base pressure reverses at a value of approximately  $P_j/P_\infty = 0.18$  and sharply increases as the pressure ratio is further reduced. This sudden reversal in behavior is apparently due to flow separation in the divergent portion of the nozzle which prevents the jet flow from expanding fully to its assumed Mach 3.0 state. For pressure ratio values less than  $P_j/P_\infty = 0.135$ , the shock structure in the jet core transitions back to a regular shock reflection as shown in Figure 39. The schlieren photographs in Figure 39 indicate that for values less than  $P_j/P_\infty = 0.135$ , either the jet Mach number is less than 1.48 and thus cannot support a Mach disc structure (Reference 8), or the increase in nozzle static pressure due to the reduced expansion cannot produce the deflection angle in the jet flow needed for a Mach disc to occur. A non-separated condition was assumed by the experimental investigators, since their value of  $P_j$  was determined using the jet total pressure and the final area ratio of the nozzle. Likewise, the computational solutions assumed non-separated Mach 3 flow just upstream of the nozzle exit plane. If some separation did occur and the nozzle flow did not fully expand to a Mach 3 condition, a substantial difference in base pressure could result.

This hypothesis of separation in the nozzle was partially confirmed by computationally solving a case where the jet total pressure corresponded to the attached case ( $P_j/P_\infty = 0.150$ ), but with jet flow to a Mach number of only 2.60 as detailed in Appendix E. A correct strong shock structure was obtained computationally, and the value of the base pressure coefficient increased to a value of -0.265. This was in much better agreement with the experimental data at this condition (see Figure 38). A more accurate simulation of this pressure ratio condition would require extending the computational mesh back to the nozzle throat. Separation in the nozzle could then occur in a direct manner in the numerical solution. Since this would require extensive grid revisions as well as additional computer resources, it was considered to be beyond the scope of this investigation.



$$p_j/p_\infty = 0.124$$



$$p_j/p_\infty = 0.132$$



$$p_j/p_\infty = 0.135$$



$$p_j/p_\infty = 0.150$$

Figure 39. Schlieren Photographs (Reference 16) Showing the Eventual Deterioration of the Mach Disc with Decreasing Nozzle Pressure Ratio

## SECTION VII

## CONCLUSIONS AND RECOMMENDATIONS

A numerical method of obtaining solutions to the Navier-Stokes equations for axisymmetric nozzles in supersonic external streams has been developed from a selection of appropriate techniques. Based on the numerical analysis and computational results obtained through this study, the following conclusions are drawn:

1. The numerical solution of the Navier-Stokes equations applied to axisymmetric nozzles successfully reproduced all of the essential flow features including boundary layers, corner expansions, recompression snocks, the recirculation region adjacent to the nozzle base wall and the evolution of the near wake to a flow with far wake behavior.
2. The numerical method achieved a correct transition from regularly reflected shock waves at the line of symmetry in the jet core flow to a strong Mach disc formation at the appropriate static pressure ratio condition of the nozzle. The subsonic embedded region immediately behind the Mach disc formation was simulated in a correct manner.
3. The application of an adaptive grid scheme in the wake region of the nozzle annulus successfully positioned the fine mesh region of the computational grid in the wake region which normally contains severe flow gradients. This allowed the accurate simulation of this high flow gradient region while conserving numerical resources.
4. The nozzle base pressure was heavily dependent on the eddy viscosity model applied in the region of the near wake. Once the model was tuned for the neutrally expanded case ( $P_j/P_\infty = 1.03$ ), good agreement was obtained computationally for all cases where the flow obeyed the assumption of remaining attached in the divergent portion of the nozzle.
5. Boundary conditions must be carefully formulated and applied in order to prevent physically unrealistic results or numerical divergence of the solution. Both the centerline and downstream boundaries were sensitive where regions of subsonic flow occurred over a substantial portion of the boundary. Both the quadratic extrapolation used in

regions of supersonic flow and a second order, zero gradient condition caused either divergence or unrealistic conditions at the boundary when applied to regions of subsonic flow. A first order zero gradient condition was used successfully in these regions of subsonic flow and found to be superior. Generalizations about the success of this first order boundary condition cannot be made, since the degree of success achieved is dependent on the specific numerical algorithm applied to the problem.

6. The final steady state solutions were found to be insensitive to the initial conditions applied over the computational domain. However, the time to converge to the final solution was highly dependent on the application of specific initial conditions. In particular, the region of subsonic recirculation in the near wake was the last region in the solution domain to converge. Solutions started using only the boundary layer profiles across the domain required three hours to converge on a Cyber 175 (45 x 45 point mesh), whereas cases started from a previous different jet total pressure condition but with an established near wake structure required only 1.7 hours to converge (45 x 45 mesh).
7. To the author's knowledge, this is the first full Navier-Stokes solution that has accurately simulated the viscous-inviscid interactions present in a dual stream nozzle flowfield at off-design conditions where the strong Mach disc shock structure is present. Mikhail (Reference 8) previously was unsuccessful in reproducing the Mach disc reflection in a full Navier-Stokes solution due to the probable improper placement of the jet inflow boundary condition which did not allow the jet plume to expand to the degree necessary to generate a Mach disc reflection.

Based on the numerical analysis and results obtained through this study, the following recommendations are made:

1. The present scalar computer code developed during the course of this investigation should be vectorized for use on the new generation of "supercomputers" such as the CRAY-1 or the Cyber 203. Although present solution times are on the order of two to four hours when

run on a Cyber 175 computer, a fully vectorized version of the present computer code can be expected to converge within five minutes on a CRAY-1 computer (Reference 39). This will allow computation of more complex nozzle geometries and better resolution in the boundary layers through the application of finer mesh, while holding costs to a reasonable level.

2. The present numerical solver should be modified to include the effects of a calorically imperfect gas with variable specific heat and thermal conductivity. This modification would allow accurate simulation of the temperature dependent effects for hot exhaust nozzles with gas temperatures less than 5000°R (Reference 19). Only minor revisions to the existing computer code would be required in order to include these temperature effects.
3. After the implementation of the two previous recommendations, it would be desirable to incorporate the effects of species mixing into the numerical solver. Many practical cases of interest involve a jet exhaust gas with a different species than that of the external stream. This modification would require a significant code revision, since the addition of the equation of mass diffusion would be required, as would the correct modeling of appropriate mass diffusion coefficients.

## APPENDIX A

## NOZZLE WALL TEMPERATURE CALCULATION

The nozzle wall boundary condition applied during the numerical solution procedure assumes a constant nozzle wall temperature within the computational domain. The relatively high thermal conductivity of the stainless steel nozzle makes this assumption valid. This wall temperature can be calculated by applying a heat flux balance across the freestream boundary layer, the nozzle wall, and the jet boundary layer as shown in Figure 40. Conduction of heat in the axial direction is neglected due to the low temperature gradients in this direction.

Since both the freestream and the jet flow are of a high-velocity nature, the unit heat flux for either stream can be written as (Reference 40):

$$\dot{q}_{w_i} = h_i (T_{aw_i} - T_w) \quad (A-1)$$

where  $h_i$  is the heat conductance of each flowstream. The adiabatic wall temperature,  $T_{aw_i}$ , is defined by the expression:

$$T_{aw_i} = T_i \left( 1 + \frac{n}{Pr} \left( \frac{\gamma-1}{2} \right) M_i^2 \right) \quad (A-2)$$

where  $n$  is  $1/2$  for laminar flow and  $1/3$  for turbulent flow. Equating the heat flow out of the control volume for a steady state process gives:

$$\sum_i \dot{q}_i = 0 \quad (A-3)$$

or

$$2\pi r_{\infty}^{j_0} \dot{q}_{\infty} + 2\pi r_j^{j_0} \dot{q}_j = 0 \quad (A-4)$$

where  $j_0$  is either 0 or 1 for two-dimensional or axisymmetric flow, respectively.



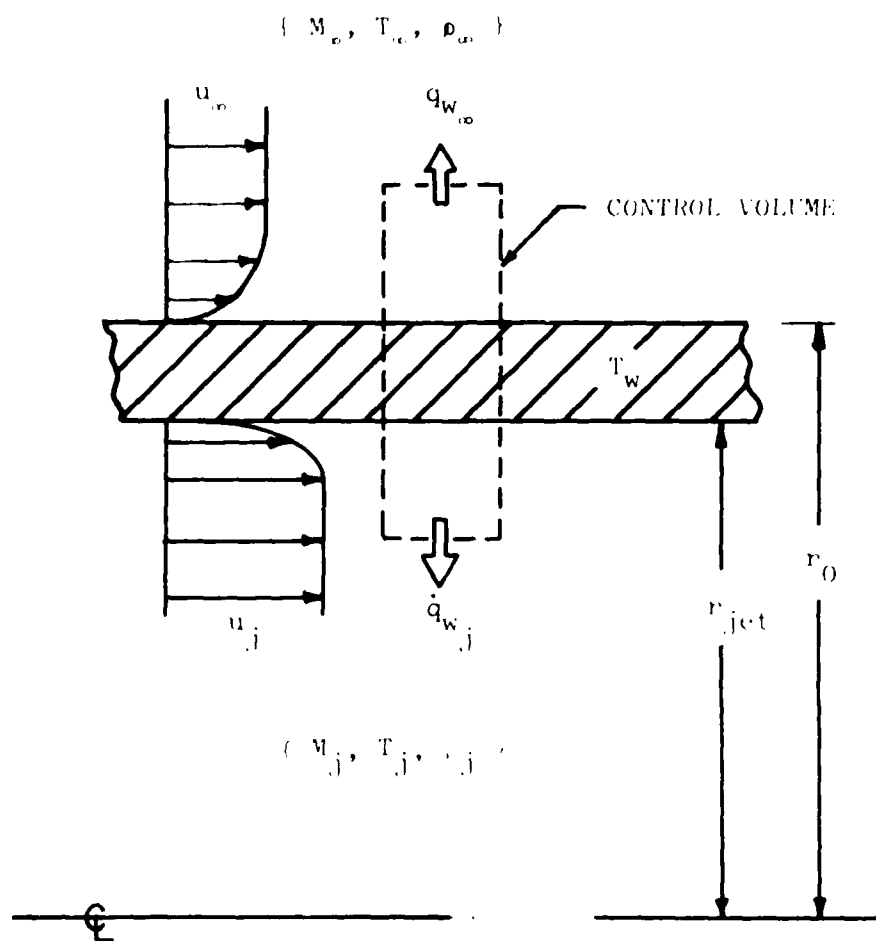


Figure 40. Heat Flux Balance Used to Determine the Nozzle Wall Temperature

Applying Equation A-1 to the values of the individual heat fluxes and solving for the wall temperature gives:

$$T_w = \frac{T_{aw_j} + (r_o/r_j)^{j_o} (h_o/h_j) T_{aw_o}}{[1 + (r_o/r_j)^{j_o} (h_o/h_j)]} \quad (A-5)$$

For flows involving a constant boundary layer edge velocity and a constant wall temperature, the conductances,  $h_i$ , can be defined by the following analytic expressions:

$$h_i = 0.332 C_p \rho_i u_i Re_{xi}^{-1/2} Pr^{-2/3} \quad (A-6)$$

for laminar flow, and

$$h_i = 0.0295 C_p \rho_i u_i Re_{xi}^{-1/5} Pr^{-2/5} \quad (A-7)$$

for turbulent flow (Reference 40). All of the quantities on the right-hand-side of Equation A-5 are then known, and a value for the wall temperature can be calculated based on the states of the two flowfields adjacent to the nozzle wall.

## APPENDIX B

## ADAPTIVE FINITE DIFFERENCE MESH

It is desirable that the fine mesh region of the computational grid remain in the areas of relatively high velocity and temperature gradients as the solution progresses towards convergence. Hirt (Reference 21) has used a technique in the solution of free surface flows that allows the grid to adapt as the solution progresses. The following kinematic equation is applied in the region where the nozzle wake and shear layer develop:

$$\frac{\partial r}{\partial t} = C_A (v - u \frac{\partial r}{\partial x}) \quad (B-1)$$

This equation ensures the condition that as the solution converges, the physical slope of the constant  $n$  finite difference cell boundaries is the same as that of the velocity vectors near each cell.

Equation B-1 can be converted to the following finite difference form for application to a computational mesh:

$$r_{i,j}^{n+1} = r_{i,j}^n + C_A \Delta t [\bar{v}_{i,j}^n - \bar{u}_{i,j}^n \left( \frac{r_{i,j}^n - r_{i-1,j}^n}{x_{i,j}^n - x_{i-1,j}^n} \right)] \quad (B-2)$$

where

$$\bar{u}_{i,j}^n = 1/4 (u_{i-1,j}^n + u_{i+1,j}^n + u_{i,j-1}^n + u_{i,j+1}^n) \quad (B-3)$$

$$\bar{v}_{i,j}^n = 1/4 (v_{i-1,j}^n + v_{i+1,j}^n + v_{i,j-1}^n + v_{i,j+1}^n) \quad (B-4)$$

and where  $C_A$  is a constant used to damp the grid motion with respect to time. Spatial averaging of the velocity components is applied in order to reduce the effects of numerical velocity fluctuations at individual mesh points in the flow. The upwind difference form of the cell aspect ratio term  $(\Delta r / \Delta x)$  is also utilized to achieve better stability in the finite difference equation.

Equation B-1 is applied in the wake region of the flowfield for a line of constant  $\eta$  ( $j=\text{constant}$ ), where the specific value of  $\eta$  corresponds to the nozzle inner wall for overexpanded flowfields, and to the nozzle outer wall for underexpanded flowfields. Once the position of this grid reference line is established, the fine mesh region corresponding to the wall thickness is computed. The exponential stretching scheme discussed in Section III is then applied for each value of  $\xi$  in the regions above and below the fine mesh region as shown in Figure 41. The first two grid points above the centerline were kept fixed at constant heights for all values of  $x$ . This prevented large numerical errors in axisymmetric cases involving the differencing of terms containing  $(1/r)$ , where  $r$  is a very small number.

The constant  $C_A$  was specified in the range of 0.3 - 0.6 in order to allow the grid to adapt smoothly as the solution converged. Larger values of  $C_A$  caused undesirable oscillatory motion of the grid reference line with respect to time.

The adaptive grid scheme was applied once during every iteration of the solution algorithm. The number of points allowed to "float" on the grid reference line could be varied during the course of the solution. This capability was utilized primarily during the start-up portion of the numerical solution, where only a limited number of points close to the nozzle were allowed to "float" until the shear layer was established. After the position of the shear layer across the complete computational domain was completely established, the adaptive grid scheme could be turned off in order to save computer time during the remainder of the solution.

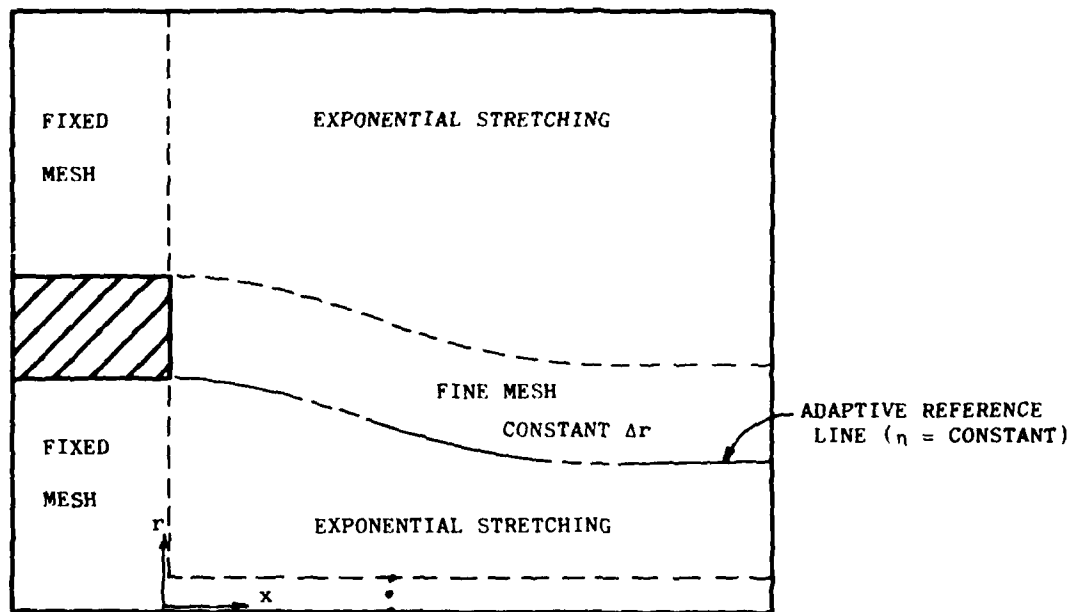


Figure 41. Adaptive Mesh Schematic

## APPENDIX C

## TWO-DIMENSIONAL FLAT PLATE FAR WAKE SOLUTION

In order to test the validity of the turbulence model in the far wake region, a check case possessing known experimental data in this region was computed. The experimental data for this case is that of Toyoda and Hiriyama (Reference 33), which involved a two-dimensional thin flat plate at a Mach number of 1.60. The flat plate possessed a thickness of  $3.28 \times 10^{-3}$  ft (1 mm) and a trailing edge thickness of  $3.28 \times 10^{-4}$  ft (0.1 mm).

The following flow quantities were given in the experimental data:

$$M_{\infty} = 1.60$$

$$P_{\infty} = 3.2 \text{ atm}$$

$$Re_{\theta} = 5300$$

A free stream stagnation temperature of  $518.7^{\circ}\text{R}$  was assumed, since this value was not given experimentally. The wall temperature of the plate was also set to  $518.7^{\circ}\text{R}$ . Using the previous quantities, the boundary layer momentum thickness at the trailing edge was computed as:

$$\theta_{TE} = 2.95 \times 10^{-4} \text{ ft}$$

The computational solution used the same numerical solver (MacCormack's explicit method) as that of the nozzle solutions. The eddy viscosity models utilized were identical with those used in the boundary layer and far wake regions of the axisymmetric nozzle. The boundary conditions utilized also closely resemble those of the nozzle. The inflow conditions were set by the experimental data and remained fixed for the duration of the solution. The upstream  $u$  component of velocity near the trailing edge of the plate was matched to that of the experimental data as shown in Figure 42. Input conditions at the upstream boundary were then set as:

$$u(x_1, y, t) = 0.6295 u_{\infty} (y/\theta_{TE})^{1/5} \quad (C-1)$$

$$v(x_1, y, t) = 0.0 \quad (C-2)$$

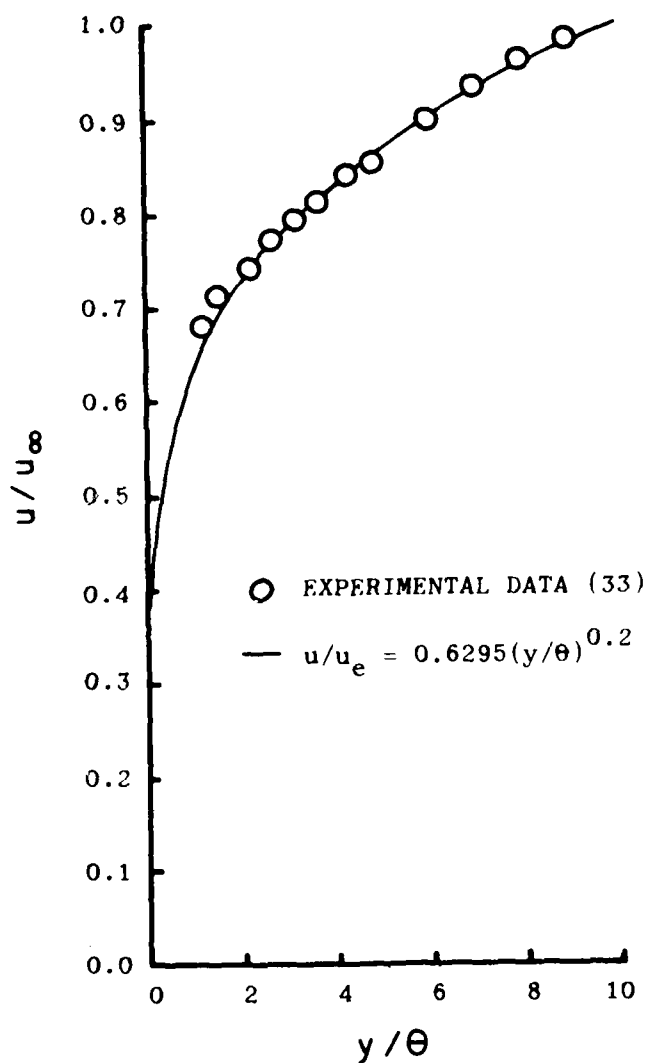


Figure 42. Velocity Profile at the Trailing Edge of the Two-Dimensional Flat Plate

$$\rho(x_1, y, t) = \rho_\infty / \{1 + \frac{(\gamma-1)}{2} M_\infty^2 [1 - (u(x_1, y, t)/u_\infty)^2]\} \quad (C-3)$$

$$P(x_1, y, t) = P_\infty \quad (C-4)$$

Both the upper and lower freestream boundaries utilize the characteristic condition applied at the upper boundary of the nozzle solutions. The outflow and wall boundaries used conditions identical to those utilized for the nozzle. The computational solution was initially started by applying the upstream profile across the computational domain:

$$U(x, y, 0) = U(x_1, y, 0) \quad (C-5)$$

This calculation utilized a 39x34 computational mesh, with exponential mesh stretching employed in both the x and y directions as shown in Figure 43. Minimum grid spacings in the x and y directions were  $4.00 \times 10^{-4}$  ft and  $3.28 \times 10^{-4}$  ft, respectively. The physical dimensions of the computational flowfield in the x and y directions were 0.125 ft and 0.070 ft, respectively. The rate of data processing on a CDC Cyber 175 computer was 0.0014 sec per grid point for each iterative time step. The solution was computed for a duration of four characteristic times (3200 iterations), at which time no significant change was detected in the dependent variables. The result was then taken to be the asymptotic solution.

The computational solution demonstrated that the eddy viscosity model gives good results in the far wake region. The maximum velocity defect generated computationally is in good agreement with the experimental data as shown in Figure 21. Figure 44 shows that the velocity field generated computationally evolves from the boundary layers on the plate to a classic wake solution very rapidly due to the turbulent nature of the flow.



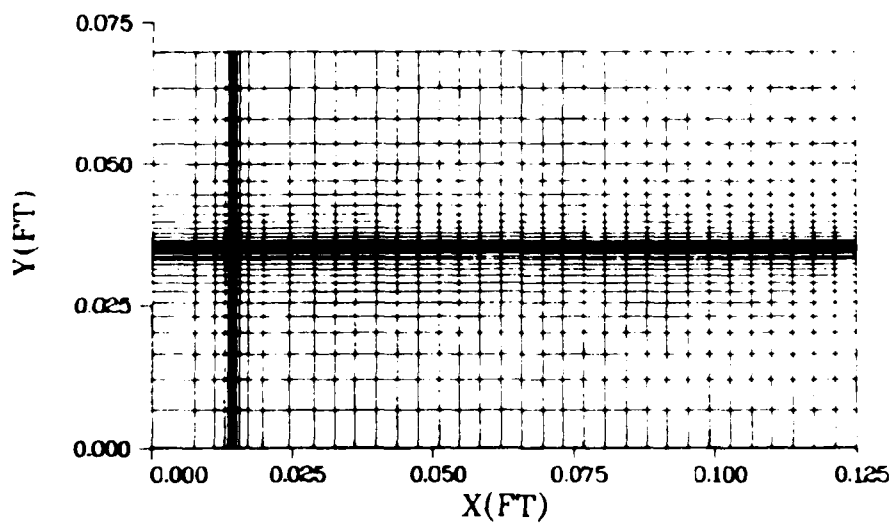


Figure 43. Computational Mesh Used in the Flat Plate Solution

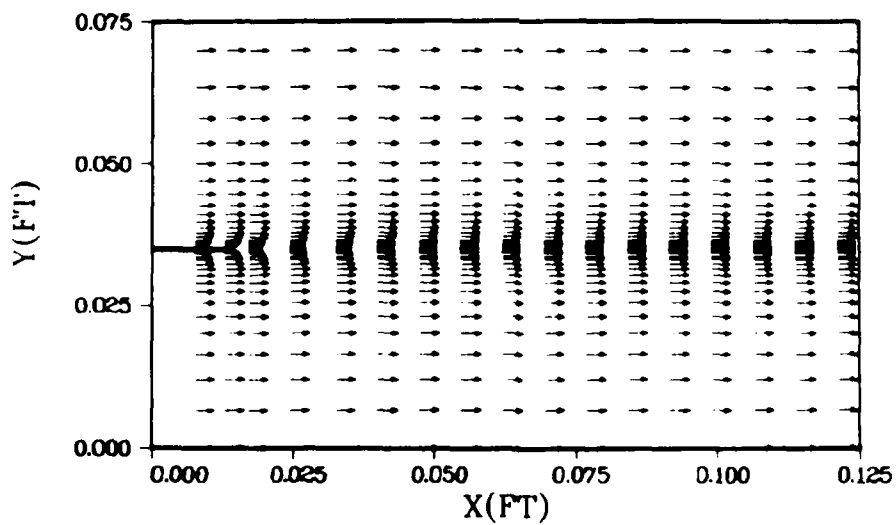


Figure 44. Computed Flat Plate Velocity Profiles

## APPENDIX D

## TWO-DIMENSIONAL WEDGE-FLAT PLATE NEAR WAKE SOLUTION

In order to test the validity of the turbulence model utilized in the near wake region of the coflowing nozzle solutions, a check case exhibiting similar physical characteristics and possessing known experimental data in this region was solved numerically. The experimental case selected for this validation study is one obtained by Rom, Seginer and Kronzon (Reference 35) for a two-dimensional wedge-flat plate in a turbulent supersonic flowfield. The model used for this study consisted of a sharp  $15^\circ$  half angle wedge-flat plate with a base height of 10 mm and a chord of 44 mm. The following flow conditions were given in the experimental data:

$$M_\infty = 2.25$$

$$Re_c = 1.5 \times 10^6$$

$$P_{o_\infty} = 40 \text{ psig}$$

$$T_{o_\infty} = 492^\circ \text{ R}$$

A computed adiabatic wall temperature of  $467^\circ\text{R}$  based on the flow condition at the flat plate portion of the model was used in the computational solution.

The numerical solution used the same computational solver and turbulence model as that of the coflowing nozzle solutions. The boundary and initial conditions were also identical to those used in the coflowing nozzle with the exception of the jet centerline condition. As shown in Figure 45, this condition was replaced with a lower freestream boundary which utilized a characteristic scheme similar to that of the upper freestream boundary. Since a value for the boundary layer thickness near the trailing edge was given experimentally ( $\delta/h = 0.15$ ), a two-dimensional boundary layer code was used to generate the velocity and temperature profiles on the upstream boundary. The boundary layer starting length was adjusted to give the correct boundary layer thickness. One additional condition was imposed on the line of symmetry for the wedge ( $j = 23$ ).

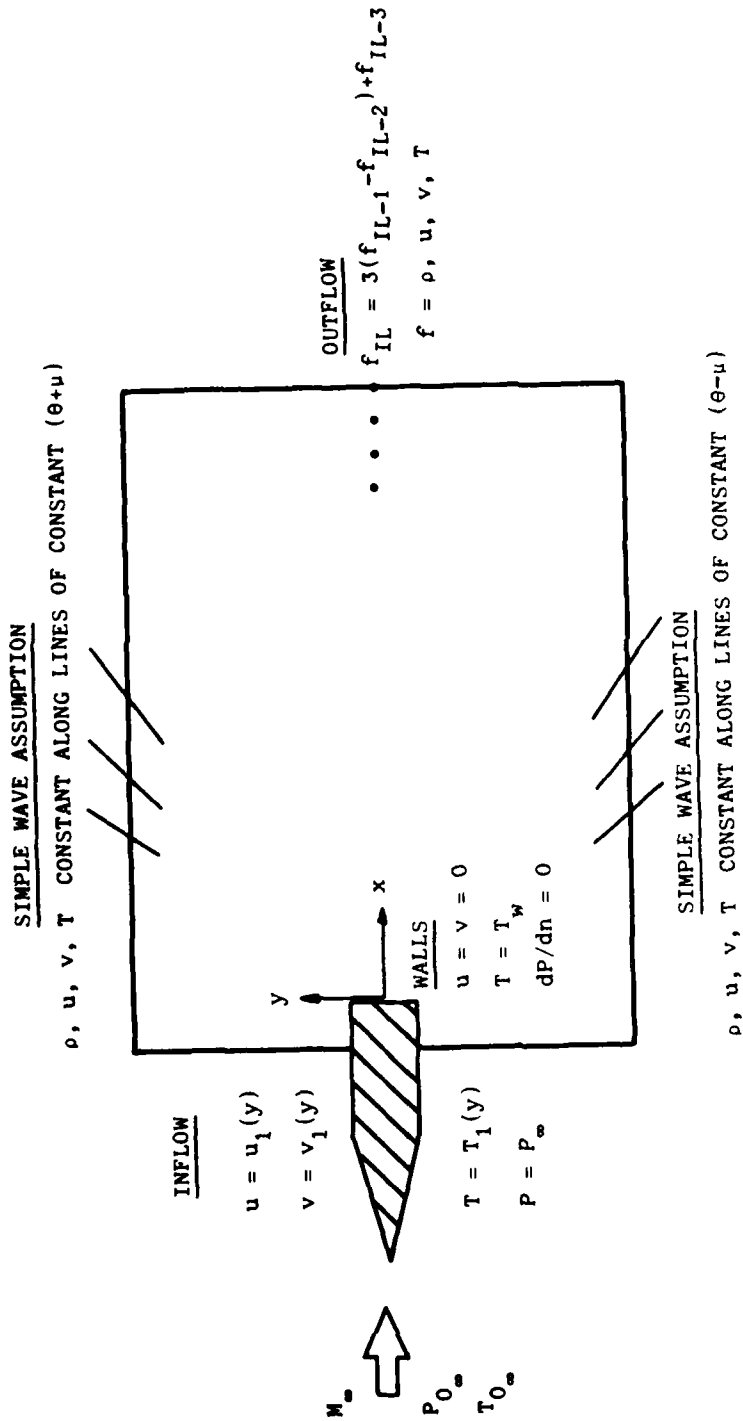


Figure 45. Computational Boundary Conditions for the Two-Dimensional Wedge-Flat Plate

At this line of symmetry, a zero  $v$  velocity component was enforced to help stabilize the wake during the startup of the numerical solution and help accelerate convergence by damping any numerical shear layer oscillations in the wake.

The solution was calculated using a  $45 \times 45$  point computational mesh with exponential stretching employed in both the  $x$  and  $y$  directions as shown in Figure 46. The physical dimensions of the computational flowfield in the  $x$  and  $y$  directions were 10cm and 7cm, respectively. Minimum grid spacing in the  $x$  and  $y$  directions was set at 0.5 mm. This gave a value of  $u/u_e = 0.83$  for the first point in the boundary layer above the nozzle wall, which corresponds to an identical value in the jet boundary layer of the axisymmetric nozzle solutions. Thus, truncation error should be similar in this region for both the wedge-flat plate and the nozzle. The rate of data processing on a CDC Cyber 175 computer was 0.0014 sec per grid point for each iterative time step. The solution was allowed to progress for approximately four characteristic timesteps at which time the change in the dependent variables was less than 0.5% per characteristic time period. This condition was then considered to be the converged asymptotic solution.

Specific features of the experimental flowfield in the near wake were reproduced in the computational solution and can be distinguished in the plots of Mach number contours and velocity profiles shown in Figures 47 and 48. Several flow features which were numerically observed include the existence of the boundary layers along the horizontal walls of the body, the turning of the flow through the corner expansion fans, the existence of the subsonic recirculating "deadwater" region adjacent to the base of the body, flow recompression through the trailing shocks, and the evolution of the wake to a classic far wake flow. The weak lip shock evident in the experimental data was not readily evident in the numerical solution. This may be attributed to the fact that the numerical method tends to smear shocks, and thus has difficulty locating shocks which are very weak.

Quantitative accuracy of the numerical solution is identified through the use of the given experimental static pressure and pitot pressure data. A comparison of the axial static pressure distribution along the line of symmetry is shown in Figure 49. The computed static

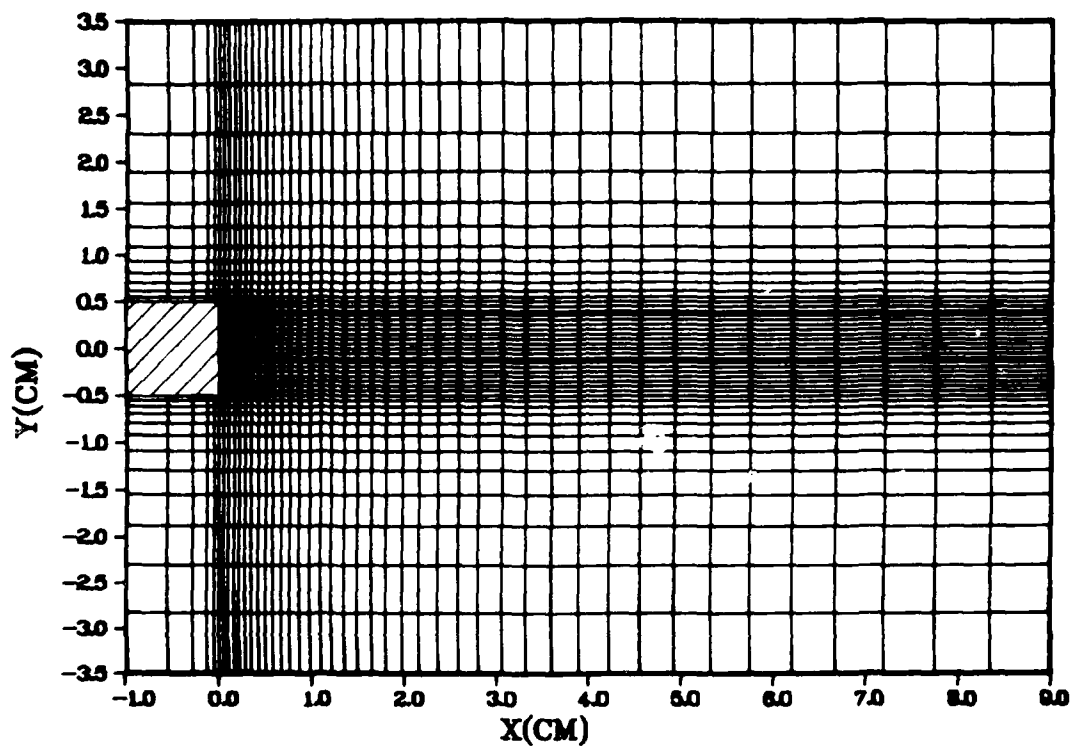


Figure 46. Computational Mesh Used for the Two-Dimensional Wedge-Flat Plate Solution

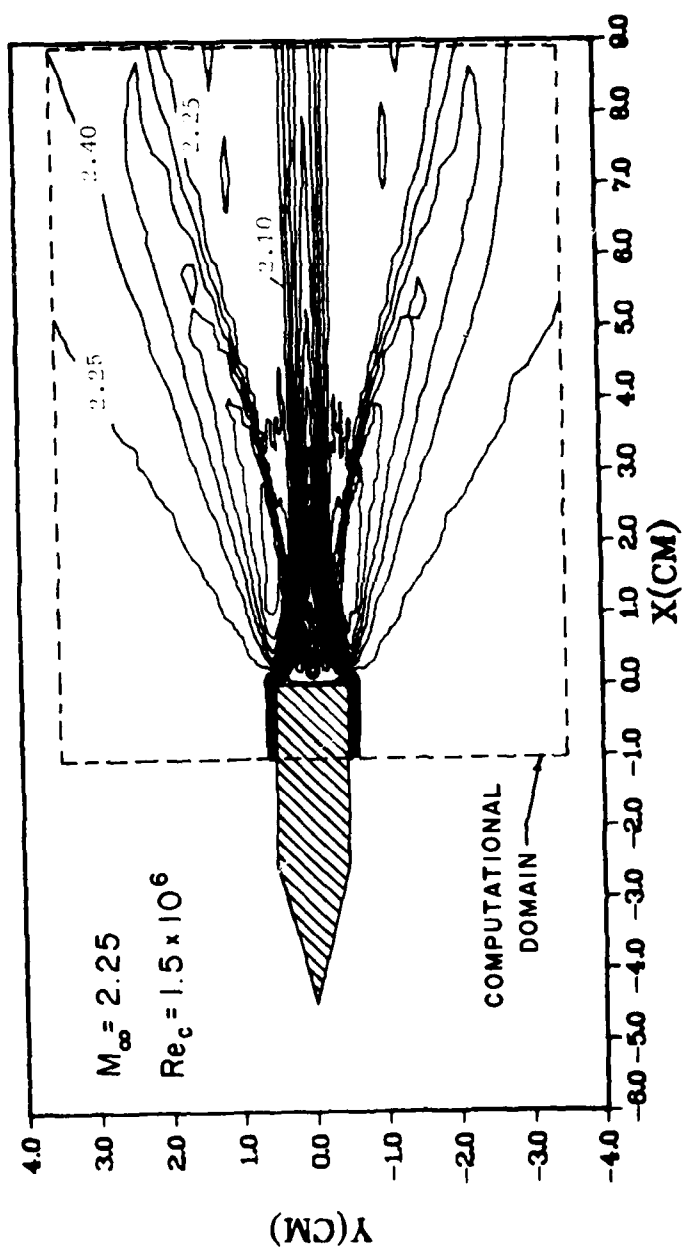


Figure 47. Two-Dimensional Wedge-Flat Plate with the Computed Mach Number Contours Shown

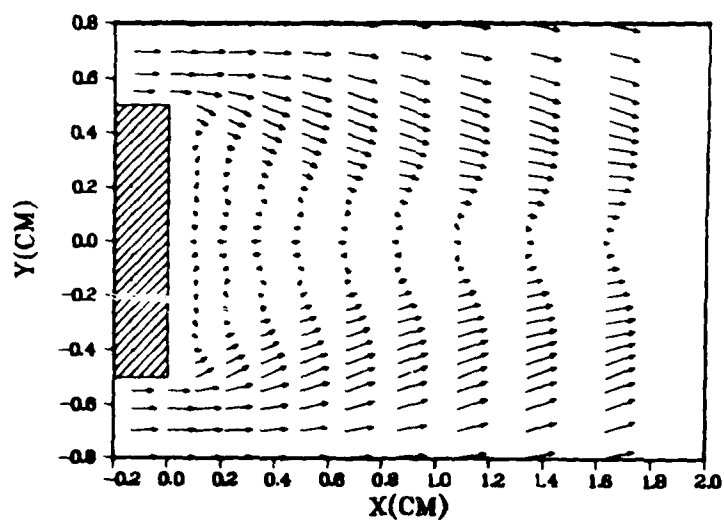


Figure 48. Computed Velocity Profiles in the Near Wake of the Two-Dimensional Wedge-Flat Plate

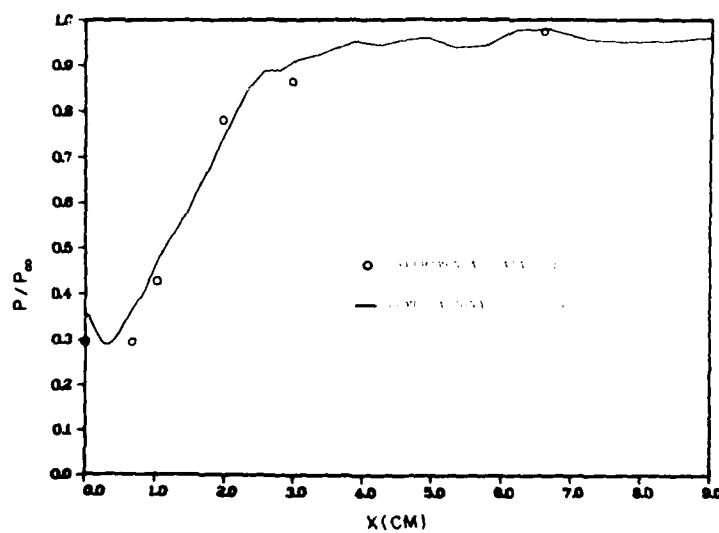


Figure 49. Static Pressure Along the Line of Symmetry in the Near Wake of the Two-Dimensional Wedge-Flat Plate

pressure distribution is within 5% of the measured values except in the region of recirculating flow ( $x \leq 1.0\text{cm}$ ), where there is up to a 7% discrepancy between the experimental and computed values. However, static pressure probes like the one used to obtain the data are very sensitive to flow angularity, and thus less reliable in areas of recirculating flow. A more reliable comparison is that of the pitot-pressure surveys shown in Figure 50. These measurements are less susceptible to errors resulting from flow angularity. This figure shows excellent agreement in the "deadwater" region of recirculating flow. The numerical solution smears the weak beginning of the recompression trailing shocks at  $0.5\text{cm}$ , but correctly simulates them at the correct values further downstream ( $x \geq 1.0$ ). This figure particularly demonstrates that the phenomena present in the near wake are accurately simulated by the present computational method and turbulence modeling.

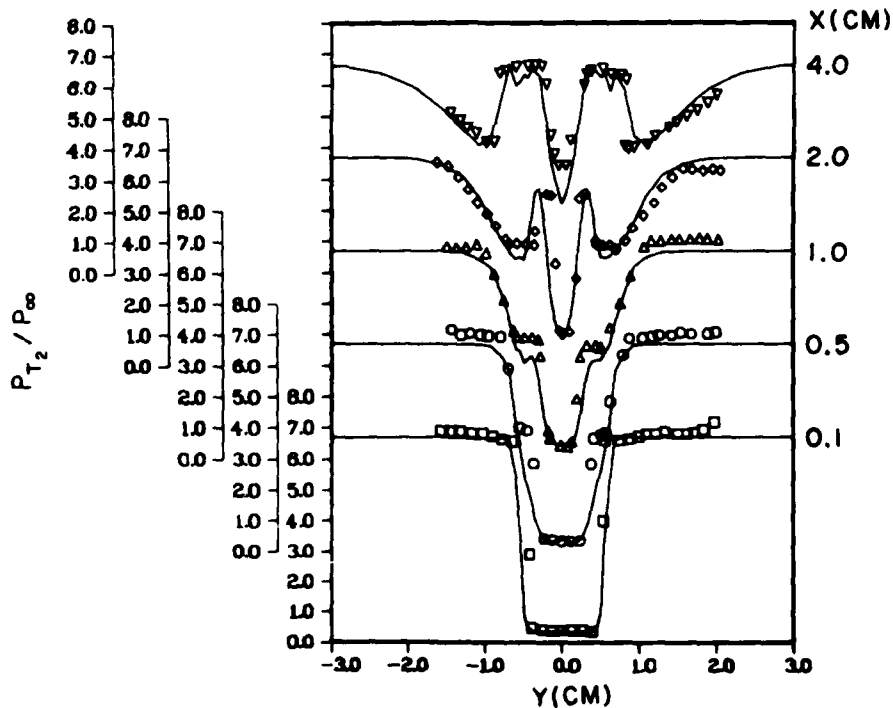


Figure 50. Pitot Pressure Profiles in the Near Wake of the Two-Dimensional Wedge-Flat Plate (Symbols-Experimental Data (Reference 34), Solid Lines - Computational Solution)



## APPENDIX E

AXISYMMETRIC NOZZLE SOLUTION SIMULATING INTERNAL  
BOUNDARY LAYER SEPARATION

The peculiar reversal in the nozzle base pressure coefficient as the pressure ratio was lowered below  $P_j/P_\infty = 0.18$  was believed to be caused by boundary layer separation in the divergent portion of the nozzle (Figure 38). This was further substantiated through an examination of the schlieren photographs (Reference 16) which show a definite change in flow character near this value (Figure 39). To test this hypothesis a numerical solution was computed for a case where the jet total pressure corresponded to that of the attached strong shock solution ( $P_j/P_\infty = 0.15$ ), but where the jet Mach number equals 2.60 based upon an isentropic expansion in the nozzle. For this jet Mach number a reduction in nozzle area ratio was assumed from  $A/A^* = 4.2$  at Mach 3 to  $A/A^* = 2.9$  at Mach 2.60. This reduced expansion rate was intended to roughly simulate the effects of boundary layer separation in the nozzle, while retaining grid geometry and fineness identical to the previously calculated attached jet flow case.

The following jet flow parameters were used in this solution:

$$\begin{aligned}M_j &= 2.60 & T_w &= 551.0^\circ R \\T_{oj} &= 580.5^\circ R \\P_{oj} &= 1636 \text{ psf}\end{aligned}$$

These jet conditions produce an actual nozzle pressure ratio of  $P_j/P_\infty = 0.276$  versus the calculated value of  $P_j/P_\infty = 0.150$  which was assumed in Reference 16.

This solution was initialized using the solution for the attached strong shock case with a calculated nozzle pressure ratio equal to 0.150. Except for the upstream jet boundary, boundary conditions and mesh

configuration identical to those of the attached case were utilized. At the upstream jet boundary the following velocity profile was fixed:

$$\begin{array}{ll} u = 2002 \text{ ft/sec} & 0 \leq r/r_{\text{jet}} \leq 0.835 \\ u = 0 & 0.835 < r/r_{\text{jet}} \leq 1 \\ v = 0 & 0 \leq r/r_{\text{jet}} \leq 1 \end{array}$$

As shown in Figure 51, this velocity input profile increased the displacement thickness of the jet boundary layer in rough approximation to that caused by separation in the nozzle. In this case the jet flow is assumed to be turbulent in nature.

As shown in Figure 52, a strong shock solution was obtained, with a reflection length of  $x_s/r_{\text{jet}} = 1.29$ , about 2% greater than the experimental value at this jet total pressure case. The base pressure coefficient obtained was equal to -0.264, about 8% less than the experimental value and in much better agreement than that of the attached jet boundary layer case.

Although discrepancies in this solution such as the smaller diameter of the computational Mach disc and the appearance of a physically non-existent secondary Mach disc further downstream are apparent, this case does demonstrate that separation and its effect on the flow expansion in the nozzle can significantly impact the resultant base pressure coefficient of the nozzle. Therefore, future computations for low pressure ratios should commence at the throat section to insure that nozzle separation is properly considered.

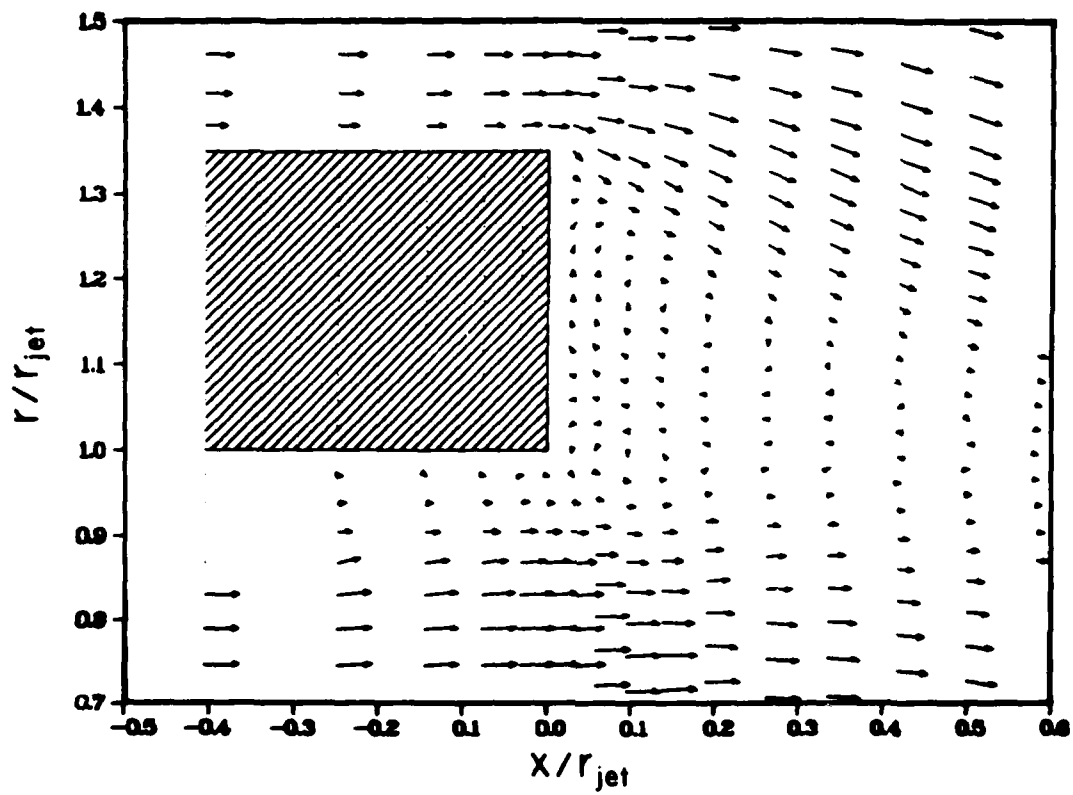


Figure 51. Computed Velocity Profiles Near the Nozzle Annulus for the Separated Flow Simulation

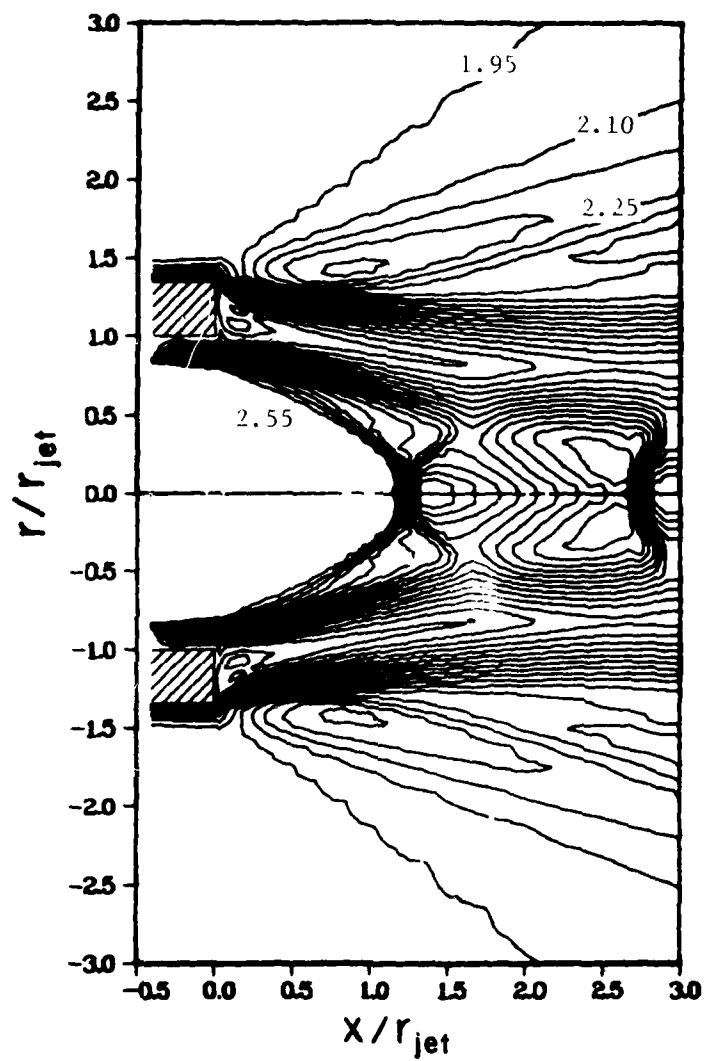


Figure 52. Computed Mach Number Contours for the Separated Flow Simulation

## APPENDIX F

## INVESTIGATION OF NUMERICAL ERROR

Two error analyses were performed on the numerical technique used to obtain solutions for the nozzle flowfields. The first consisted of examining the error generated by the numerical algorithm used to solve the Navier-Stokes equations. The second was a study of the effect of re-positioning first the downstream boundary, and subsequently the upper boundary to regions containing only minor flow gradients normal to each boundary. These analyses are discussed in detail in the following sections.

## 1. TRUNCATION ERROR ANALYSIS

MacCormack's explicit finite difference algorithm is an equivalent second order accurate numerical solver. The final converged solution for any case computed by this algorithm should then satisfy the Navier-Stokes equations at all interior node points with second order accuracy. A numerical check on this accuracy was conducted using a typical converged solution and the following procedure.

As shown in Section II, the axisymmetric Navier-Stokes equations can be written as:

$$\frac{\partial U}{\partial t} + \frac{\partial F}{\partial x} + \frac{1}{r} \frac{\partial(rG)}{\partial r} - \frac{H}{r} = 0 \quad (F-1)$$

A nondimensionalized finite difference formulation of these equations can then be written as:

$$\left(\frac{t_c}{U_\infty}\right) \frac{\Delta U}{\Delta t} + \frac{t_c}{U_\infty} \left[ \frac{\Delta F}{\Delta x} + \frac{1}{r} \frac{\Delta(rG)}{\Delta r} - \frac{H}{r} \right] = E = \text{Error} \quad (F-2)$$

where  $U_\infty$  is defined as:

$$U_\infty = \begin{bmatrix} \rho_\infty \\ \rho_\infty u_\infty \\ \rho_\infty u_\infty^2 \\ \rho_\infty e_\infty \end{bmatrix} \quad (F-3)$$

and  $t_c = 5 \times 10^{-6}$  sec is set to insure that the lead terms on the left hand side of Equation F-2 are of order one.

The particular check case selected was that containing the strong Mach disc shock structure ( $P_j/P_\infty = 0.150$ ), since this case contains both substantial regions of subsonic and supersonic flow, and oblique as well as normal shock waves. The MacCormack solution for this case was used as input for Equation F-2 where the left hand side of the equation was computed at all interior grid points using a standard two-dimensional second order central differencing scheme applied on the transformed computational plane. The magnitude of the Error vector (E) is then an indication of how close MacCormack's method is to an alternate second order accurate solver. The following root mean square (RMS) values of E were obtained over the interior of the computational domain:

$$E_{rms} = \begin{bmatrix} E_\rho \\ E_{\rho u} \\ E_{\rho v} \\ E_{\rho e} \end{bmatrix} = \begin{bmatrix} 0.026 \\ 0.020 \\ 0.011 \\ 0.026 \end{bmatrix}$$

This result indicates that over the domain, MacCormack's algorithm and the two-dimensional central difference scheme are equivalent to within three percent.

Finally, the Error vector E was examined over the computational domain to determine which regions generated the highest magnitude of error. Since the RMS error value of the continuity equation was one of the largest, and the error distribution was representative of that in the other equations, it is shown in Figure 53. In this figure, only error values greater than the RMS value are shown as contours. Regions containing the largest error consist of those containing shock waves and that containing the expansion fan near the sharp corner of the nozzle. In these shock regions, strong flow gradients exist over areas with fairly coarse finite difference mesh spacing. Although the wake region also contains strong gradients within the mixing layer, it lies within a fine mesh region of the grid that produces much less numerical error.

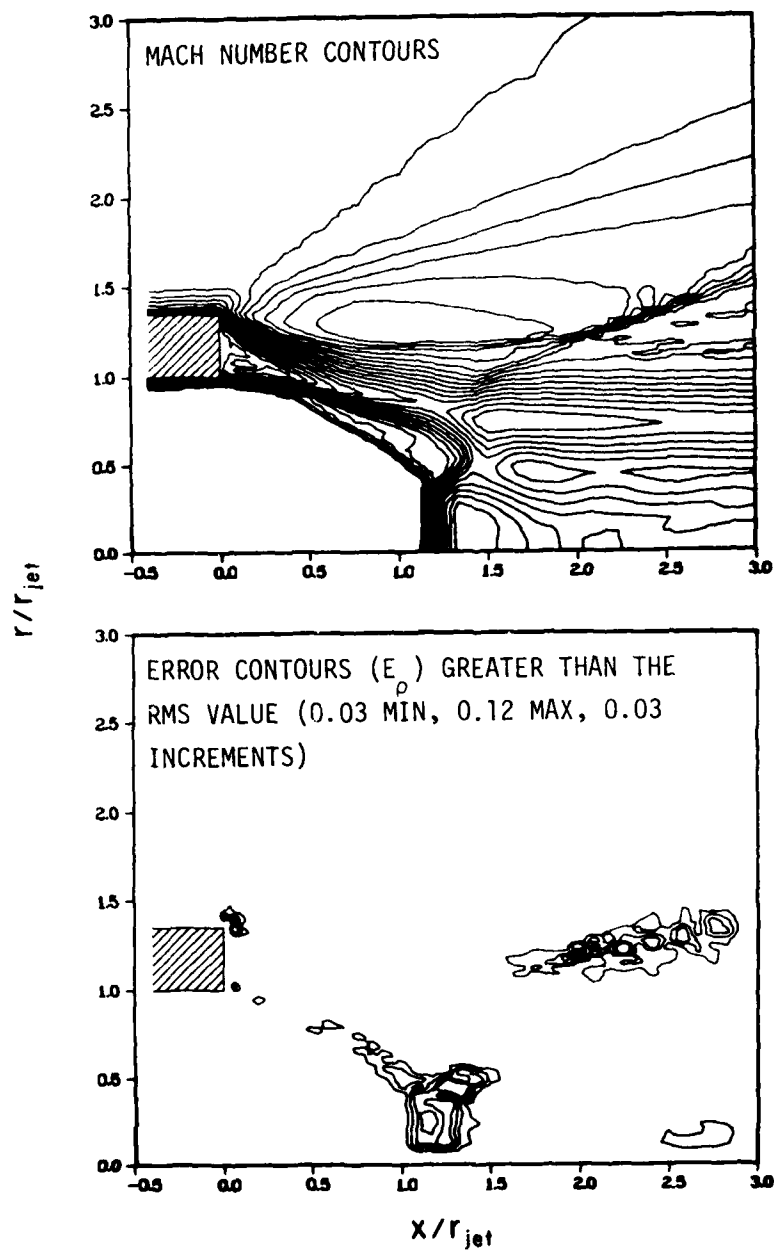


Figure 53. Comparison between the Computational Solution and the Error Present in the Continuity Equation,  $P_j/P_{\infty} = 0.150$

This analysis further demonstrates the desirability of utilizing adaptive mesh schemes that can align the grid with flow gradients as the solution progresses to convergence.

## 2. BOUNDARY POSITION ANALYSIS

Although the upstream boundary, the centerline boundary, and the position of the nozzle walls were fixed by the definition of the problem to be solved, the placement of both the downstream boundary and the upper boundary was left to the discretion of the computational investigator. It was desirable to place these boundaries as close to the nozzle as possible in order to achieve computational efficiency in a compact domain. In the axisymmetric nozzle solutions, both of these boundaries were located in regions in which flow gradients existed due to the presence of shock and expansion waves and viscous phenomena such as shear layers and wakes in the flowfield. The assumption is made that positioning these two boundaries in flow gradient regions does not affect the computational solutions obtained. To validate this assumption, each of these boundaries was repositioned a greater distance from the nozzle to regions containing only minor flow gradients normal to each boundary. The resulting effect on the shock wave structure as well as on the nozzle base pressure coefficient in the numerical solution was then observed.

The nozzle case at which  $P_j/P_\infty = 0.251$  was examined for this particular study. The downstream boundary contains primarily supersonic outflow with an embedded wake region of subsonic outflow. The downstream boundary was extended from its original position at  $x/r_{jet} = 3.0$  to a new value of  $x/r_{jet} = 6.0$ . This stretching was achieved by the addition of twelve grid points axially to the original mesh. The outflow at this new position was totally supersonic in nature with only minor gradients in existence normal to the boundary. As shown in Figure 54, no changes were evident in the shock structure contained in the original domain. The computational base pressure coefficient remained unchanged at a value of  $c_{p_B} = -0.299$ .



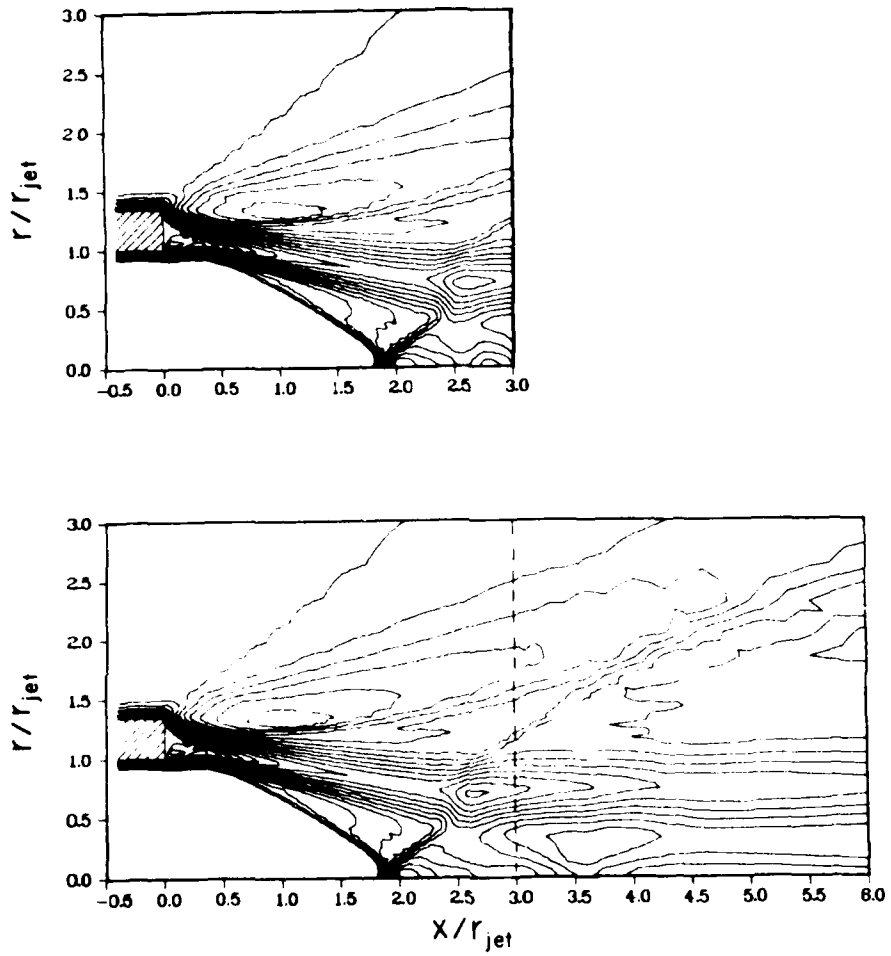


Figure 54. Extension of the Downstream Boundary Showing Computed Mach Number Contours,  $P_j/P_\infty = 0.251$

The effect of repositioning the upper boundary to a radial distance at which flow gradients are not present was then examined. The upper boundary of the axially stretched case was extended from its original value of  $r/r_{jet} = 3.0$  to a new value of  $r/r_{jet} = 6.0$  as shown in Figure 55. In this case eight grid points were added radially to the axially stretched mesh. Again, no changes were evident in the numerical shock structure, and the computational value of the nozzle base pressure coefficient remained at  $\rho_B = -0.299$ .

Since repositioning these boundaries had essentially no effect on the computational solution that was examined, the application of these boundary conditions in the original regions containing mixed supersonic-subsonic flow on the outflow boundary and substantial flow gradients on both boundaries was valid.

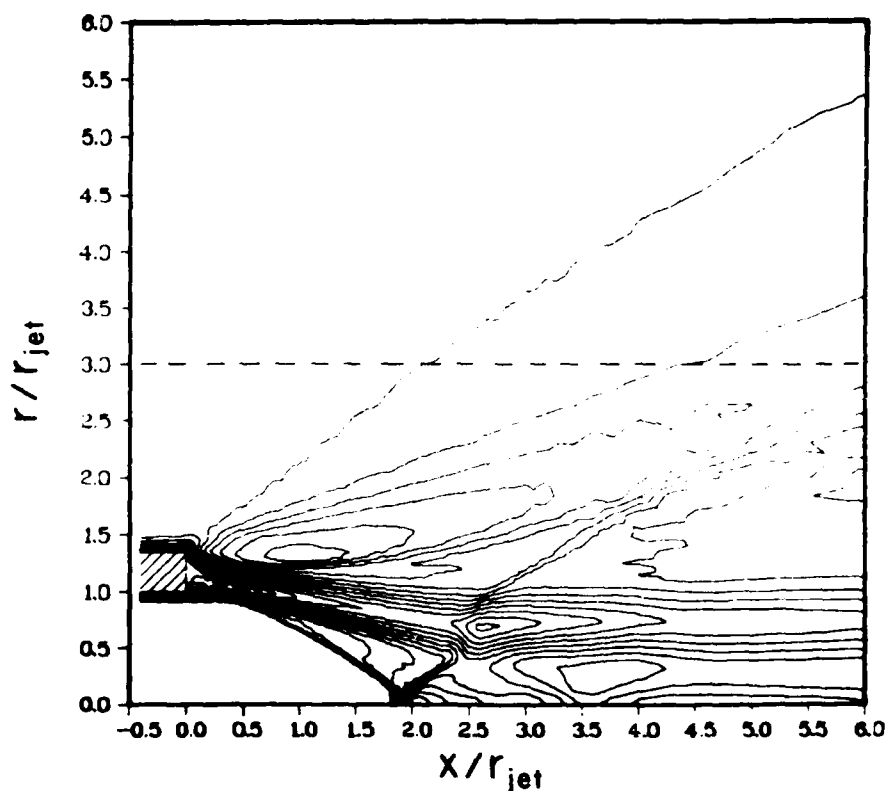


Figure 55. Extension of the Upper Boundary Showing Computed Mach Number Contours,  $P_j/P_\infty = 0.251$

# REFERENCES

1. Grossman, B., and Melnik, R. E., "The Numerical Computation of the Transonic Flow Over Afterbodies Including the Effect of Jet Plume and Viscous Interactions," AIAA Paper 75-62, Pasadena, California, Jan. 1975.
2. Cosner, R. R., and Bower, W. W., "A Patched Solution of the Transonic Flowfields about an Axisymmetric Boattail," AIAA Paper 77-227, Los Angeles, California, Jan. 1977.
3. Pergament, H. S., and Dash, S. M., and Wilmoth, R. G., "Prediction of Nearfield Jet Entrainment by an Interactive Mixing/Afterburning Model," AIAA Paper 78-1189, Seattle, Washington, July 1978.
4. Yaeger, L., "Transonic Flow Over Afterbodies Including the Effects of Jet-Plume and Viscous Interactions with Separation," AIAA Paper 77-228, Los Angeles, California, Jan. 1977.
5. Holst, T., "Numerical Solution of Axisymmetric Boattail Fields with Plume Simulators," AIAA Paper 77-224, Los Angeles, California, Jan. 1977.
6. Mikhail, A. G., Numerical Solution of a Supersonic Nozzle Afterbody Flow with Jet Exhaust, AFFDL-TR-79-3078, June 1979.
7. Shapiro, A. H., The Dynamics and Thermodynamics of Compressible Fluid Flow, The Roland Press Co., 1954.
8. Henderson, L. F., and Lozzi, A., "Experiments on Transition of Mach Reflexion", Journal of Fluid Mechanics, Vol. 68, Part 1, 1975, pp. 139-155.
9. Adamson, T. C., and Nicholls, J. A., "On the Structure of Jets from Highly Underexpanded Nozzles into Still Air," Journal of the Aerospace Sciences, Jan. 1959, pp. 16-24.
10. Eastman, D. W., and Radtke, L. P., "Location of the Normal Shock Wave in the Exhaust Plume of a Jet," AIAA Journal, Vol. 1, No. 4, April 1963.
11. Abbet, M. A., "Mach Disc in Underexpanded Exhaust Plumes," AIAA Journal, Vol. 9, No. 3, March 1971, pp. 512-514.
12. Chang, I. S., "Mach Reflection, Mach Disc, and the Associated Nozzle Free Jet Flows," PhD Thesis, Dept. of Mechanical and Industrial Engineering, University of Illinois at Urbana-Champaign, Urbana, Illinois, 1973.
13. Jofre, R. J., "The Mach Disc in Axisymmetric Rocket Plumes," PhD dissertation, Louisiana State University, May 1971.

REFERENCES (Cont'd)

14. Sinha, R., Zakkay, V., and Erdos, J., "Flowfield Analysis of Plumes of Two-Dimensional Underexpanded Jets by a Time-Dependent Method," AIAA Journal, Vol. 9, No. 12, Dec. 1971, pp. 2362-2570.
15. Hankey, W. L., "Viscous Analysis of a Slip Surface," AIAA Journal, Vol. 10, No. 10, October 1972, pp. 1363-1364.
16. Bromm, A. F., and O'Donnell, R. M., "Investigation at Supersonic Speeds of the Effect of Jet Mach Number and Divergence Angle of the Nozzle upon the Pressure of the Base Annulus of a Body of Revolution," NACA RM L54116, Dec. 1954.
17. Roache, P. J., Computational Fluid Dynamics, Hermosa Publishers, Albuquerque, New Mexico, 1972.
18. Chapman, D. R., "Computational Aerodynamics Development and Outlook," AIAA Journal, Vol. 17, No. 12, December 1979, pp. 1293-1313.
19. Ames Research Staff, "Equations, Tables and Charts for Compressible Flow," NACA Report 1135, 1953.
20. Rubesin, M. W. and Rose, W. C., "The Turbulent Mean-Flow, Reynolds Stress, and Heat Flux Equations in Mass Averaged Dependent Variables," NASA TMX-62, 248, March 1973.
21. Hirt, C. W., Nichols, B. D. and Romero, N. C., "SOLA - A Numerical Solution Algorithm for Transient Fluid Flows," Report LA-5852, Los Alamos Scientific Laboratory, April 1975.
22. MacCormack, R. W., "Numerical Solution of the Interaction of a Shock Wave with a Laminar Boundary Layer," Proceedings of the Second International Conference on Numerical Methods in Fluid Dynamics, Univ. of California, Berkely, September 15-19, 1970.
23. MacCormack, R. W. and Baldwin, B. S., "A Numerical Method for Solving the Navier-Stokes Equations with Application to Shock-Boundary Layer Interactions," AIAA Paper 75-1, Pasadena, Calif., January 1975.
24. Black, Roie, "Parabolized Navier-Stokes Solver," to be published as an AFWAL Tech Memorandum.
25. Shang, J. S., Hankey, W. L., and Dwyer, D. L., "Compressible Turbulent Boundary Layer Solutions Employing Eddy Viscosity Models," ARL Report #73-0041, March 1973.
26. Blake, Charles R., "Numerical Solution of the Compressible Boundary Layer Equations Over Axisymmetric Surfaces," AFIT Master's Thesis Ga/Ma/76D-4, 1976.
27. Schlichting, H., Boundary Layer Theory, McGraw-Hill Book Company, New York, 1968.

REFERENCES (Concluded)

28. Harsha, P. T., Free Turbulent Mixing: A Critical Evaluation of Theory and Experiment, AEDC-TR-71-36, February 1971.
29. Cebeci, T., Smith, A., and Mosinskis, G., "Calculation of Compressible Adiabatic Turbulent Boundary Layers," AIAA Journal, Vol. 8, No. 11, November 1970, pp 1974-1982.
30. Dash, S. M., Wilmouth, R. G., and Pergament, H. S., "Overlaid Viscous/Inviscid Model for the Prediction of Near Field Jet Entrainment," AIAA Journal, Vol. 17, No. 9, September 1979, pp 950-958.
31. Pergament, H. S., Dash, S. M., and Varma, A. K. "Evaluation of Turbulence Models for Rocket and Aircraft Plume Flowfield Predictions," ARAP Report No. 370-1, February 1979.
32. Baldwin, B. S. and Lomax, H., "Thin Layer Approximation and Algebraic Model for Separated Turbulent Flows," AIAA Paper 78-527, Huntsville, Alabama, January 1978.
33. Toyoda, J., and Hirayama, N., "Turbulent Near Wake of a Flat Plate ( Part 2, Effects of Boundary Layer Profile and Compressibility)," Bulletin of the JSME, Vol. 18, No. 120, June 1975, pp 605-611.
34. Rom, J., Seginer, A., and Kronzon, J., "The Flow Field in the Turbulent Supersonic Near Wake Behind a Two-Dimensional Wedge Flat Plate Model," TAE Report No. 54, August 1966.
35. Rom, J., Seginer, A., and Kronzon, J., "The Velocity, Pressure and Temperature Distributions in the Turbulent Supersonic Near Wake Behind a Two-Dimensional Wedge Flat Plate Model," TAE Report No. 80, September 1968.
36. Lin, C. C. (editor), Turbulent Flows and Heat Transfer, Volume 5, High Speed Aerodynamics and Jet Propulsion, Princeton University Press, 1959.
37. Launder, B. E., and Spaulding, D. B., "The Numerical Computation of Turbulent Flows," Computer Methods in Applied Mechanics and Engineering, Vol. 3, pp. 269-289, 1974.
38. Peery, K. M., and Forester, C. K., "Numerical Simulation of Multi-Stream Nozzle Flows," AIAA Paper 79-1549, AIAA 12th Fluid and Plasma Dynamics Conference, Williamsburg, Virginia, July 1979.
39. Shang, J. S., Buning, P. G., Hankey, W. L., and Wirth, M. C., "Performance of a Vectorized Three-Dimensional Navier-Stokes Code on the CRAY-1 Computer," AIAA Journal, Vol. 18, No. 9, September 1980, pp. 1073-1079.
40. Kays, W. M., Convective Heat and Mass Transfer, McGraw-Hill, Inc, 1966.

**MED**  
**-8**